HUMBERTO AKIRA UEHARA SASAKI

DIGITAL TWIN OF A MANEUVERING SHIP: REAL-TIME ESTIMATION OF DRIFT AND RESISTANCE COEFFICIENTS BASED ON SHIP MOTION AND RUDDER AND PROPELLER COMMANDS

São Paulo
2023

HUMBERTO AKIRA UEHARA SASAKI

DIGITAL TWIN OF A MANEUVERING SHIP: REAL-TIME ESTIMATION OF DRIFT AND RESISTANCE COEFFICIENTS BASED ON SHIP MOTION AND RUDDER AND PROPELLER COMMANDS

Dissertation submitted to the Escola Politécnica da Universidade de São Paulo to obtain the degree of Master of Science.

São Paulo
2023

HUMBERTO AKIRA UEHARA SASAKI

DIGITAL TWIN OF A MANEUVERING SHIP: REAL-TIME ESTIMATION OF DRIFT AND RESISTANCE COEFFICIENTS BASED ON SHIP MOTION AND RUDDER AND PROPELLER COMMANDS

Revised Version

Dissertation submitted to the Escola Politécnica da Universidade de São Paulo to obtain the degree of Master of Science.

Area of study:

Control and Mechanical Automation Engineering

Advisor:

Prof. Dr. Eduardo Aoun Tannuri

Co-advisor:

Dr. Pedro Cardozo de Mello

São Paulo
2023

Este exemplar foi revisado e corrigido em relação à versão original, sob responsabilidade única do autor e com a anuência de seu orientador.

São Paulo, **10** de **Julho** de **2023**

Assinatura do autor: Humberto Akira Uehara Sasaki

Assinatura do orientador: _____

Catalogação-na-publicação

Uehara Sasaki, Humberto Akira
Digital Twin of a Maneuvering Ship: Real-time Estimation of Drift and Resistance Coefficients Based on Ship Motion and Rudder and Propeller Commands / H. A. Uehara Sasaki -- versão corr. -- São Paulo, 2023.
120 p.

Dissertação (Mestrado) - Escola Politécnica da Universidade de São Paulo. Departamento de Engenharia Mecatrônica e de Sistemas Mecânicos.

1.Drift and resistance coefficients 2.Unscented Kalman Filter 3.Maneuvering dynamics 4.Digital Twin I.Universidade de São Paulo. Escola Politécnica. Departamento de Engenharia Mecatrônica e de Sistemas Mecânicos II.t.

RESUMO

O presente trabalho aborda o problema de modelagem referente às etapas iniciais de uma implementação de um Gêmeo Digital (DT) de um navio em manobras, mais especificamente se concentrando em estimar em tempo real os principais coeficientes hidrodinâmicos de uma embarcação – os coeficientes de deriva e resistência. O procedimento consiste em duas etapas distintas: uma se referindo à navegação em alto mar e a outra em águas restritas ou portuárias.

Em ambos, o método escolhido se deu através do Filtro de Kalman em sua versão Unscented (UKF), cujas medições são os movimentos obtidos por GNSS, Girocompasso e IMU e as entradas, os comandos para o propulsor e o leme. Uma prova de conceito foi testada em um ambiente simulado chamado *pyDyna* – um simulador de manobras implementado em *Python* embasado no modelo matemático adotado no Centro de Simulação de Manobras do Tanque de Provas Numérico da Universidade de São Paulo (TPN-USP).

Dados de sensores de movimento foram emulados ao acrescentar um ruído branco Gaussiano nos valores advindos em tempo real do simulador, visando uma melhor representação de um cenário prático com medições imperfeitas. Resultados obtidos se mostraram com relativa boa aderência e baixo custo computational, possivelmente apresentando o método como um conveniente avaliador preliminar de parâmetros até outros métodos de melhor acurácia e despendiosos como CFD serem executados (pelo menos para um dos parâmetros hidrodinâmicos no estado atual deste trabalho).

Não obstante, a fim de se obter uma implementação prática de DT, outros problemas devem ser estudados, como design da arquitetura, rede de comunicação, motivação da digitalização, etc., assuntos que não serão abordados aqui. Ao invés disso, este trabalho se concentrou em desenvolver um modelo geral de sistema coerente, que almeja ser um pilar para futuras implementações de DT. Alguns exemplos que podem eventualmente implementar essa tecnologia são: análise de performance devida à degradação do casco, leme ou propulsor; auxílio na tomada de decisão para manutenções programadas e até monitoramento remoto.

Palavras-Chave – Coeficientes de resistência e deriva, Unscented Kalman Filter (UKF), Dinâmica de manobras de navios, Gêmeo Digital (DT).

ABSTRACT

The present work tackles the modeling problem concerning the initial steps of a Digital Twin (DT) application in a maneuvering ship, more specifically focusing in estimating in real-time the main vessel hydrodynamic coefficients – namely drift and resistance coefficients. The procedure consists in separating it into two different estimation phases: one referring to a vessel in open seas and another in restricted waters or port maneuvers.

In both, the chosen method is via Unscented Kalman Filter (UKF), whose measurements are the ship motions obtained from GNSS, Gyrocompass and IMU, and the input, the commands to the propeller and rudder. A proof of concept was tested in a simulated environment called *pyDyna* -– a ship maneuvering simulator implemented on *Python* based on the mathematical model adopted in the TPN-USP Ship Maneuvering Simulation Center.

Data from motion sensors were mimicked by adding a Gaussian white noise in the values retrieved from the simulator in real-time, intending to better represent a real-world scenario with not perfect measurements. Obtained results show limited good adherence and low computational cost, possibly presenting the method as a convenient preliminary parameter assessment, until more accurate and time-consuming methods such as CFD are evoked (at least for one of the hydrodynamic parameter in the current state of this work).

Nonetheless, to envision a real DT implementation, further problems need to be solved, such as architecture design, communication network, digitalization purpose, etc., subjects which will not be discussed here. Instead, this work focused on developing a well-rounded general system model, that intends to be a cornerstone to future DT implementation, some examples that could implement this technology are: performance analysis due to degradation of the hull, rudder, or thruster; decision support for maintenance scheduling; or even distance monitoring.

Keywords – Drift and resistance coefficients, Unscented Kalman Filter (UKF), Ship maneuvering dynamics, Digital Twin (DT).

LIST OF RELEVANT ABBREVIATIONS

CAD	Computer Aided Design
CFD	Computer Fluid Dynamics
DT	Digital Twin
DoF	Degrees of Freedom
EKF	Extended Kalman Filter
GNSS	Global Navigation Satellite System
IMU	Inertial Measurement Unit
ITTC	International Towing Tank Committee
KF	Kalman Filter
LOA	Length Overall
NED	North-East-Down
PUKF	Projected Unscented Kalman Filter
TPN-USP	Numerical Offshore Tank from University of São Paulo
UKF	Unscented Kalman Filter
UT	Unscented Transformation

LIST OF FIGURES

LIST OF TABLES

CONTENTS

PART I

GENERAL STRUCTURE

1 INTRODUCTION

Determining the hydrodynamic characteristics of a ship is a highly complicated task, since many parameters affect the motion dynamics. These parameters determine the incident reaction forces due to the ship motion on water, the effectiveness of the rudder action and the thrust force generated by the propeller.

In the past, experimental investigations were the basis for creating the general framework in the naval construction, as it can be seen in an assay conducted by Leonardo da Vinci around 1500, in which he tested three ship models with the same length and different fore and aft shape, for then reaching an optimized shape result for the highest speed from this utterly restrict sample domain (STEEN, 2014). Yet, it was sufficient at the epoch considering all the limitations from a mathematical, technological and material point of view.

Advancing some centuries, Isaac Newton revolutionized the field of Hydrodynamics, enhancing the understanding of the interaction of bodies with fluids; William Froude's experiments of towing small wooden models by a system of ropes and falling weights carved out a path for better integrating the scientific method with the field of marine technology; and around 1800 with the introduction of mechanically driven ships, mainly by paddle wheels and powered by steam engines.

Soon, these experimental innovations would be assembled into what is known in current days as Towing Tanks, where the model is pull through a carriage in a large tank with controlled temperature and density. Being the only method back in the 1870s, such apparatus allowed to achieve better standards of hydrodynamic efficiency, as more emphasis could be given in the hull shape design (OOSTERVELD, 1991). Concurrently, the transition from wood structures towards iron in the late 19th was hugely benefited with these new experimental facilities, allowing big departures from traditional designs, as could be seen in the late ironclads.

Fast forwarding until late 1970s, with the emergence of the computers, the *Computa-*

tional Fluid Dynamics (CFD) soon became a major player in the optimization phase of the design process. Various alternative designs could be calculated in a short period of time, in comparison with the old manner. Not only the conception part was evolved by the *Third Industrial Revolution*, but also the Instrumentation was heavily benefited with the rise of electronics.

Measuring instruments became increasingly and progressively more precise, robust and cheap, allowing reintegrating back on the design loop the real world behaviour and some other characteristics that were beforehand neglected on the theory scope. One former student of Patrick F. Dunn (DUNN, 2010), M. Clark, once cited that:

> making predictions can serve as a guide to what we expect, (...) but to really learn and know what happens in reality, experiments must be done

Although it was thought for the justification of experiments, it also reflect the importance of knowing how some objects and phenomenons interact with the environment with precision, since at the end no matter how good a model can be, it will be always a grasp of our understanding of the real world.

Such reflect can be even seen in multiple applications, specially with the increasing adherence in machine learning emerging methods, which essentially embodies the core principles from the empiric school by creating models purely from observed data. Albeit being extremely useful to retrieve various complex behaviours in the maritime field, it also carries an interpretability concern. Particularly, but not only, for these scenarios, traditional physics based ones continue with its relevance.

Other vantages towards the latter can be seen in the setup. Machine learning techniques in a broad aspect usually take time to learn the model and can be sometimes not so intuitively to tune to every slight variation encountered in a real vessel, hindering the efficacy of tailor made solutions.

With the advances in communication field, as seen in the adoption of the Global Maritime Distress and Safety System (GMDSS) in the late 1980s, information exchange between a sailing vessel and a stationary base in land became possible and increasingly recurring, specially for security and safety reasons. As this technology evolved, along the years, the bandwidth data widened and its speed transfer drastically improved, tracking capabilities become even more precise than ever, opening new opportunities for real-time applications, such as autonomous navigation and digitalization field.

Yet, all these implementations still require a sufficiently good knowledge of the vessel

characteristics, specially concerning the maneuvering dynamics topic.

1.1 Objective

This work proposes an implementation of a phase-zero Digital Twin (DT) of a navigating craft, in other words, a first proposal to model a ship maneuvering dynamics. In order to achieve real-time applicability, some physical simplifications were done, nonetheless, the proposed method still aims to reduce the gap between generic parameterization from standard System Identification procedures, by further modeling some system aspects such as the propeller and rudder dynamics.

By targeting this initial DT application, the following objectives shall be resolved:

- A general methodology to retrieve simplified maneuvering mathematical models;
- Better representation of the propeller and rudder internal mechanisms;
- Testing and validation of concept in a high fidelity simulator.

1.2 Work structure

A schematic of the proposed workflow is presented in Fig.1.

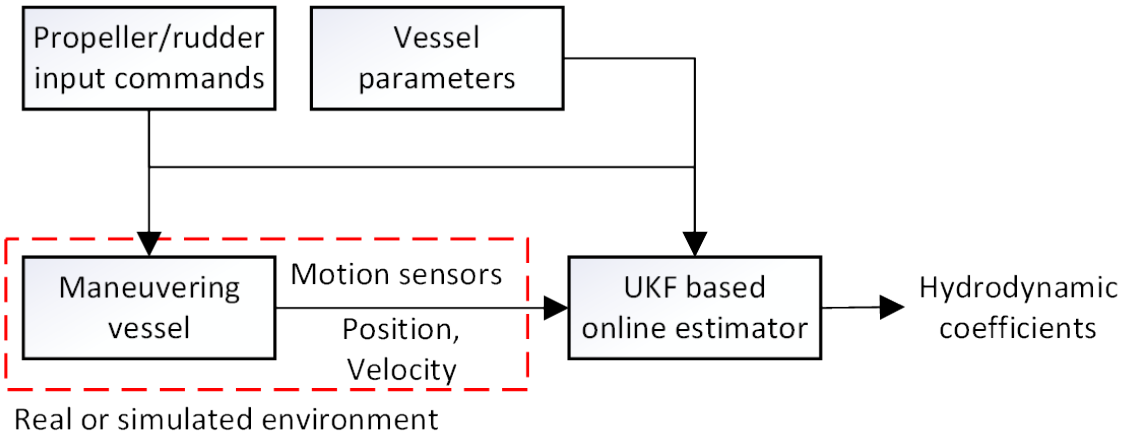

Figure 1: Block diagram of the proposed method.

With the information retrieved from certain motion sensors, namely measurements from Global Navigation Satellite System (GNSS), the idea is to obtain in almost real time certain hydrodynamics coefficients of a marine craft purely through an Unscented Kalman Filter (UKF) approach.

Due to the system equations being physics-based, some core vessel parameters need to be informed *a priori*, such as the Length Overall (LOA) L, Draft T, mass matrices and other rudder and propeller general information – fairly simple knowledge data. Both the effective rudder angle and the effective propeller rotation are taken as input, thus being continuously provided during the maneuvers.

Instead of a real maneuvering ship, or several captive model tests or even CFD runs, a simulated environment based on a high fidelity ship maneuvering simulator named *pyDyna* was chosen, due to its capacity of easily generate maneuvering data, being an outstanding option for rapid testing and theory validation.

1.3 Thesis organization

The work is organized in parts, being the one ending here the Introduction (Part 1 - Chapter 1). Secondly, comes the Literature review in Part II, in which the concepts of Digital Twins (Chapter 2) and System Identification (Chapter 3) are explored. In Theoretical background (Part III), the proper system dynamics is modeled (Chapter 4) – which includes the maneuvering, propeller and rudder formulation – followed by the Kalman Filter methodology (Chapter 5).

The problem is tackled in Part IV, with the developed formulation (Chapter 6) followed by a sample of the results obtained in a single vessel for different batch of maneuvers (Chapter 7). Finally, some discussions are done in Part V.

PART II

LITERATURE REVIEW

2 DIGITAL TWIN

"When I use a word, it means whatever I want it to mean"

-- Lewis Carroll

Reciting a dialogue from Alice's Adventures Through The Looking Glass from Lewis Carroll, Wright and Davidson (WRIGHT; DAVIDSON, 2020) firm their statement about the term "Digital Twin". As for many it can be described as a digital representation of a physical object or process that mimics its behaviour and current state in near real time, a broad concept that can be applied to countless areas and in a wide variety of contexts, serving different single or multi focused objectives with the same implementation.

This "broadness" aspect can be translated to "still there is no clear consensus", also by lacking a proper mathematical formulation, each individual company ends with its own definition of what is a "Digital Twin" (ERIKSTAD, 2017; WORDEN et al., 2020; NEGRI; FUMAGALLI; MACCHI, 2017). This is heavily criticized in (WRIGHT; DAVIDSON, 2020), mentioning the hindering effect on the term with its over-usage in situations where the distinction between a simple model and a digital twin is almost none.

Nonetheless, there are some attempts to better contextualize the term, as will be presented in the following sections 2.1 and 2.2. Some concerns are cited in 2.3 and in 2.4 were shown some application examples.

2.1 Technical formulation approach

Authors such as Erikstad (ERIKSTAD, 2017) tries to encapsulate some general concepts that commonly appeared in various allegedly Digital Twin applications. He conceived five core characteristics for this concept:

1. Identity: connection to a single, real and unique physical asset, or several connected subsystems with each covering relevant information from the bigger system.

2. Representation: translate the real system's interested measure in a corresponding engineering model, being a CAD or any other digital format.

3. State: captures the asset's real state close to real time.
4. Behaviour: acts correspondingly as the real system for a same given external stimuli.
5. Context: represents correctly the operating environment in which the system operates, such as wind, waves or temperature.

Erikstad (ERIKSTAD, 2017) has also stated that for an application to be considered a Digital Twin, it should at least be capable of:

- Observing key aspects of the asset's state and behavior provided from sensors with corresponding edge processing capabilities.
- Rendering an almost real time mirror of the asset's state by the incoming data collected from the sensors.

Since a Digital Twin implementation can be applied at any moment of the object or process lifetime, starting from the design up until to the operation phase, Parrot and Warshaw (PARROTT; WARSHAW, 2017) deemed important that the architecture behind it should be thought considering a flexible and scalable design a priori. Madni et al. (MADNI; MADNI; LUCERO, 2019) classified Digital Twins into four levels of sophistication, each one being somehow associated to its physical counterpart time phase:

1. Pre-Digital Twin: supports decision-making at the concept preliminary design or design phase. Essentially it is a virtual prototype whose purpose is usually mitigating technical risks and uncover issues in upfront engineering. Its building base model virtual prototype will not be necessarily carried over the final system.
2. Digital Twin: once the physical twin is already in operation, the virtual representation can receive batch updates from the physical counterpart, such as performance, health and maintenance data, that can be used to explore the system behaviour in hypothetical "what-if" scenarios. As the interaction now is bidirectional with the physical and virtual twins, any detected deficiencies from the latter one can be used to modify the real system.
3. Adaptive Digital Twin: in this level, an adaptive user interface is implemented, as this implementation is directed towards an user of the final system, therefore it will support real-time planning and decision-making during the operational phase. Madni et al. also adds into this classification level the capability of this implementation to learn the preferences and priorities of the human operator.

4. Intelligent Digital Twin: the last step on the maturity level, it incorporates all the previous features adding an extra layer of unsupervised machine learning and reinforcement learning when possible.

Each of these different levels can be implemented accordingly with the usage scope, which can be many: validation of system model with real one, prediction of changes in physical system over time, predictions of consequences in future condition scenarios, provider of decision support and alerts to users for various cases such as schedule maintenance, low operational efficiency, component health depletion or early damage detection, etc (ERIKSTAD, 2017; MADNI; MADNI; LUCERO, 2019). Although the idea of Digital Twin started in the aerospace field, its generality reached various other domains, more notoriously is the manufacturing recently (NEGRI; FUMAGALLI; MACCHI, 2017).

2.2 Mathematical formulation approach

In contrast to Erikstad, Worden et al. (WORDEN et al., 2020) went into a more rigorous mathematical definition of the Digital Twin concept, although in that paper they strongly supported the adoption of the term "mirror" instead of "twins" for establishing an over-arching framework.

2.2.1 Physics-based models

Starting firstly with only physics-based models, being the physical object of interest a *system* S, its characterizing state, or *state vector* $\vec{s}(t)$, consists of a set of N_S instantaneous measurements of S at a given time t (continuous or discrete, but it will be assumed to be the latter for computational implementation):

$$\underline{s}(t_i) = \begin{bmatrix} s_1(t_i) & s_2(t_i) & \cdots & s_{N_S}(t_i) \end{bmatrix} \ , i = 1, \cdots, N_t; t_i \in [0, T] \tag{2.1}$$

Since the *environment* influences S, it is also defined its state vector $\underline{e}(t)$, consisted also by a set of instantaneous environment measurements N_E:

$$\underline{e}(t_i) = \begin{bmatrix} e_1(t_i) & e_2(t_i) & \cdots & e_{N_E}(t_i) \end{bmatrix} \ , i = 1, \cdots, N_t; t_i \in [0, T] \tag{2.2}$$

Generally, one will want to investigate only a part of the system, not the whole, hence a *context* C is also defined:

$$C = \{e_j^C \in E, s_l^C \in \underline{s}; j, l\} \tag{2.3}$$

With the subset $\{e_i^C\}$ being referred as environment context and $\{s_j^C\}$, as the response or predictive context. A schedule W_C for the context C will be a time series:

$$W_C = \{\underline{e}_W^C(t_i); i = 1, \cdots, N_t; t_i \in [0, T]\} \tag{2.4}$$

By imposing a schedule as input, it is possible to test the system, giving a response $\underline{r}_W^C$:

$$\underline{r}_W^C(t_i) = S[\underline{e}_W^C(t_i)] \tag{2.5}$$

The test set T_W^C associated with the schedule W_C in the context C is given by:

$$T_W^C = \{\underline{e}_W^C, \underline{r}_W^C\} \tag{2.6}$$

Once carried multiple tests, one can define the training and testing schedule as the set of schedules associated with acquiring data for its respective purpose: D_{tr} for training and D_t for testing. From these, a model of S for a context C can define a mathematical function M^C, which attempts to predict the behaviour of S for any schedule specific to the context C. A simulation $\underline{m}_W^C$ for a context C under a schedule W_C corresponding to a k-labeled test $T_k^C = \{\underline{e}_k^C, \underline{r}_k^C\}$ can be defined as:

$$\underline{m}_W^C(t_i) = M^C[\underline{e}_W^C(t_i)] \tag{2.7}$$

A metric $d^C(\underline{x}, \underline{y})$ defined by:

$$d^C(\underline{x}, \underline{y}) \geq 0 \ \wedge \ d^C(\underline{x}, \underline{y}) = 0 \Leftrightarrow \underline{x} = \underline{y} \tag{2.8}$$

can be used to associate to the error ϵ on a given context C for all scheduled tests in D_t between the obtained simulation and the observed measures of the physical system with:

$$d^C(\underline{m}^C(t), \underline{r}^C(t)) \leq \epsilon \leq \epsilon_T \tag{2.9}$$

A model M_{ϵ}^{C} is judged as fit-for-purpose in a given context C if and only if the last inequality of (2.9) is respected, being ϵ_T a critical threshold retrieved from engineering requirements, such as empirical judgment, regulatory compliance, security adequacy, etc.

2.2.2 Hybrid models

Black-box and hybrid-box models are respectively models created purely by a model basis with a universal approximation property and tuneable parameters (such as artificial neural networks or support vector machines) and, by combining physics aspects with machine learning approach. Analogously to the physics-based, for these ones cited before, the predictor model M^{hC} is produced using data acquired from a training schedule D_{tr} and tested by a test schedule D_t.

Although the model M^{hC} can be also evaluated accordingly to (2.9), further assessments are made in (WORDEN et al., 2020) towards the probabilistic content of machine learning algorithms, in which the authors propose various other possible metrics to adopt.

2.2.3 Virtualisation concept

Environment variables in a context C can be divided into two groups: the controllable $\underline{e}_c^C$ and uncontrollable $\underline{e}_u^C$. These uncontrolled environmental variables impact when one attempts to use the model for future predictions, hence a generative model M_u^{EC} is needed in this case, that will make some best estimate of $\underline{\hat{e}}_u^C(t)$:

$$\underline{\hat{e}}_u^C(t) = M_u^{EC} \tag{2.10}$$

The model M_u^{EC} can be established as a non-parametric black-box model or can be replaced by mean values with corresponding uncertainties. Once built, it is possible in a given context C to make predictions $\underline{p}^C(t)$:

$$\underline{p}^C(t) = M[\underline{e}_c^C(t), M_u^{EC}(t)] \tag{2.11}$$

Finally, a virtualisation for a given context C is defined as:

$$V^C = (M_{\epsilon_1}^{hC}, M_{\epsilon_2}^{EC}) \tag{2.12}$$

in which both models have its respective ϵ's. The importance of this pair is that it can

be used to examine what-if scenarios for the system, possibly providing an insight on how it will behave in hypothetical extreme events, failures or simply for evaluation purposes.

2.3 Common problematics

Besides the already mentioned diffused definition of the Digital Twin term, Rasheed San and Kvamsdal (RASHEED; SAN; KVAMSDAL, 2020) pinpoint four main problems that one should be careful in a successful Digital Twin implementation:

1. Real-time connectivity: necessity of a two-way connection between the physical asset and its digital twin. Major concerns are due to sensors resolution data, latency in communication, large traffic and generated data volume, etc.

2. Backwards compatibility: capacity of maintaining previous used architectures still operating as the physical asset evolves in time.

3. Safety and security: as some applications will affect on decision assignment, physical consistency, transparency and interpretability are required characteristics – which can be sometimes extreme difficult, specially with the increasingly use of black-box models.

4. User friendliness: the final digital twin product should appear the same with its real counterpart and be easy to operate.

Depending on the application-specifics, many more challenges emerges, Grieves and Vickers (GRIEVES; VICKERS, 2017) mention some other obstacles such as the non-homogeneous information perspective between engineering and manufacturing phases, simulation specific softwares without multi-domain focus and predictability behaviour when facing extreme rare or difficult to simulate natural phenomena.

2.4 Application examples

Following the Industry 4.0 trend commenced by the German government (KAGERMANN; WAHLSTER; HELBIG, 2013), movement highly characterized for its focus shift towards digital transformation, the maritime industry also sailed into the integration of new technologies from the so called "*Fourth Industrial Revolution*" – such as Cyber-Physical

Systems (CPS), Internet of Things (IoT) and Internet of Services (IoS). Each year progressively sophisticated on-board equipment with embedded computers and preciser sensors become easily accessible in regards of price and availability (RØDSETH; PERERA; MO, 2016), providing new information data that before were not reliably accurate.

As briefly mentioned in (ERIKSTAD, 2018), Digital Twins can be implemented with in-numerous purposes, such as:

- Replication in a virtual model of the state and behaviour in close to real time based on sensor observations.
- Study of the state and behaviour of an asset given a simulated input based on deriving asset responses from observations.
- Detection of anomalies or defects by continuous comparison of monitored and simulation-derived behaviours.

2.4.1 Regarding maritime operations

Autonomous vehicles are an example of systems that Digital Twin technology has a key role for their implementation, since one should at least be projected with the first previous intend mentioned in mind. An experimental autonomous ship such as the ReVolt, which is being developed by *Den Norske Veritas - Germanischer Lloyd* (DNV GL) (DANIELSEN-HACES, 2018), is an illustration of how one can envision in a Digital Twin system.

3 SYSTEM IDENTIFICATION ON SHIP MANEUVERING

As viewing the technical and mathematical requirements in 2.1 and 2.2 respectively, the knowledge and correct assessment of a model is an essential pillar in regard to Digital Twin architecture. Thus, the subject of System Identification, which is part of the basic scientific methodology, becomes critical, since it deals with the problem of elaborating mathematical models of dynamic systems based on observed data (LJUNG, 1998).

Ljung in (LJUNG, 1998) describes three basic entities for constructing a model from data:

1. Data Record: the required input-output data recorded during a identification experiment.
2. Set of models or model structure: set of candidate models searched to be the best suitable, being composed from basic physical laws, other well-established relationships, standard linear models or even black-box models.
3. Model judgement: the verification of the model quality, typically based on how the models perform when confronted against measured data accordingly to an adopted rule, such as the Least Square selection rule.

After successfully passing through all the mentioned steps, the final phase is the model validation itself. Involving various procedures to assess how the model relates to observed data, to prior knowledge and to its intended use scope. Even after all this, Ljung reinforces in (LJUNG, 1998) that:

> A model can never be accepted as a final and true description of the system. Rather, it can at best be regarded as a good enough description of certain aspects that are of particular interest to us.

Some examples of System Identification techniques applied in ship maneuvering are presented in the following sections: 3.1 and 3.2.

3.1 Physics-based approaches

Consisting into models derived from fundamental physical laws, the so called white-box models have been applied not uniquely in maritime transportation but also in terrestrial and aerial fields, as they become crucial in the design process of navigation controllers, specially with the increasing demand generated by the autonomous vehicles technologies. Some related works will be discussed in this section.

Ma and Tong presented in (MA; TONG, 2003) a fairly simple model focused only in the longitudinal speed of a ship, even with an EKF and Second Order Filter to treat the system nonlinearities, the steering process impacted hugely into the poor obtained estimations, with some having a percentage error of above 40% on average and other parameters not even been able to be recovered.

Hajizadeh, Seif and Mehdigholi (HAJIZADEH; SEIF; MEHDIGHOLI, 2016) and Shi et al. (SHI et al., 2009) considered a maneuver dynamics with 3 degrees of freedom (DoF), longitudinal, transversal and rotation, consisting in a planar representation of the movement in 2D. In both works, they arrived in similar formulations and though the augmented states formulation of the EKF, they could retrieve the ship maneuvering characteristics with acceptable accuracy. Yet, both the rudder and propeller internal dynamics were not implemented, instead, general parameter identification modeling were adopted to represent these dynamics.

Parting from a different basis, Wang, Perera and Batalden (WANG; PERERA; BATALDEN, 2021) approached the maneuver dynamics by the acceleration measurements, formulating around the curvilinear motion model (LI; JILKOV, 2003). Although they acquired sufficiently accurate results with a Particle Filter methodology, they were restricted to the states of system dynamics, hence positions, velocities and accelerations, not considering intrinsic vessel parameters.

Other common modeling procedures are based into the well-renown Nomoto model (NOMOTO et al., 1957), which consists in decoupling the longitudinal movement with the turning analysis. However, even Nomoto et al. themselves mentioned the model limitations facing higher rudder deflection angles, point reiterated by Källström and Älström in (KÄLLSTRÖM; ÅSTRÖM, 1981).

Perera, Oliveira and Soares in (PERERA; OLIVEIRA; GUEDES SOARES, 2015, 2016) and Casado and Ferreiro (CASADO; FERREIRO, 2005) worked in an enhanced Nomoto second order model with the reversed spiral curve proposed by Amerongen and Cate (VAN

AMERONGEN; UDINK TEN CATE, 1975). Whilst the former implemented an EKF, the latter opted to apply a Model Reference Adaptive Control, more specifically, with a recursive design known as adaptive backstepping introduced by Krstić, Kanellakopoulos and Kokotovic (KRSTIĆ; KANELLAKOPOULOS; KOKOTOVIĆ, 1995). Both strategies were efficient, although they both emphasized the strong assumption that the forward longitudinal speed of the ship needs to maintain constant in order to retrieve good results.

3.2 Machine learning methodologies

Gravitating towards more black-box models, many other studies have been conducted on System Identification field, as they usually do not necessarily require complex physical equations.

Neural Network applications in ship maneuvering field can be found in early 2000s with (HESS; FALLER, 2001; MOREIRA; GUEDES SOARES, 2003; CHIU et al., 2004; MARTINS; LOBO, 2007). Due to being versatile as it can approximate various functions using a set of the appropriate number of parameters, it is also implemented in different kinds of scenarios, such as low-speed maneuvers (WAKITA et al., 2022) and ice interaction in complex ice fields (MILAKOVIĆ et al., 2020).

Other techniques such as Support Vector Machines are used in (LUO, 2016; XU et al., 2019, 2020; MEI; SUN; SHI, 2019), with the last two interested in some particularities: Luo et al. employed the method targeting a catamaran maneuver model in (LUO; MOREIRA; GUEDES SOARES, 2014) and Xu et al. tackled the shallow water effect in (XU et al., 2020). Within the same category, Random Forest can also be seen implemented along with a Model Reference approach as in (MEI; SUN; SHI, 2019), leaning more into the hybrid modeling territory.

Focusing more in the uncertainty characteristics of the measurement inputs, Gaussian Process can also be implemented as viewed in (XUE et al., 2020; OUYANG; ZOU, 2021), with Xue et al. introducing the noise information into the input data in the former (XUE et al., 2020) and with Ouyang and Zou including Genetic Algorithm to optimize the hyperparameters in the kernel function in the latter (OUYANG; ZOU, 2021).

3.3 Review insights

After extensive presentation of System Identification methodologies applied in the maritime field, a point noted is that none envision a proper complete modeling, parting from the propeller and rudder to the maneuvering itself. Rigorously, leading even the so called white-box models being treated as grey-box considering the adopted higher abstraction level of the mentioned components in term of mathematical modeling.

Approaches shown in (MA; TONG, 2003; HAJIZADEH; SEIF; MEHDIGHOLI, 2016; SHI et al., 2009) presented generic terms that could not grasp the internal dynamics of the rudder or propeller mechanisms. While the cross terms such as $X_{v\delta}, X_{un}$ were introduced to circumvent that, these additions complicated the estimations, specially in terms that influenced lateral and rotation velocity, as they are usually smaller.

Works based on the model of Nomoto (NOMOTO et al., 1957; PERERA; OLIVEIRA; GUEDES SOARES, 2015, 2016; CASADO; FERREIRO, 2005) achieved better results in terms of course varying scenarios, specially the ones with higher model complexity, however, these still suffer in more rough changing heading angles and the assumption of constant advance speed.

Finally, applications based on machine learning methodology albeit being well robust, when merely focused in the input-output relation for model generation, they suffered considerably in the time and computational power spent to training, as also of the Particle Filter method. This aspect posed a challenging problem when envisioning a real-time and portable solution.

Interpretability is another problem that is very recurrent in these. The notion to how the parameters can affect each aspect of the modelling is usually lost and any unexpected obtained results become hard to reverse-engineering to justify its assessment.

Initial steps were taken in preliminary works presented in (UEHARA SASAKI et al., 2021), with a first modeling proposal using EKF and in (UEHARA SASAKI; DE MELLO; TANNURI, 2022), with the inclusion of the ship's propeller and rudder dynamics and the replacement towards the UKF.

PART III

THEORETICAL BACKGROUND

4 SYSTEM DYNAMICS MODELING

4.1 Essential concepts

4.1.1 Vessel general characteristics

Being a complex combination of different sizes, hull shapes, superstructure designs, etc, ships are usually classified by their basic dimensions, their weight or water displacement and their intended service (STORCH et al., 1995). Although some specific definitions are dependent of this latter, most of them are applicable for all ship types.

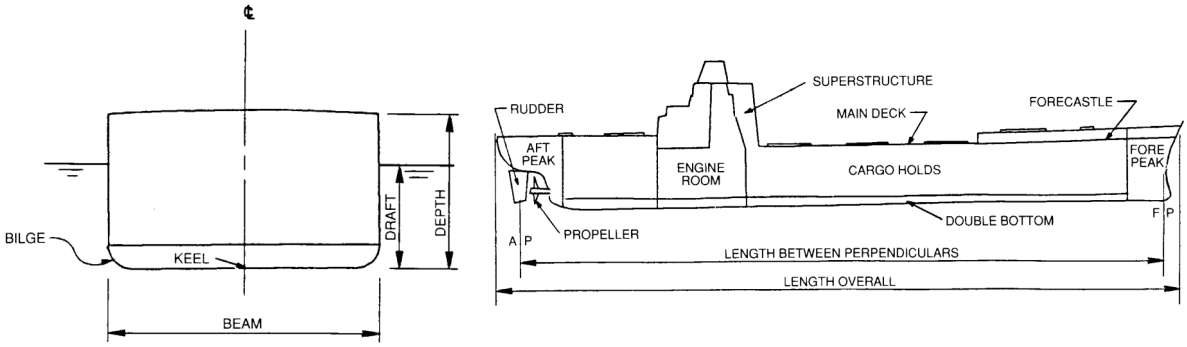

Figure 2: General view of a ship (extracted from (STORCH et al., 1995)).

Regarding this work, the interesting general dimensions to be used are the Draft T and the Length Overall (LOA) L as shown in Fig.2. Rigorously, the most adequate term to use should be the Length Between Perpendiculars L_{pp}, as it represents the ship length which crosses the waterline, however, as it is dependent of the draft at the moment, its value is usually hard to precise. Calculations for the Reynolds number usually take this latter:

$$R_n = \frac{L_{pp}}{\nu}|u_r|, \quad \nu = 1 \times 10^{-6} m^2/s \tag{4.1}$$

The term ν represents the kinematic viscosity of the fluid, in this case, the water, and u_r is the relative surge speed. Analogous to the Froude number:

$$F_n = \frac{u_r}{\sqrt{gL_{pp}}} \tag{4.2}$$

With g being the gravity acceleration.

Both propeller and rudder are subsystems of a ship that can be thought as equally complex systems as their own. Nonetheless, some fundamental characteristics can be seen. For the former, regarding the generation of thrust power in screw type propellers, one of the core parameters to consider is its diameter, shown in Fig.3a as D, but used here onward as D_p.

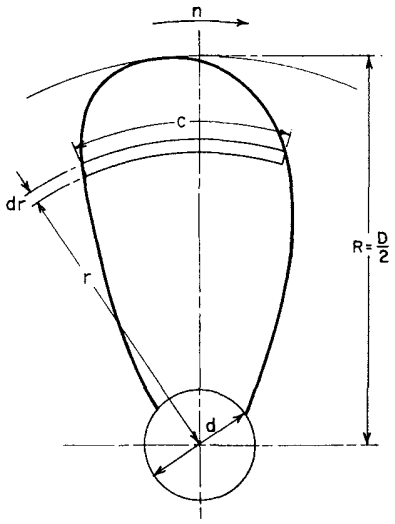

(a) Propeller blade view (extracted from (LEWIS, 1988)).

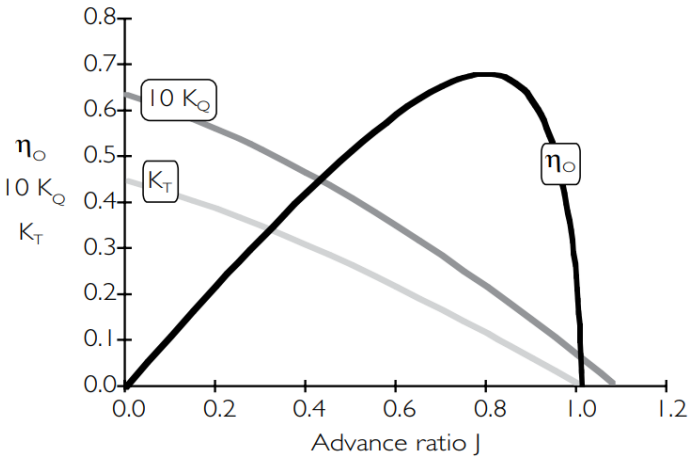

(b) Example of a screw propeller open water diagram (extracted from (STAPERSMA; WOUD, 2005)).

Figure 3: Propeller general characteristics.

In this case, open water diagrams such as the presented in Fig.3b gives the relation between torque, thrust, ship speed and propeller speed.

As for the rudder, albeit existing numerous parameters as shown in Fig.5, their impact in the generation of thrust and moment for the ship can be seen in the drag and lift curves, which can be retrieved from CFD or from experiments, such as shown in Fig.4.

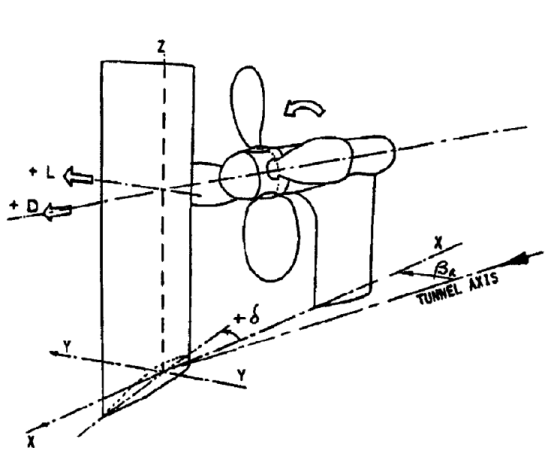

(a) Experiment schematics.

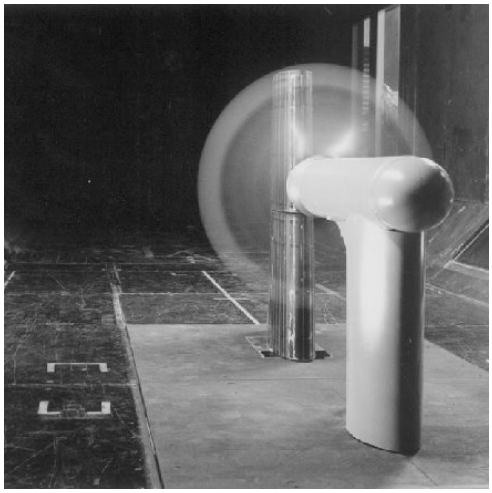

(b) Final setup.

Figure 4: Arrangement of a wind tunnel experiment to extract drag and lift curves from a rudder (extracted from (MOLLAND; TURNOCK, 2007)).

Nonetheless, in the formulation by Kose et al. (KOSE; YUMURO; YOSHIMURA, 1981) that will be later presented in 4.3.2, the essential characteristic to be taken is the position of the center of pressure (x_R, y_R) relative to the ship.

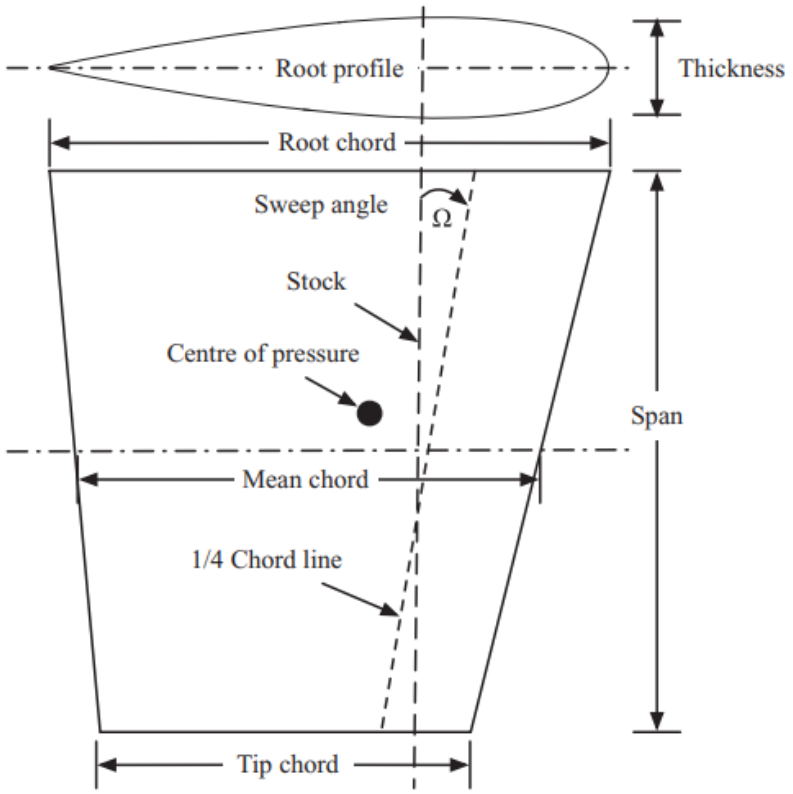

Figure 5: General notation for a rudder (extracted from (MOLLAND; TURNOCK, 2007)).

4.1.2 NED to Body frame transformation

As will be further described in 4.2, the maneuvering dynamics equations are formulated in the frame fixed to the vessel itself, usually centering the origin to coincide with a point midships in the water line. Yet, some measurements taken, such as the GNSS measurements, are provided in the so called North-East-Down (NED) coordinate system. Both systems can be visually represented as shown in Fig.6.

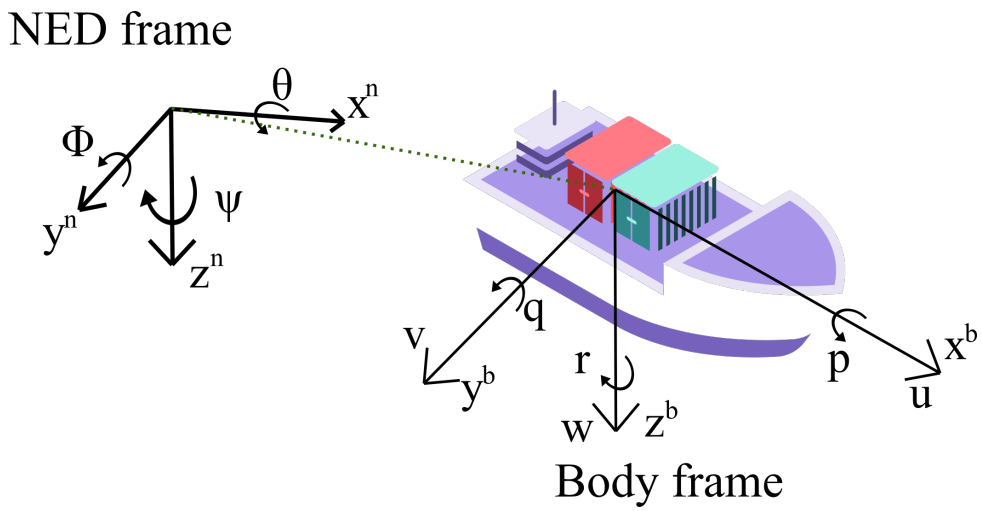

Figure 6: Visual representation of the NED and Body Frame coordinate system.

Following the notation in (FOSSEN, 2011), the coordinates in NED (η) and Body frame (ν) are related according to:

$$\begin{bmatrix} \dot{p}^n_{nb} \\ \dot{\Theta}_{nb} \end{bmatrix} = \begin{bmatrix} R(\Theta_{nb}) & 0_{3\times3} \\ 0_{3\times3} & T(\Theta_{nb}) \end{bmatrix} \begin{bmatrix} v^b_{nb} \\ \omega^b_{nb} \end{bmatrix} \Rightarrow \dot{\eta} = J_\Theta(\eta)\nu \tag{4.3}$$

With:

$$R(\Theta_{nb}) = \begin{bmatrix} \cos\theta\cos\psi & -\cos\phi\sin\psi + \sin\phi\sin\theta\cos\psi & \sin\phi\sin\psi + \cos\phi\sin\theta\cos\psi \\ \cos\theta\sin\psi & \cos\phi\cos\psi + \sin\phi\sin\theta\sin\psi & -\sin\phi\cos\psi + \cos\phi\sin\theta\sin\psi \\ -\sin\theta & \sin\phi\cos\theta & \cos\phi\cos\theta \end{bmatrix},$$

$$T(\Theta_{nb}) = \begin{bmatrix} 1 & \sin\phi\tan\theta & -\cos\phi\tan\theta \\ 0 & \cos\phi & -\sin\phi \\ 0 & \sin\phi/\cos\theta & \cos\phi/\cos\theta \end{bmatrix} \tag{4.4}$$

Simplifying for the plane O_{xy}:

$$R(\Theta_{nb}) = \begin{bmatrix} \cos\psi & -\sin\psi & 0 \\ \sin\psi & \cos\psi & 0 \\ 0 & 0 & 1 \end{bmatrix}, T(\Theta_{nb}) = \begin{bmatrix} 1 & 0 & \delta\theta \\ 0 & 1 & -\delta\phi \\ 0 & \delta\phi & 1 \end{bmatrix} \tag{4.5}$$

4.2 Maneuvering dynamics formulation

According to Fossen (FOSSEN, 2011), the maneuvering equation of a vessel motion without any ocean currents can be represented by:

$$M\dot{\underline{\nu}} + C(\underline{\nu})\underline{\nu} + D(\underline{\nu})\underline{\nu} + g(\underline{\eta}) + g_0 = \tau \tag{4.6}$$

Such that $\underline{\nu} = [u, v, w, p, q, r]^T$ is the state vector of all six velocities DoF in the Body Frame.

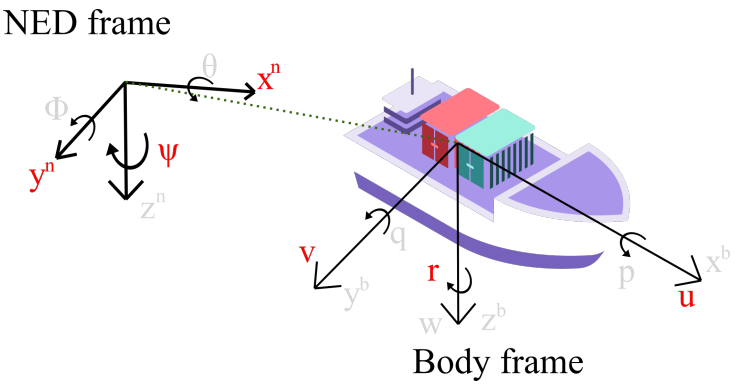

Figure 7: Visual representation of the adopted coordinate system and relevant coordinates.

As this work is focused only in the 2D horizontal plane xy, the shown system in Fig.6 can be reduced to Fig.7, the coordinates of interest are detached in red.

4.2.1 Mass matrix

The matrix is divided into the rigid-body and added mass component. While the former refers to an innate characteristic of a body, the latter can be seen as a virtual mass added to a system due to the surrounding fluid displacement caused by its movement, rigorously, it is a force that is proportional to the acceleration – or the drift volume displaced multiplied by the fluid density (DARWIN, 1953). In the same spirit, Newman (NEWMAN, 1977) explained it as being a weighted integration of the entire mass of the fluid particles that are accelerated with the body.

Through the lens of the Seakeeping Theory (FOSSEN, 2011), which concerns in the study of the craft motion when there is wave excitation while keeping a constant heading and speed (including zero-speed), the term of added mass is described as a function of frequency $A(\omega)$. The vessel dynamics can then be described by the Cummins equation (NEWMAN, 1977):

$$(-\omega^2[M_{RB} + A(\omega)] - j\omega B_{\text{total}}(\omega) + C)\xi(j\omega) = \tau_{wind}(j\omega) + \tau_{wave}(j\omega) + \delta\tau(j\omega) \quad (4.7)$$

Where $\delta\tau$ is the perturbed control input due to propulsion and control surfaces; B_{total} is the damping matrix containing potential and viscous damping terms; C is the spring stiffness matrix; τ's are the other external input forces from wind and wave and ξ is the perturbations in the 6 DoF. Fluid-memory effects become relevant and in an experimental setup, it is possible to control some of these terms, retaining merely with:

$$M_{RB}\ddot{\xi} = \overbrace{-A(\omega)\ddot{\xi} - B(\omega)\dot{\xi} - C\xi}^{\tau_{hyd}+\tau_{hs}} + f\cos(\omega t) \quad (4.8)$$

With τ_{hyd} and τ_{hs} referring to the hydrodynamic and hydrostatic forces due to surrounding water, by exposing the system to several frequencies, both terms of added mass $A(\omega)$ and damping $B(\omega)$ can be calculated. The aforementioned experiment can be made in a wave basin with a scaled model or can also be calculated purely numerically through different approaches such as with the strip theory, panel methods or semi-empirical methods (FOSSEN, 2011).

Nonetheless, this work focuses on the Maneuvering Theory (FOSSEN, 2011), assuming the ship is moving in restricted calm, sheltered waters or in a harbor. The maneuvering model is derived for a ship moving at a positive speed under a zero-frequency wave excitation assumption, in which the added mass and damping can be represented by using constant parameters or hydrodynamic derivatives. The usage of zero-frequency values is restricted to the surge, sway and yaw as their values are very distant from their natural frequencies counterparts. Such separation enables simplifications that can be made to facilitate calculations.

$$
\begin{gathered}
M = M_{RB} + M_A, \\
M_{RB} = \begin{bmatrix} m & 0 & -my_G \\ 0 & m & mx_G \\ -my_G & mx_G & I_z \end{bmatrix}, M_A = -\begin{bmatrix} X_{\dot{u}} & X_{\dot{v}} & X_{\dot{r}} \\ Y_{\dot{u}} & Y_{\dot{v}} & Y_{\dot{r}} \\ N_{\dot{u}} & N_{\dot{v}} & N_{\dot{r}} \end{bmatrix}
\end{gathered} \tag{4.9}
$$

4.2.2 Coriolis-centripetal matrix

Related to the rotation of the vessel frame relative to the inertial one, it can be also separated into two terms of rigid-body and added mass.

$$
\begin{gathered}
C(\underline{\nu}) = C_{RB}(\underline{\nu}) + C_A(\underline{\nu}), \\
C_{RB}(\underline{\nu}) = \begin{bmatrix} 0 & 0 & -m(x_G r + v) \\ 0 & 0 & -m(y_G r - u) \\ -I_{yz} r & I_{xz} r & 0 \end{bmatrix}, C_A(\underline{\nu}) = \begin{bmatrix} 0 & 0 & a_2 \\ 0 & 0 & -a_1 \\ -a_2 & a_1 & 0 \end{bmatrix}
\end{gathered} \tag{4.10}
$$

With a_1 and a_2 being functions in terms of u, v, r:

$$
\begin{cases} a_1(u,v,r) & = X_{\dot{u}} u + X_{\dot{v}} v + X_{\dot{r}} r \\ a_2(u,v,r) & = Y_{\dot{u}} u + Y_{\dot{v}} v + Y_{\dot{r}} r \end{cases} \tag{4.11}
$$

4.2.3 Damping matrix

Considering a ship moving with constant velocity U on the free surface, the resulting drag can be written as:

$$
D = \frac{1}{2} \rho S U^2 C_D(R_n, F_n) \tag{4.12}
$$

Where ρ is the water density, S is the wetted surface of the hull and F_n, the Froude number that represents the effect of gravity (4.2).

Remounting the Froude's hypothesis (NEWMAN, 1977; MOLLAND; TURNOCK; HUDSON, 2017), the drag coefficient C_D can be expressed by two separate parts: a sum of a frictional-drag coefficient C_F depending on the Reynolds number R_n and a residual-drag coefficient C_R depending on the Froude number F_n.

$$C_D(R_n, F_n) \approx C_F(R_n) + C_R(F_n) \tag{4.13}$$

Although very practical as now it is possible to scale separately Reynolds and Froude number, and by assuming that all resistance in excess C_R scales according to Froude's law, one can easily calculate the total drag coefficient from scaled model experiments:

$$C_R^{ship} = C_R^{model} \Rightarrow C_D^{ship} = C_D^{model} - (C_F^{model} - C_F^{ship}) \tag{4.14}$$

This approach tends to diverge from the actual C_D as the viscous resistance C_R does not scale exactly accordingly to Froude's law, resulting in over-estimations for very large ships. A more acceptable proposition was made by Hughes (LEWIS, 1988), in which it is assumed that the total viscous resistance (friction and form) scales according to Reynolds' law:

$$C_D = (1 + k)C_F + C_W = C_V + C_W \tag{4.15}$$

The term $(1 + k)$ is the form factor which depends on the hull form, C_F would now represent the skin friction coefficient based on a flat-plate, the composition of both C_V is the viscous coefficient, which considers the skin friction along with the pressure resistance, and finally C_W is the wave resistance coefficient.

Analogous to (4.14), on the basis of Froude's law:

$$C_W^{ship} = C_W^{model} \Rightarrow C_D^{ship} = C_D^{model} - (1 + k)(C_F^{model} - C_F^{ship}) \tag{4.16}$$

Molland, Turnock and Hudson (MOLLAND; TURNOCK; HUDSON, 2017) mention a plethora of model experiments to obtain the form factor directly or indirectly, some of them that can be mentioned is from running tests at low Froude values until C_D runs parallel with C_F (Fig.8 left), in which then:

$$C_W \to 0 \Rightarrow (1 + k) = \frac{C_D}{C_F} \tag{4.17}$$

Another method is a modified version introduced by Prohaska (LEWIS, 1988) (Fig.8 right), with:

$$\frac{C_D}{C_F} = (1+k) + A\frac{Fr^n}{C_F} \tag{4.18}$$

Where n, A and k are derived from a least-squares approximation.

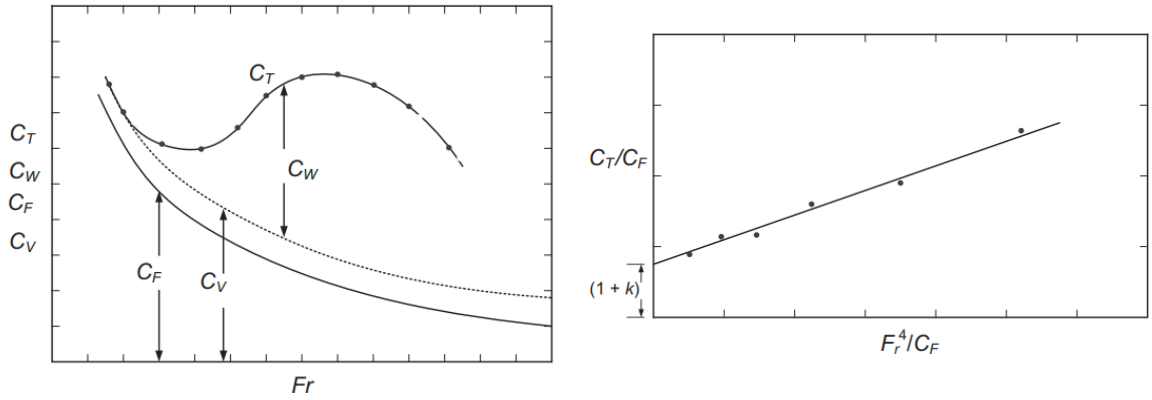

Figure 8: Experimental plots to retrieve form factor (extracted from (MOLLAND; TURNOCK; HUDSON, 2017)).

An approach based purely on the general dimensions of the ship was proposed by Hoerner (HOERNER, 1965):

$$(1+k) = 1 + 1.5\left(\frac{d}{l}\right)^{3/2} + 7\left(\frac{d}{l}\right)^{3} \tag{4.19}$$

With l being the length and d the diameter approximation for the hull.

Parting from recommendations from the International Towing Tank Conference (ITTC) in 1970s, a new method was most accepted to better implement correlation factors besides one overall such as $(1+k)$. The method, known as the 1978 ITTC Performance Prediction Method for Single Screw Ships (ITTC, 2017), composes the total resistance coefficient as:

$$C_D = (1+k)C_F + C_W + \Delta C_F + C_A + C_{AA} \tag{4.20}$$

The residual resistance C_R from ITTC is essentially the wave resistance C_W from (4.15). The term C_{AA} refers to the air resistance, which tackles the fluid interaction with the ship windage area (area exposed directly to the wind) and, thus, can be neglected for the scope of this work. The roughness allowance ΔC_F is calculated by:

$$\Delta C_F = 0.044\left(\left(\frac{k_s}{L_{pp}}\right)^{\frac{1}{3}} - 10{R_n}^{-\frac{1}{3}}\right) + 0.000125 \tag{4.21}$$

With k_s indicating the roughness of the hull surface, admitting a value of $150 \times 10^{-6} m$ when there is no measured data. Finally, the correlation allowance C_A is determined from comparison between model and full scale trials results. If using the standardized mentioned value, it can be calculated by:

$$C_A = (5.68 - 0.6 \log R_n) \times 10^{-3} \tag{4.22}$$

Fossen (FOSSEN, 2011) opted to work with the proposal from Hughes (4.15) to elaborate the damping in surge $\Gamma_u(\nu)$, that is proportional to the quadratic relative surge velocity u_r:

$$\begin{aligned} C_f(u_r) &= \overbrace{\frac{0.075}{(\log_{10} R_n - 2)^2}}^{C_F} + C_R \\ \Gamma_u(\nu) &= \underbrace{-\frac{1}{2}\rho S(1+k) C_f(u_r)}_{X_{|u|u}} |u_r| u_r \end{aligned} \tag{4.23}$$

Recalling that C_F is the flat plate friction from the ITTC 1957 line, the damping in surge $\Gamma_u(\nu)$ is a function of the wetted surface of the hull S and the density of the water ρ. The force is proportional to the quadratic relative velocity in surge u_r (which subtracts the influence of external current velocity V_c):

$$V_c = \sqrt{u_c^2 + v_c^2} \;\; \Rightarrow \begin{cases} u_r = u - u_c \\ v_r = v - v_c \end{cases} \tag{4.24}$$

Fig.9 illustrates both mentioned velocities vectors acting in a vessel.

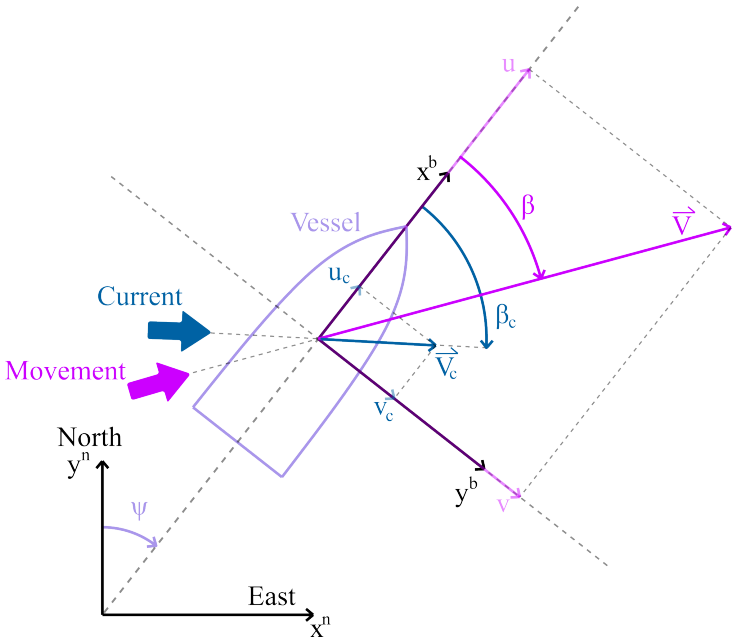

Figure 9: Visual representation of the incident current and drift angles.

Fig.10 illustrates how the water relative speed is constructed by the ship advance speed and the current speed. For the case of a non-existent external current ($u_c = v_c = 0$), the water relative speed becomes essentially the advance speed of the ship: $u_r = u$ and $v_r = v$.

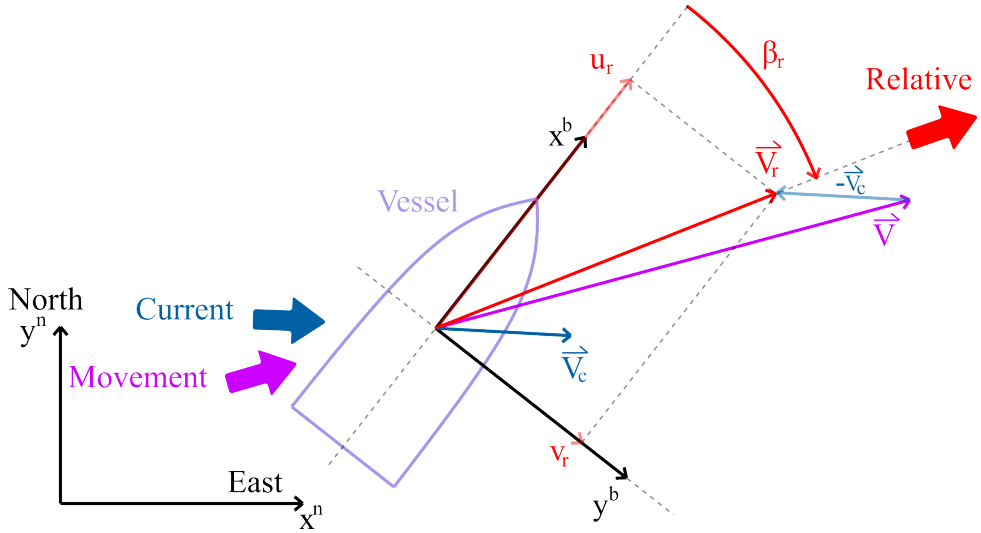

Figure 10: Visual representation of the angles mentioned in (4.24).

Due to C_F being inversely proportional to the Reynolds number, this coefficient will tend to infinity at low speeds, as such, Fossen mentions that a minimum value should be typically assigned, in the case for ships, $R_{n,min} = 10^6$. In this low speed scenario, in order to obtain sufficient damping, Fossen further modifies the damping term $X_{|u|u}$ and the resistance coefficient itself in (4.23) to:

$$
\begin{aligned}
X_{|u|u}^{slow} &= \frac{1}{2}\rho A_x C_X^{new} \quad C_X^{new} = \frac{S}{A_x} C_f^{new} \\
C_f^{new}(u_r) &= C_f(u_r^{max}) + \left(\frac{A_x}{S} C_X - C_f(u_r^{max}) \right) \exp\left(-\alpha u_r^2\right)
\end{aligned}
\tag{4.25}
$$

With A_x being the frontal project area, $C_f(u_r^{max})$, the maximum friction coefficient computed for maximum relative velocity u_r^{max}, $\alpha > 0$, a weight that makes the exponential term vanishes at higher speeds. By inspecting Fig.11, even by this singular example, one can see the higher values of the C_f^{new} for low speeds in comparison with C_f, allowing better simulation fidelity for these scenarios.

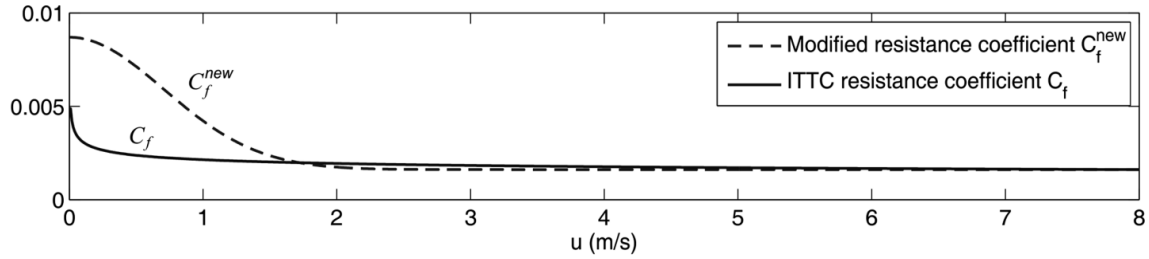

Figure 11: Comparison between the modified resistance curve with the ITTC one in a particular unspecified vessel, extracted from (FOSSEN, 2011).

Nonetheless, Fossen recommends the usage of different damping models depending on the regime of the system. In Fig.12, in the context of Dynamic Positioning control systems, this limit was set around 2 m/s.

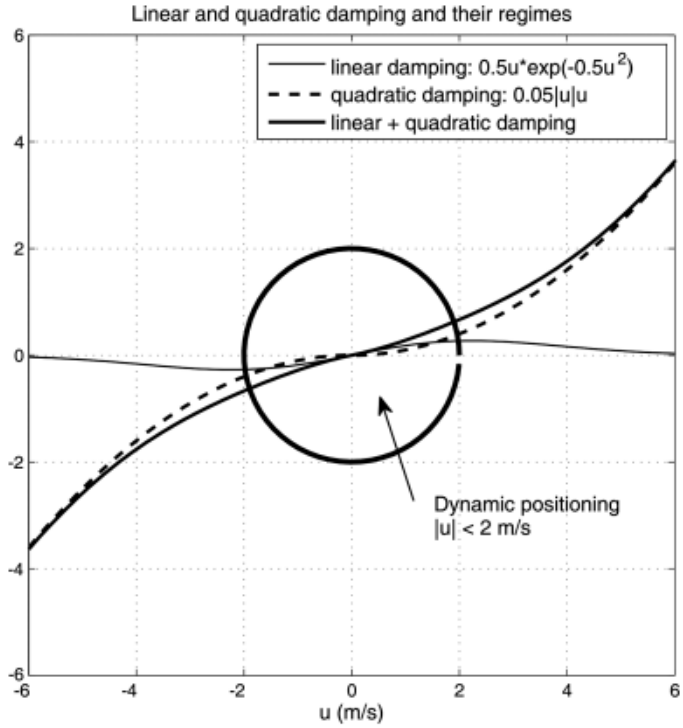

Figure 12: Graphical representation of the linear and quadratic damping regimes in a Dynamic Positioning control scenario. (extracted from (FOSSEN, 2011))

For sway force and yaw moment, Faltinsen (FALTINSEN, 1993) introduced the cross-flow principle to calculate these components:

$$\begin{aligned}\Gamma_v(\nu) &= -\frac{1}{2}\rho \int_{-\frac{L_{pp}}{2}}^{\frac{L_{pp}}{2}} T(x) C_d^{2D}(x) |v_r + xr|(v_r + xr) dx \\ \Gamma_r(\nu) &= -\frac{1}{2}\rho \int_{-\frac{L_{pp}}{2}}^{\frac{L_{pp}}{2}} T(x) C_d^{2D}(x) x |v_r + xr|(v_r + xr) dx\end{aligned} \tag{4.26}$$

With $C_d^{2D}(x)$ being the 2-D drag coefficient and $T(x)$ being the draft at each section along the x-axis; and v_r being the sway relative velocity defined in (4.24).

Obokata (OBOKATA, 1987) proposed another method to include this cross-flow model, replacing the evaluation by section with more general coefficients C_x, C_y and C_z. Such terms can be easily obtained by captive towing-tank tests or CFD calculation – for both shallow and deep waters – as they now varies with the incident water stream direction, which in maneuvering terms, can be calculated as:

$$\beta = \arctan\left(\frac{v}{u}\right) \tag{4.27}$$

Another idea introduced by Obokata is that the draft does not need to be known at each section, instead, the coefficients themselves would absorb some knowledge of the hull shape.

Fucatu and Nishimoto (FUCATU; NISHIMOTO, 2004) expanded the method from Obokata to consider a non-uniform current field $\vec{V}_C(X, Y)$, leading to an integral by section of the current profile instead. A variation of this formulation can be seen in (TANNURI et al., 2014):

$$\begin{aligned}
\Gamma_u(\nu) &= \frac{1}{2}\rho T \int_{-L/2}^{L/2} C_x(\psi_{crx}) V_{crx}^2 dx \\
\Gamma_v(\nu) &= \frac{1}{2}\rho T \int_{-L/2}^{L/2} C_y(\psi_{crx}) V_{crx}^2 dx \\
\Gamma_r(\nu) &= \frac{1}{2}\rho T \int_{-L/2}^{L/2} \left(C_y(\psi_{crx}) V_{crx}^2 - C_y(\psi_{cr}) V_{cr}^2\right) x dx + \frac{1}{2}\rho T L^2 C_z(\psi_{cr}) V_{cr}^2
\end{aligned} \tag{4.28}$$

With the subscript crx representing the speed of the section x from the vessel midships related to the water and the cr, the relative speed at exactly midships $x = 0$. Tannuri et al. (TANNURI et al., 2014) further developed these hydrodynamic forces to include a self induced ship rotation, as can be seen in the integral terms, throwing back in a similar manner as the formulation from Faltinsen (4.26), replacing the section dependency in the draft $T(x)$ and drag coefficient $C_d^{2d}(x)$ towards the Obokata coefficients $C_x(\psi_{crx}), C_y(\psi_{crx}), C_z(\psi_{crx})$.

Fig.13 better illustrates how Tannuri et al. considered the speed variation at each section (reinforcing that the system adopted there is slightly different from this work).

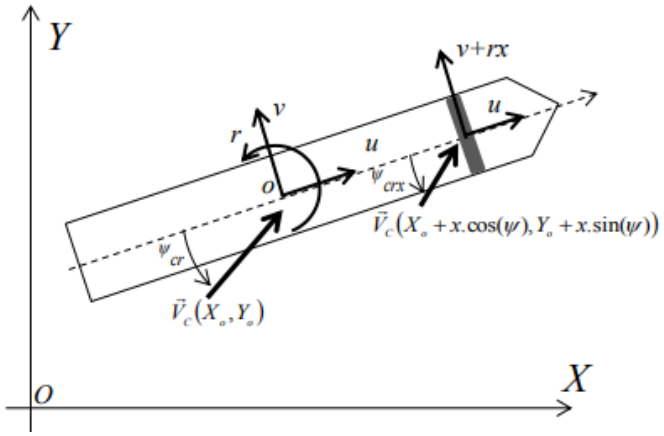

Figure 13: Notation adopted in (TANNURI et al., 2014) according to its original reference system.

Rewriting (4.28) into the system coordinates adopted in this work, the damping matrix will be given by:

$$D(\nu) = \begin{bmatrix} \Gamma_u(\nu) \\ \Gamma_v(\nu) \\ \Gamma_r(\nu) \end{bmatrix} = \begin{bmatrix} -\frac{1}{2}\rho T \int_{-\frac{L}{2}}^{\frac{L}{2}} C_x(\beta_{crx}) V_{crx}^2 dx \\ -\frac{1}{2}\rho T \int_{-\frac{L}{2}}^{\frac{L}{2}} C_y(\beta_{crx}) V_{crx}^2 dx \\ -\frac{1}{2}\rho T \int_{-\frac{L}{2}}^{\frac{L}{2}} \left(C_y(\beta_{crx}) V_{crx}^2 - C_y(\beta_{cr}) V_{cr}^2 \right) x dx - \frac{1}{2}\rho T L^2 C_z(\beta_{cr}) V_{cr}^2 \end{bmatrix} \tag{4.29}$$

These integrals were expanded in Appendix A.1 according to the simplification adopted later in 6.2.

4.2.4 Hydrostatic and external forces

Hydrostatic forces are the restoring forces responsible for maintaining the buoyancy of the craft. While being essential to the minimal requirement of a vessel, as their major components are present in the z-axis, roll and pitch, for this work the terms $g(\underline{\eta})$ and g_0 can be neglected.

For the external forces τ, the propeller, rudder and environment are expected to be in here. As this work focused into the estimation analysis, the maneuvers were executed in calm waters with no wind nor currents. Both propeller and rudder dynamics are considered and will be presented in 4.3.1 and 4.3.2, as they have their own specificities.

4.2.5 Complete 3 DoF formulation

Finally the maneuvering equation can be compiled as:

$$\begin{bmatrix} m - X_{\dot{u}} & -X_{\dot{v}} & -my_G - X_{\dot{r}} \\ Y_{\dot{u}} & m - Y_{\dot{v}} & mx_G - Y_{\dot{r}} \\ -my_G - N_{\dot{u}} & mx_G - N_{\dot{v}} & I_z - N_{\dot{r}} \end{bmatrix} \begin{pmatrix} \dot{u} \\ \dot{v} \\ \dot{r} \end{pmatrix} + \begin{bmatrix} \Gamma_u(\nu) \\ \Gamma_v(\nu) \\ \Gamma_r(\nu) \end{bmatrix} + \begin{bmatrix} 0 & 0 & -m(x_G r + v) + a_2 \\ 0 & 0 & -m(y_G r - u) - a_1 \\ -I_{yz} r - a_2 & I_{xz} r + a_1 & 0 \end{bmatrix} \begin{pmatrix} u \\ v \\ r \end{pmatrix} = \begin{pmatrix} \tau_u \\ \tau_v \\ \tau_r \end{pmatrix} \tag{4.30}$$

4.3 External forces as modular models

Although well-established, (4.30) is not necessarily the basis for System Identification studies with physics-based models as already discussed in 3.3. Some of the aforementioned formulations have general parameters with correlated states influence (surge-sway, sway-yaw, for example) that encompass joint effects, such as some of the Coriolis forces are merged with the damping merely because both would have a quadratic surge speed dependency. These models can be also known as hydrodynamics derivative models and while for their specific context it is already sufficient, as with then one can define how the ship would behave dynamically, they lack crucially in the interpretability domain – a characteristic that can easily fit in as one of the pillars of a DT application.

The model of Abkowitz (ABKOWITZ, 1964) clearly exemplifies this approach by developing the forces and moment acting in the vessel through Taylor series expansion up to the second-order:

$$
\begin{aligned}
X(x) &\approx X(x_0) + \sum_{i=1}^{n} \left(\frac{\partial X(x)}{\partial x_i}\bigg|_{x_0} \Delta x_i + \frac{1}{2}\frac{\partial^2 X(x)}{(\partial x_i)^2}\bigg|_{x_0} \Delta x_i^2 + \frac{1}{6}\frac{\partial^3 X(x)}{(\partial x_i)^3}\bigg|_{x_0} \Delta x_i^3 \right) \\
Y(x) &\approx Y(x_0) + \sum_{i=1}^{n} \left(\frac{\partial Y(x)}{\partial x_i}\bigg|_{x_0} \Delta x_i + \frac{1}{2}\frac{\partial^2 Y(x)}{(\partial x_i)^2}\bigg|_{x_0} \Delta x_i^2 + \frac{1}{6}\frac{\partial^3 Y(x)}{(\partial x_i)^3}\bigg|_{x_0} \Delta x_i^3 \right) \\
N(x) &\approx N(x_0) + \sum_{i=1}^{n} \left(\frac{\partial N(x)}{\partial x_i}\bigg|_{x_0} \Delta x_i + \frac{1}{2}\frac{\partial^2 N(x)}{(\partial x_i)^2}\bigg|_{x_0} \Delta x_i^2 + \frac{1}{6}\frac{\partial^3 N(x)}{(\partial x_i)^3}\bigg|_{x_0} \Delta x_i^3 \right) \\
&\text{with: } x = [u, v, r, \dot{u}, \dot{v}, \dot{r}, \delta]^T,\ x_0 = [U, 0, 0, 0, 0, 0, 0]^T,\ \Delta x = x - x_0
\end{aligned}
\tag{4.31}
$$

By expanding (4.31) along with some physical insights, the expressions become:

$$
\begin{aligned}
X =& X^* + X_{\dot{u}}\dot{u} + X_u\Delta u + X_{uu}\Delta u^2 + X_{uuu}\Delta u^3 + X_{vv}v^2 + X_{rr}r^2 + X_{\delta\delta}\delta^2 \\
&+ X_{rv\delta}rv\delta + X_{r\delta}r\delta + X_{v\delta}v\delta + X_{vvu}v^2\Delta u + X_{rru}r^2\Delta u + X_{\delta\delta u}\delta^2\Delta u \\
&+ X_{rvu}rvu + X_{r\delta u}r\delta\Delta u + X_{v\delta u}v\delta\Delta u \\
Y =& Y^* + Y_u\Delta u + Y_{uu}\Delta u^2 + Y_r r + Y_v v + Y_{\dot{r}}\dot{r} + Y_{\dot{v}}\dot{v} + Y_\delta\delta + Y_{rrr}r^3 + Y_{vvv}v^3 \\
&+ Y_{\delta\delta\delta}\delta^3 + Y_{rr\delta}r^2\delta + Y_{\delta\delta r}\delta^2 r + Y_{rrv}r^2 v + Y_{vvr}v^2 r + Y_{\delta\delta v}\delta^2 v + Y_{vv\delta}v^2\delta + Y_{\delta vr}\delta vr \\
&+ Y_{vu}v\Delta u + Y_{vuu}v\Delta u^2 + Y_{ru}r\Delta u + Y_{ruu}r\Delta u^2 + Y_{\delta u}\delta\Delta u + Y_{\delta uu}\delta\Delta u^2 \\
N =& N^* + N_u\Delta u + N_{uu}\Delta u^2 + N_r r + N_v v + N_{\dot{r}}\dot{r} + N_{\dot{v}}\dot{v} + N_\delta\delta + N_{rrr}r^3 + N_{vvv}v^3 \\
&+ N_{\delta\delta\delta}\delta^3 + N_{rr\delta}r^2\delta + N_{\delta\delta r}\delta^2 r + N_{rrv}r^2 v + N_{vvr}v^2 r + N_{\delta\delta v}\delta^2 v + N_{vv\delta}v^2\delta \\
&+ N_{\delta vr}\delta vr + N_{vu}v\Delta u + N_{vuu}v\Delta u^2 + N_{ru}r\Delta u + N_{ruu}r\Delta u^2 + N_{\delta u}\delta\Delta u + N_{\delta uu}\delta\Delta u^2
\end{aligned}
\tag{4.32}
$$

Apart from being derivatives from the forces or moment, these parameters do not always carry directly a physical significance by their own, they mainly exist, after being extracted through interpolated curves in a post-processing phase after conducting experiments such as the towing tank tests.

Other common characteristic noted is that none of them showed a concern in formulating some real physics representation of the propulsion or steering mechanisms. In the next sections 4.3.1 and 4.3.2, some formulation is explored intending to achieve a higher degree of linkage towards physical phenomena. The forces and moment generated by both will enter in (4.30) through the terms τ_i.

4.3.1 Propeller thrust formulation

The propeller is the traditional major device responsible for moving the ship composed by a set of blades as schematized in Fig.5, usually being divided into two main categories: the Fixed pitch propeller (FP-propeller) or the Controllable pitch propeller (CP-propeller). While the former is fixed to the ship hull, similar to the setup shown in Fig.4, the latter has a setup that enables the tilt movement in the pitch axis. Nonetheless, both are the most common solutions applied to a vast number of ships that operate mainly at sea and does not require complex controls.

Albeit the fluid flow is the main physic phenomenon that explains the total generated thrust force for the vessel to displace in water – therefore relying in results from CFD with individualities specific to each studied model – dimensionless coefficients were introduced

to simplify this theory and allow a faster assessment with enough accuracy, as it can be found in (FOSSEN, 2011) and (STAPERSMA; WOUD, 2005).

An algorithm to retrieve the generated thrust from a fixed single-screw propeller starts by retrieving the water relative speed at the propeller (u_P):

$$u_P = (1 - w_P)u \tag{4.33}$$

With w_P being the wake factor of the propeller, essentially condensing the whole information of hull-propeller interaction. Next, the advance number of the propeller (J_P), a dimensionless expression representing the speed of advance of the propeller, is defined as:

$$J_P(u, n) = \begin{cases} \dfrac{u_P}{nD_P}, & \text{if } n \neq 0 \\ 1, & \text{if } n = 0 \end{cases} \tag{4.34}$$

with n being the rate of the revolution and D_P its diameter.

By knowing the advance number, it is possible to obtain the motor thrust constant K_T through interpolating the curve given by the manufacturer, then the thrust force F^{thr} can be expressed as:

$$F^{thr}(u, n) = \rho n^2 D_P^4 K_T(J_P) \tag{4.35}$$

With ρ being the mass density of the water. This force is mainly applied on the longitudinal direction of the vessel, thus:

$$\tau^{thr}(u, n) = \begin{bmatrix} F^{thr}(u, n) \\ 0 \\ 0 \end{bmatrix} \tag{4.36}$$

4.3.2 Rudder forces and moment formulation

Regarding the steering control system in a ship, the rudder is the uppermost apparatus. In its most common form it is shaped as a flat plane projected to minimize the hydrodynamic drag. As it operates on the principle of unequal water pressures, it is usually placed at the stern and right behind the propeller to better performs. When

requested, one side becomes more exposed to the water flowing than the other, generating an initial lift force that slightly rotates the vessel in yaw, then the hull itself generates the remaining differential moment responsible to steer the ship. Thus, the rudder itself acts as a trigger to the steering process.

As the water flow is an essential component in the rudder action, knowing the velocity at the rudder position is the initial step to obtain the desired forces and moments. Accordingly to Kose et al. in (KOSE; YUMURO; YOSHIMURA, 1981), the water longitudinal speed component can be calculated by:

$$u_R = \varepsilon u_P \sqrt{\eta \left\{ 1 + \kappa \left(\sqrt{1 + \frac{8K_T}{\pi J_P^2}} - 1 \right) \right\}^2 + (1 - \eta)} \tag{4.37}$$

Being η the ratio of the propeller diameter to the rudder span, with $\eta = 1$ standing as a good approximation from empirical knowledge (LIU; HEKKENBERG, 2017); $\varepsilon = \frac{1-w_R}{1-w_P}$, the ration of wake fraction at propeller and ruder positions; and κ, an experimental constant approximated to $\kappa = \frac{0.6}{\varepsilon}$ (KOSE; YUMURO; YOSHIMURA, 1981). The terms u_P, J_P and K_T are obtained by (4.33) and (4.34).

Yasukawa and Yoshimura (YASUKAWA; YOSHIMURA, 2015) summarize the lateral speed component, yet, they include a correction for the flow straightening phenomena, leading to a formula with some experimental parameters. Aiming a more general application, this method simplified it to only consider the rudder position towards its center of gravity:

$$v_R = v + r(x_R - x_G) \tag{4.38}$$

Related to fomulation in (4.27), the drift angle β_R and the absolute speed at rudder position V_R can both be defined as:

$$V_R = \sqrt{u_R^2 + v_R^2}, \quad \beta_R = \arctan\left(\frac{v_R}{u_R}\right) \tag{4.39}$$

By ignoring the flow straightening phenomena (MOLLAND; TURNOCK, 2007), the rudder inflow angle α_R can be described as:

$$\alpha_R = \delta + \beta_R \tag{4.40}$$

Being δ the actual rudder deflection angle, which can be obtained though the demanded angle. Once calculated α_R, it is possible to retrieve the correspondent drag $C_D(\alpha_R)$ and $C_L(\alpha_R)$ (4.1.1). Thence, its forces on a typical single-screw ship can be calculated by:

$$\begin{aligned} F_D &= \frac{1}{2}\rho S_R C_D(\alpha_R) V_R^2 \\ F_L &= \frac{1}{2}\rho S_R C_L(\alpha_R) V_R^2 \end{aligned} \tag{4.41}$$

Finally, translating into the Body frame coordinate system, as visually represented in Fig.14:

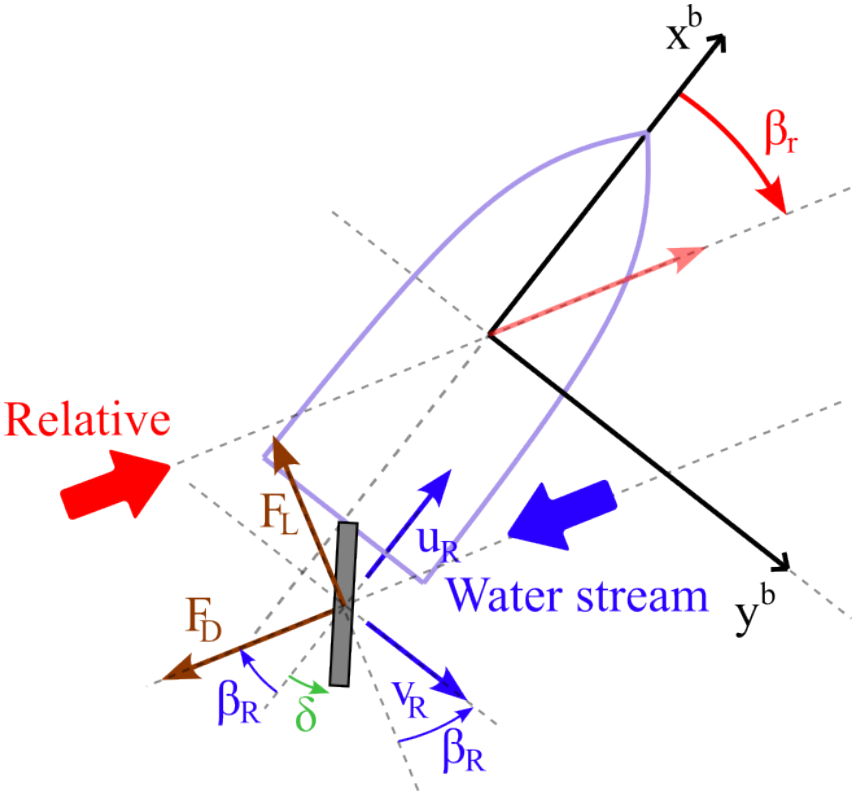

Figure 14: Visual representation of the rudder actuating forces.

$$\begin{aligned} F_x^{rud}(\nu,\delta) &= -F_D \cos\beta_R + F_L \sin\beta_R \\ F_y^{rud}(\nu,\delta) &= -F_D \sin\beta_R - F_L \cos\beta_R \\ M_z^{rud}(\nu,\delta) &= (x_R - x_G)F_y^{rud} - (y_R - y_G)F_x^{rud} \end{aligned} \tag{4.42}$$

And uniforming to the adopted nomenclature:

$$\tau^{rud}(\nu,\delta) = \begin{bmatrix} F_x^{rud}(\nu,\delta) \\ F_y^{rud}(\nu,\delta) \\ M_z^{rud}(\nu,\delta) \end{bmatrix} \tag{4.43}$$

5 KALMAN FILTER METHODOLOGY

Kalman Filter (KF) is the optimal full-state estimator given the Gaussian white noise disturbances of the modeling and the measurement processes.

5.1 Kalman Filter (KF)

Named after Rudolf E. Kálmán by its firsts studies in (KALMAN, 1960), KF consists of an algorithm that combines received measurements with knowledge of the interested system dynamics along with each of the correspondent uncertainties to produce better estimations. Widely applied in countless domains, its discrete formulation (LEWIS; XIE; POPA, 2017) begins by the description of the linear system and measurement model:

$$\begin{aligned} x_{k+1} &= A_k x_k + B_k u_k + G_k w_k \\ z_k &= H_k x_k + v_k \end{aligned} \tag{5.1}$$

Being $x \in R^n$ the modeled states, $u \in R^m$ the system input and $z \in R^p$ the measurements in vector form; A, B and H are matrices that correlate the dynamics and measurements evolution in terms of the mentioned terms. Both process noise w_k and measurement noise v_k are assumed to be stationary white noise processes with zero mean $w_k \sim (0, Q_k)$ and $v_k \sim (0, R_k)$. The subscript indicates the discrete time step k.

5.1.1 Prediction phase

Given an initial condition for the estimate $x_0 \sim (\bar{x}_0, P_{x_0})$, the procedure starts with the time update, in which a prediction is taken purely considering the system dynamics:

$$\begin{aligned} &\text{Error covariance } \textit{a priori}: && P_{k+1}^- = A_k P_k A_k^T + G_k Q_k G_k^T \\ &\text{Estimate } \textit{a priori}: && \hat{x}_{k+1}^- = A_k \hat{x}_k + B_k u_k \end{aligned} \tag{5.2}$$

5.1.2 Correction phase

Next, enters the measurement update, in which a correction is applied to these previous terms:

$$\begin{aligned} &\text{Kalman gain:} && K_{k+1} = P^-_{k+1} H^T_{k+1} (H_{k+1} P^-_{k+1} H^T_{k+1} + R_{k+1})^{-1} \\ &\text{Error covariance } \textit{a posteriori}\text{:} && P_{k+1} = (I - K_{k+1} H_{k+1}) P^-_{k+1} \\ &\text{Estimate } \textit{a posteriori}\text{:} && \hat{x}_{k+1} = \hat{x}^-_{k+1} + K_{k+1}(z_{k+1} - H_{k+1}\hat{x}^-_{k+1}) \end{aligned} \tag{5.3}$$

These relations are illustrated in Fig.15. The estimator will be optimal if the state variables have arbitrary statistics.

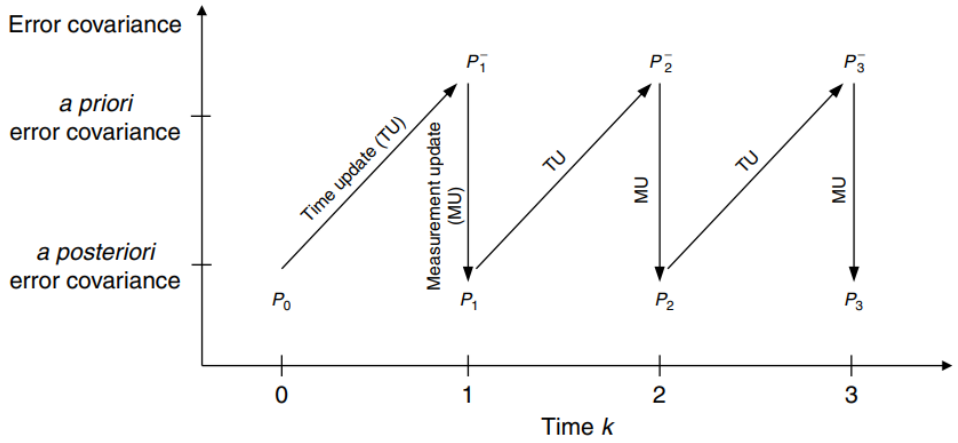

Figure 15: Diagram of the correction for the error covariance (extracted from (LEWIS; XIE; POPA, 2017)).

5.2 Extended Kalman Filter (EKF)

For nonlinear systems, one well known variation for the KF is the Extended Kalman Filter (EKF). By applying a linearization around a reference point at each time step, these nonlinearities can be then treated as linear system instantaneously, returning to a classical KF problem, as previously described in 5.1.

Consider a nonlinear continuous process dynamics and discrete measurements as:

$$\begin{aligned} \dot{x}(t) &= f(x(t), u(t)) + G(t)w(t) \\ z_k &= h(x_k) + v_k \end{aligned} \tag{5.4}$$

The jacobians are calculated as:

$$F(t) = \left.\frac{\partial f(x(t), u(t))}{\partial x(t)}\right|_{x(t)=\hat{x}(t),u(t)}, \quad H_k = \left.\frac{\partial h(x_k)}{\partial x_k}\right|_{x_k=\hat{x}_k^-} \tag{5.5}$$

5.2.1 Prediction phase

Thus, the time update equations in (5.2) are altered to:

$$\begin{aligned} \dot{\hat{x}}(t) &= f(\hat{x}(t), u(t)) \\ \dot{P}(t) &= F(t)P(t) + P(t)F^T(t) + GQG^T \end{aligned} \tag{5.6}$$

Apart from the shifting towards a time continuous representation, the predicted state vector $\hat{x}$ is now obtained via the nonlinear map given by $f(x(t), u(t))$ based on the previous estimate at $t - \Delta t$. As the measurements are still treated in discrete time, both $\hat{x}(t)$ and $P(t)$ are sampled by:

$$\begin{aligned} \hat{x}_k^- &= \hat{x}(k\Delta t) + \dot{\hat{x}}(t) \cdot \Delta t \\ P_k^- &= P(k\Delta t) + \dot{P}(t) \cdot \Delta t \end{aligned} \tag{5.7}$$

5.2.2 Correction phase

Finally, the measurement update equations from (5.3) can now be written as:

$$\begin{aligned} K_k &= P_k^- H_k^T (H_k P_k^- H_k^T + R_k)^{-1} \\ \hat{x}_k &= \hat{x}_k^- + K_k(z_k - \hat{y}_k^-), \quad \hat{y}_k^- = h(\hat{x}_k^-) \\ P_k &= (I - K_k H_k) P_k^- \end{aligned} \tag{5.8}$$

One of the major concerns of the EKF consists in the assumption that the states, which are taken as random variables following a Gaussian distribution, will still propagates this same behavior after the nonlinear mapping through $f(x(t), u(t))$. Besides stop being the optimal estimator in this context, problems such as stability or convergence could appear, along with numerous others mentioned in (MADYASTHA et al., 2011) and (JULIER; UHLMANN, 1997).

5.3 Unscented Kalman Filter (UKF)

Proposed by Julier and Uhlman (JULIER; UHLMANN, 1997), the Unscented Kalman Filter (UKF) presents an improvement in comparison with the EKF counterpart. As mentioned previously in 5.2, the propagation of a Gaussian random variable (GRV) along the evolution of the system dynamics is essential towards reaching the optimal estimation. In EKF, the state distribution itself is approximated by a GRV, which would not pose any issue when facing linear dynamics. However, as for nonlinear systems the procedure is to approximate into a first-order linearization, the true posterior mean and covariance of the transformed GRV can be affected, leading towards sub-optimal performance and even divergence.

By using a minimal set of carefully chosen sample points, the UKF addresses the previously mentioned problem, as these points completely capture the true mean and covariance of the GRV, achieving accuracy up to the 3rd order, even when propagated through nonlinear systems – in contrast with the EKF, which only reaches first-order accuracy.

5.3.1 Unscented Transformation (UT)

The Unscented transformation (UT) is a method for calculating the statistics of a random variable which undergoes a nonlinear transformation. Considering a random variable x, with $\bar{\mathrm{x}}$ mean and $\mathrm{P_x}$ covariance, the sigma vectors $\mathcal{X}_i$ are defined as:

$$\begin{aligned} \mathcal{X}_0 &= \bar{\mathrm{x}} \\ \mathcal{X}_i &= \bar{\mathrm{x}} + \left(\sqrt{(L+\lambda)\mathrm{P_x}}\right)_i \qquad i = 1, \ldots, L \\ \mathcal{X}_i &= \bar{\mathrm{x}} - \left(\sqrt{(L+\lambda)\mathrm{P_x}}\right)_{i-L} \qquad i = L+1, \ldots, 2L \end{aligned} \tag{5.9}$$

Each sigma vector has a corresponding weight W_i that will be used to adjust the mean $W_i^{(m)}$ and the covariance $W_i^{(c)}$:

$$\begin{aligned} W_0^{(m)} &= \frac{\lambda}{L+\lambda} \\ W_0^{(c)} &= \frac{\lambda}{L+\lambda} + (1 - \alpha^2 + \beta) \\ W_i^{(m)} &= W_i^{(c)} = \frac{1}{2(L+\lambda)} \qquad i = 1, \ldots, 2L \end{aligned} \tag{5.10}$$

With λ being a scaling parameter calculated as: $\lambda = \alpha^2(L + \kappa) - L$. While κ is a secondary scaling parameter, α determines the spread of the sigma points around $\bar{\mathrm{x}}$ and β incorporates prior knowledge of the distribution of x. The adding and subtracting term $\left(\sqrt{(L+\lambda)\mathrm{P_x}}\right)_i$ is the i-th row of the matrix square root.

Propagating these sigma vectors $\mathcal{X}_i$ through the nonlinear function:

$$\mathcal{Y}_i = g(\mathcal{X}_i), \qquad i = 0, \ldots, 2L \tag{5.11}$$

The mean $\bar{\mathrm{y}}$ and covariance $\mathrm{P_y}$ are then approximated by a weighted sample mean and covariance of the posterior sigma points:

$$\bar{\mathrm{y}} \approx \sum_{i=0}^{2L} W_i^{(m)} \mathcal{Y}_i \tag{5.12}$$

$$\mathrm{P_y} \approx \sum_{i=0}^{2L} W_i^{(c)} \{\mathcal{Y}_i - \bar{\mathrm{y}}\}\{\mathcal{Y}_i - \bar{\mathrm{y}}\}^T \tag{5.13}$$

The Unscented transformation (UT) is the first step in the UKF method.

5.3.2 Prediction phase

At the beginning of each step, an UT is performed with the estimates from previous step, following the same procedure presented before, starting from the generation of the sigma points:

$$\chi_{k-1} = \left[\hat{x}_{k-1} \quad \hat{x}_{k-1} + \gamma\sqrt{P_{k-1}} \quad \hat{x}_{k-1} - \gamma\sqrt{P_{k-1}}\right]_{(2L+1)\times L} \text{ with: } \gamma = \sqrt{L+\lambda} \tag{5.14}$$

These points are then mapped through the process dynamics, except that this time the result will be in a matrix format χ:

$$\mathcal{X}_k = f(\chi_{k-1}, u_{k-1}) \tag{5.15}$$

Analogously to equations (5.2) and (5.6), the *a priori* estimations will then be:

$$\begin{aligned} \hat{x}_k^- &= \sum_{i=0}^{2L} W_i^{(m)} \mathcal{X}_{i,k} \\ P_k^- &= \sum_{i=0}^{2L} W_i^{(c)} [\mathcal{X}_{i,k} - \hat{x}_k^-][\mathcal{X}_{i,k} - \hat{x}_k^-]^T + Q_k \end{aligned} \tag{5.16}$$

Essentially being the output of the UT as shown in (5.12) and (5.13).

5.3.3 Correction phase

Again, another UT is taken, but with the measurements instead. The mapping from (5.15) is now taken through the function h:

$$\mathcal{Y}_k = h(\mathcal{X}_k, u_{k-1}) \tag{5.17}$$

Thus, the estimated measurement $\hat{y}_k$ and its correspondent covariance P_k^y are:

$$\begin{aligned} \hat{y}_k &= \sum_{i=0}^{2L} W_i^{(m)} \mathcal{Y}_{i,k} \\ P_k^y &= \sum_{i=0}^{2L} W_i^{(c)} [\mathcal{Y}_{i,k} - \hat{y}_k][\mathcal{Y}_{i,k} - \hat{y}_k]^T + R_k \end{aligned} \tag{5.18}$$

Using the same idea, the cross covariance between the states and measurements are also calculated:

$$P_k^{xy} = \sum_{i=0}^{2L} W_i^{(c)} [\mathcal{X}_{i,k} - \hat{x}_k^-][\mathcal{Y}_{i,k} - \hat{y}_k]^T \tag{5.19}$$

Finally, the estimates can be corrected with:

$$\begin{aligned} K_k &= P_k^{xy} (P_k^y)^{-1} \\ \hat{x}_k &= \hat{x}_k^- + K_k (z_k - \hat{y}_k) \\ P_k &= P_k^- - K_k P_k^y (K_k)^T \end{aligned} \tag{5.20}$$

5.4 Kalman Filter with constraints

Albeit one can believe that with an application of the KF approach by itself should be enough to obtain optimal state estimations as it consists in minimizing the states variance, Simon (SIMON, 2010) breaks this misconception by mentioning two reasons:

- For nonlinear systems, the KF can only reach sub-optimal estimations as its variations are merely approximately minimum variances
- If there are additional constraints beyond those explicitly given in the system model inserted into the KF algorithm, then the within reached estimations differ from the complete system

Still in (SIMON, 2010), Simon presents a survey of how state constraints can be incorporated into the KF. The numerous possible approaches is such that he presents a flowchart (Fig.16) to help one navigate and find best suited formulation to implement, as they perform identically if the constraints are complete.

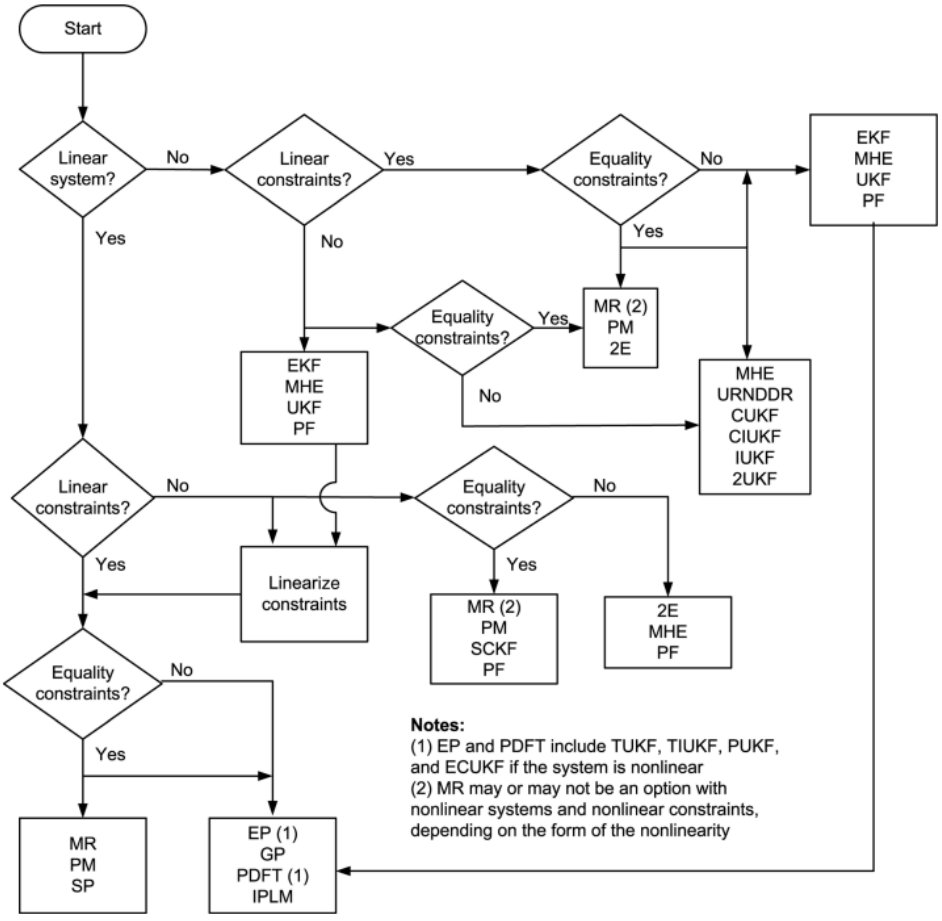

Figure 16: Flowchart to guide the combination selection of system and constraint types usage presented in (SIMON, 2010).

Depending in which step the constraint enters in the KF algorithm, the general interpretation of the problem can differ:

- A linear relationship between states leads to a reduction of state dimension, thus the Model Reduction (MR) approach, although it can also be seen as Perfect Measurements (PM).
- If the constraints are applied directly into the KF formulation, the filter correction phase turns into a constrained likelihood maximization problem or a constrained least squares problem.
- By starting from the unconstrained estimate and then incorporate the constraints, one gets the general projection or the Probability Density Function truncation (PDFT).
- If the state constraints considerably affects the process noise terms, one gets the System projection approach.

When facing nonlinear systems, the constraints have all the possibilities to be inserted in the general solving for nonlinear equations, which increase even more the number of approaches. Intended to facilitate the enunciation of the adopted general formulation, only the used method in this work will be more detailed, the Projected Unscented Kalman Filter (PUKF).

5.4.1 Projected Unscented Kalman Filter (PUKF)

As also described by Teixeira et al. in (TEIXEIRA et al., 2008, 2010) and better detailed in (SIMON, 2006), this filter runs an UKF normally, as already described in 5.3 and then incorporates inequality constrains through the optimization problem:

$$\hat{x}_k^p = \arg\min_{x_k}(x_k - \hat{x}_k)^T W_k^{-1}(x_k - \hat{x}_k), \text{such that: } d_k \leq x_k \leq e_k \tag{5.21}$$

Equation (5.21) gives the usual output x_k from UKF, both d_k and e_k are the constraints as newly added information. Simon and Simon state in Theorem 3 (SIMON; SIMON, 2006) that by setting $W_k = P_k$ the problem will produce the smallest estimation error covariance. Hence, resulting in a quadratic programming problem.

This method was selected due to the number of constraint optimization procedures, being one at most when the generated $\hat{x}_k$ does surpass the barrier limit, while in the Sigma

Point Interval UKF (SIUKF), this number is increased to $2n + 1$ due to the application of the problem into the Sigma Points augmented states (TEIXEIRA et al., 2008). Methods such as the Constrained UKF (CUKF) or Constrained Interval UKF (CIUKF) were not chosen as they transformed the correction phase (5.20) into a Moving Horizon Estimation (MHE) with horizon size of 1, which increases the complexity of the function to optimize; neither the Truncated UKF (TUKF) nor Truncated Interval UKF (TIUKF) due to the complicated equation formulation, as they insert the constraints into the Probability Density Function itself.

5.5 Kalman Filter for parameter estimation

Described in (ISERMANN; MÜNCHHOF, 2011), the KF methodology can also be used for the parameter estimation problem. Isermann and Münchlof define a parameter vector θ with size p, which is then integrated in the original system state vector x, creating an augmented state vector x^a.

$$x^a = \begin{bmatrix} x & \theta \end{bmatrix}^T \tag{5.22}$$

Then, the system in space-state notation can be written as:

$$\begin{aligned} \dot{x}^a(t) = \begin{bmatrix} \dot{x}(t) \\ \dot{\theta}(t) \end{bmatrix} &= \begin{bmatrix} f(x(t), \theta(t), u(t)) \\ 0_{p\times 1} \end{bmatrix} + \begin{bmatrix} G(t)w^d(t) \\ \xi(t) \end{bmatrix} \\ z_k &= h(x(t)) \end{aligned} \tag{5.23}$$

Due to the parameters being modeled as slow-varying dynamics disturbed by a white noise $\xi(t)$, the filter can adjust itself.

PART IV

PROBLEM STATEMENT

6 NUMERICAL EXPERIMENTS SETUP

6.1 *pyDyna* simulator

Based on the mathematical model presented in (TANNURI et al., 2014), *pyDyna* is an API (Application Programming Interface) for interacting with the core of the numerical engine of the TPN-USP (Numerical Offshore Tank) via *Python* language.

Regarding the simulated maneuvering environment, as acquiring data from a real ship is somehow complicated, besides been restricted to the specific registered trajectory in a not so controlled conditions, the *pyDyna* presents as a friendly manner to execute any kind of desired maneuver, along with the possibility to manipulate freely the environmental conditions.

6.2 Estimation problem formulation

The main focus of this work is to retrieve the general hydrodynamic drift coefficients $C_x(\beta), C_y(\beta), C_z(\beta)$ of a vessel during maneuvering. Formulations of these terms obtained from general ship dimensions were intensively studied (OBOKATA, 1987; LEITE et al., 1998; SIMOS et al., 2001), yet they are more focused on moored vessels, which are immobile and more exposed to open sea currents profiles.

Though some previous endeavours to tackle this problem during maneuvers in (UEHARA SASAKI et al., 2021; UEHARA SASAKI; DE MELLO; TANNURI, 2022), the approximation of the surge coefficient component C_x into a single slow varying parameter posed some limitations on the accuracy of the estimation in maneuvers with considerable variation of the drift angle β; notwithstanding, in scenarios with it being constant, the approach displayed the very opposite.

Another observation taken is that although standardized maneuvers such as the evaluated zigzag described in (ITTC, 2002) used in (UEHARA SASAKI et al., 2021; UEHARA

SASAKI; DE MELLO; TANNURI, 2022) lead to relatively accurate estimations, when facing typical maneuvering crafts in most of the time their drift angle is usually utmost 20 degrees. Such characteristic of unexcited inputs can lead to mathematical convergence problems for the KF. Thus, a solution to retrieve them in this context was to approximate them as linear and quadratic terms depending on:

$$\begin{aligned} C_x(\beta) &= C_0^x + X_{\beta\beta}\beta^2 \\ C_y(\beta) &= Y_\beta \beta \\ C_z(\beta) &= N_\beta \beta \end{aligned} \tag{6.1}$$

By inspecting typical curves generated by models proposed by Leite et al. (LEITE et al., 1998) such as shown in Fig.17, it is possible to see that (6.1) captures the general shape of these drift coefficients around zero.

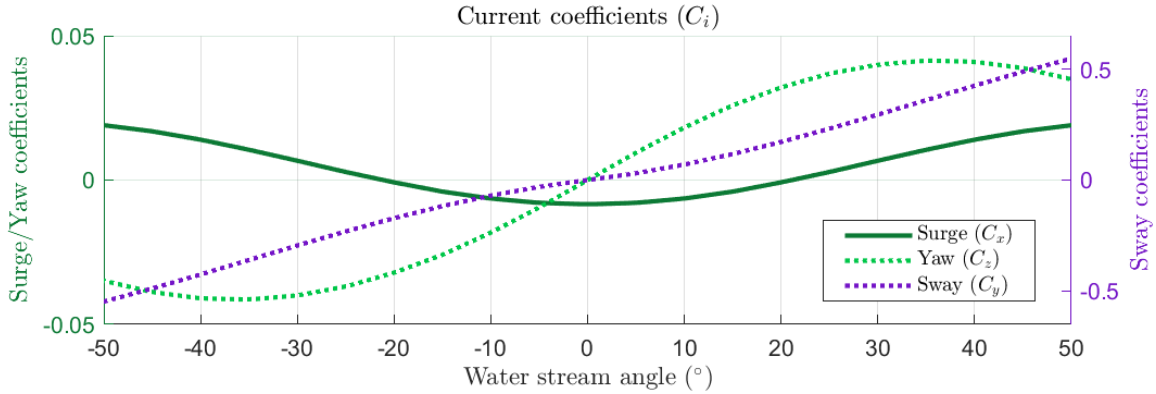

Figure 17: Example of typical drift coefficients generated from a general formulation in (LEITE et al., 1998) (Drift coefficients of the vessel used in the maneuver 7).

Thus, the estimation problem is then divided into two different phases: a called 1P estimator responsible to retrieve the singular term related to ship resistance C_0^x and a 3P estimator, in which the estimates of parameters $X_{\beta\beta}, Y_\beta, N_\beta$ are taken. A flowchart of this separation is described in Fig.18.

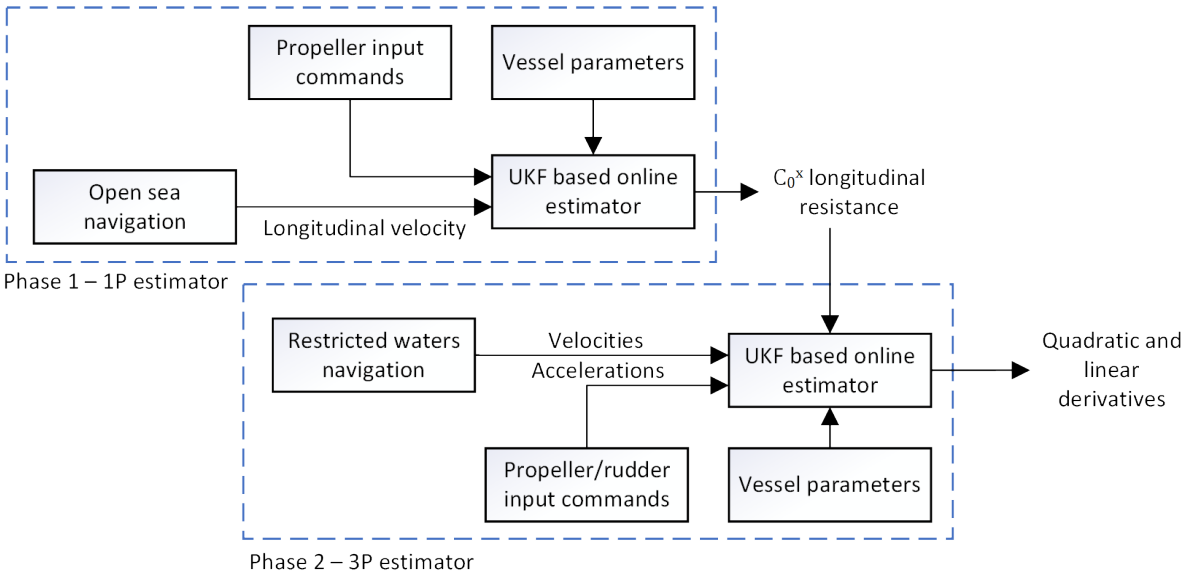

Figure 18: Adopted approach to retrieve the drift coefficients.

6.2.1 1P estimator

This phase should represent the vessel navigating in open seas, thus operating a standard cruise speed profile and mainly without any drift nor any variation of heading. Empirical data in (ŻELAZNY, 2014) reinforces the practicality of this scenario as more than 95 % of the drift angle observed in a route between Western Europe to the East Cost of USA is condensed in a range of less than 2 degrees. Thence, the maneuvering equations can be reduced to merely surge motion, from (4.30) by taking $v = r = 0$:

$$(m - X_{\dot{u}})\dot{u} + \overbrace{\frac{1}{2}\rho LTC_x(\beta = 0)u^2}^{\Gamma_u} = F^{thr}(u, n) \tag{6.2}$$

Instead of treating directly with the estimation of the drift coefficient itself C_x, as the usual parameter estimator approach incur, in order words, assuming it has a slow dynamics $\dot{C}_x = 0$, the 1P estimator had the damping force Γ_u to behave as such, thence, $\dot{\Gamma}_u = 0$. This modification helped to alleviate fluctuations of the estimation of C_0^x, that would appear otherwise due to the non-linearity term $C_x u^2$. The aforementioned approach can only be taken here, in a open sea maneuver, as eventually the forces – including the damping – will stabilize in a certain value.

As such, the state of interest in this case is merely the surge velocity u and the interested "parameter", the surge damping force Γ_u. As the rudder command is irrelevant in this context, only the thruster effective rotation n is used as the system input:

$$\begin{aligned} \underline{x}^{1P} &= \begin{bmatrix} u \end{bmatrix} \underline{\theta}^{1P} = \begin{bmatrix} \Gamma_u \end{bmatrix}, \ \underline{x}^{a_{1P}} = \begin{bmatrix} u & \Gamma_u \end{bmatrix}^T \\ \underline{u}^{1P} &= \begin{bmatrix} n \end{bmatrix} \qquad\qquad\quad \underline{z}^{1P} = \begin{bmatrix} u \end{bmatrix}^T \end{aligned} \tag{6.3}$$

Rewriting (6.3) in the proper system dynamic estimation problem:

$$\begin{aligned} \underline{\dot{x}}^{a_{1P}}(t) &= \begin{bmatrix} \frac{1}{m - X_{\dot{u}}} \left(F^{thr}(u(t), n(t)) - \Gamma_u(t) \right) \\ 0 \end{bmatrix} + w_d^{1P}(t) \\ \underline{z}_k^{1P} &= \begin{bmatrix} 1 & 0 \end{bmatrix} \underline{x}_k^{a_{1P}} + w_n^{1P}(t) \end{aligned} \tag{6.4}$$

At the end, to obtain the surge drift coefficient at zero drift angle C_0^x, one can simply do the inverse operation from (A.9):

$$C_0^x(t) = -\frac{2}{\rho T L u^2(t)} \Gamma_u(t) \tag{6.5}$$

An average value is then taken from $C_0^x(t)$ considering only the last instants, where the estimation is steadier, obtaining the estimate $\hat{C}_0^x$ that will be used onwards.

6.2.2 3P estimator

For the second phase, this should incorporate some maneuvering actions when a vessel is navigating through a strait or channel or even approaching a port, but prior the last part of the berthing procedure, when usually the ship is helped by tugboats. Not considering this latter part is important as the influence of tugboats was not contemplated in the modeling of this work. Another important aspect of the captured data is that it restricted the speed regime above the 2 m/s to avoid heavy influence of the linear damping as mentioned in Fig.12.

As previously mentioned, the interested states in this phase are all the velocities u, v, r and the parameters, the linear and quadratic parameters related to drift coefficients $X_{\beta\beta}, Y_\beta, N_\beta$ plus an additional term of the surge coefficient C_x that will be later explained its redundancy. Both rudder effective rotation n and the rudder effective angle δ are given as system inputs. As surge and sway measurements of accelerations from accelerometers (a_x^{acc}, a_y^{acc}) are taken, additional states for the bias are also used b_x, b_y, while the measurements are inserted in the KF as inputs.

$$\underline{x}^{3P} = \begin{bmatrix} u & v & r & C_x & b_x & b_y \end{bmatrix}^T \; \underline{\theta}^{3P} = \begin{bmatrix} X_{\beta\beta} & Y_\beta & N_\beta \end{bmatrix}^T, \; \underline{x}^{a_{3P}} = \begin{bmatrix} u & v & r & C_x & X_{\beta\beta} & Y_\beta & N_\beta \end{bmatrix}^T$$
$$\underline{u}^{3P} = \begin{bmatrix} n & \delta & a_x^{acc} & a_y^{acc} \end{bmatrix}^T \qquad \underline{z}^{3P} = \begin{bmatrix} u & v & r \end{bmatrix}^T \tag{6.6}$$

Recalling the complete 3 DoF maneuvering equation (4.30) along with (4.36) and (4.43):

$$\begin{bmatrix} m - X_{\dot{u}} & -X_{\dot{v}} & -my_G - X_{\dot{r}} \\ Y_{\dot{u}} & m - Y_{\dot{v}} & mx_G - Y_{\dot{r}} \\ -my_G - N_{\dot{u}} & mx_G - N_{\dot{v}} & I_z - N_{\dot{r}} \end{bmatrix} \begin{pmatrix} \dot{u} \\ \dot{v} \\ \dot{r} \end{pmatrix} + \begin{bmatrix} \Gamma_u(\nu, X_{\beta\beta}) \\ \Gamma_v(\nu, Y_\beta) \\ \Gamma_r(\nu, N_\beta) \end{bmatrix}$$
$$+ \begin{bmatrix} 0 & 0 & -m(x_G r + v) + a_2 \\ 0 & 0 & -m(y_G r - u) - a_1 \\ -I_{yz} r - a_2 & I_{xz} r + a_1 & 0 \end{bmatrix} \begin{pmatrix} u \\ v \\ r \end{pmatrix} = \begin{pmatrix} F^{thr}(u, n) + F_x^{rud}(\nu, \delta) \\ F_y^{rud}(\nu, \delta) \\ M_z^{rud}(\nu, \delta) \end{pmatrix} \tag{6.7}$$

In order to better visualize the formulation of future equations, (6.7) is rewritten as:

$$\begin{pmatrix} \dot{u} \\ \dot{v} \\ \dot{r} \end{pmatrix} = \begin{pmatrix} f_1(\underline{x}^{3P}, \underline{\theta}^{3P}, \underline{u}^{3P}) \\ f_2(\underline{x}^{3P}, \underline{\theta}^{3P}, \underline{u}^{3P}) \\ f_3(\underline{x}^{3P}, \underline{\theta}^{3P}, \underline{u}^{3P}) \end{pmatrix} = M^{-1} \begin{pmatrix} f_u^p(\underline{x}^{a_{3P}}, \underline{u}^{3P}) \\ f_v^p(\underline{x}^{a_{3P}}, \underline{u}^{3P}) \\ f_r^p(\underline{x}^{a_{3P}}, \underline{u}^{3P}) \end{pmatrix} \Rightarrow$$
$$f_u^p(\underline{x}^{a_{3P}}, \underline{u}^{3P}) = F_x^{thr}(u, n) + F_x^{rud}(\underline{x}^{a_{3P}}, \underline{u}^{3P}) - \Gamma_u(\underline{x}^{a_{3P}}) + m(x_G r + v)r - a_2(\underline{x}^{a_{3P}})r$$
$$f_v^p(\underline{x}^{a_{3P}}, \underline{u}^{3P}) = F_y^{rud}(\underline{x}^{a_{3P}}, \underline{u}^{3P}) - \Gamma_v(\underline{x}^{a_{3P}}) + m(y_G r - u)r + a_1(\underline{x}^{a_{3P}})r$$
$$f_r^p(\underline{x}^{a_{3P}}, \underline{u}^{3P}) = M_z^{rud}(\underline{x}^{a_{3P}}, \underline{u}^{3P}) - \Gamma_r(\underline{x}^{a_{3P}}) + (I_{yz} r + a_2(\underline{x}^{a_{3P}}))u - (I_{xz} r + a_1(\underline{x}^{a_{3P}}))v \tag{6.8}$$

The damping forces and moment Γ_i's were comprised to better visualize (6.8). The whole expansion can be seen in A.1.1 for surge force Γ_u, in A.1.2 for sway force Γ_v and in A.1.3 for yaw moment Γ_r.

Both acceleration terms in surge $\dot{u}$ and sway $\dot{v}$ directions can be written as the value given by the accelerometer measurements a_i^{acc} added by a white noisy bias that slow vary b_i:

$$\begin{aligned} \dot{u} &= a_x^{acc} + b_x \\ \dot{v} &= a_y^{acc} + b_y \end{aligned} \tag{6.9}$$

With:

$$\begin{aligned} \dot{b}_x &= f_5 = 0 \\ \dot{b}_y &= f_6 = 0 \end{aligned} \tag{6.10}$$

The surge drift coefficient as a whole is used as a state in the dynamics to enable the insertion of the information $\hat{C}_0^x$ obtained in the previous phase and its derivate in time calculation is shown in Appendix A.2:

$$\dot{C}_x = 2X_{\beta\beta}\beta\frac{u\dot{v} - v\dot{u}}{u^2 + v^2} \tag{6.11}$$

And by adding the data from accelerometers in (6.9):

$$\dot{C}_x = f_4(\underline{x}^{a_{3P}}, \underline{u}^{3P}) = 2X_{\beta\beta}\beta\frac{u(a_y^{acc} + b_y) - v(a_x^{acc} + b_x)}{u^2 + v^2} \tag{6.12}$$

The parameters, whose influence in the maneuver dynamics appear in the damping forces Γ_i's, are assumed as having a slow varying dynamics, thus:

$$\begin{aligned} \dot{X}_{\beta\beta} &= 0 \\ \dot{Y}_{\beta} &= 0 \\ \dot{N}_{\beta} &= 0 \end{aligned} \tag{6.13}$$

Merging equations (6.8), (6.12), (6.10) and (6.13), the first portion of the KF is then written as:

$$\dot{\underline{x}}^{a_{3P}}(\underline{x}^{a_{3P}}(t), \underline{u}^{3P}(t)) = \begin{pmatrix} f_1 \\ \vdots \\ f_6 \\ 0_{3\times 1} \end{pmatrix} (\underline{x}^{a_{3P}}(t), \underline{u}^{3P}(t)) + w_d^{3P}(t) \tag{6.14}$$

As the three velocities are taken as measurements, the second portion of the KF can be written as:

$$h(\underline{x}_k^{a_{3P}}, \underline{u}_k^{3P}) = \begin{pmatrix} u \\ v \\ r \end{pmatrix} + w_n^{3P}(t_k) \tag{6.15}$$

Including the estimation of the surge coefficient obtained from the phase one 6.2.1 along with the knowledge of the curves general tendency as restrictions (5.21) for the problem:

$$\begin{aligned} C_x &= C_0^x + X_{\beta\beta}\beta^2 \\ X_{\beta\beta} &> 0 \end{aligned} \tag{6.16}$$

Finally, combining (6.14), (6.16) and (6.16):

$$\begin{aligned} \dot{\underline{x}}^{a_{3P}}(\underline{x}^{a_{3P}}(t), \underline{u}^{3P}(t)) &= \begin{pmatrix} f_1 \\ \vdots \\ f_6 \\ 0_{3\times 1} \end{pmatrix} (\underline{x}^{a_{3P}}(t), \underline{u}^{3P}(t)) + w_d^{3P}(t) \\ \underline{z}_k(\underline{x}_k^{a_{3P}}, \underline{u}_k^{3P}) &= \begin{pmatrix} u \\ v \\ r \end{pmatrix} + w_n^{3P}(t_k) \end{aligned} \quad , \quad \text{with: } \begin{matrix} X_{\beta\beta} > 0 \\ C_x = C_0^x + X_{\beta\beta}\beta^2 \end{matrix} \tag{6.17}$$

6.3 Proposed simulated maneuvers

For the maneuvers in open seas, the idea was to simply put a vessel at Full Sea Speed command, which represents 100% of thrust capacity, and maintaining its navigation in a straight line by leaving the rudder at midships. Although it would be infeasible in real life, due to various limitations for continuous operating time, this could represent the optimal condition for the estimator to retrieve better estimates, as the linear damping becomes even less significant (Fig.12). Environmental conditions were set as zero, which restrained the problem to a mere 1 DoF.

As for the 3P estimator, two maneuvers were selected: one was a standard zigzag maneuver described in (ITTC, 2002) in a calm water scenario; and the other was a maneuver executed by pilots in real-time maneuvering simulations, conducted at TPN-USP

under real conditions and environmental conditions, in different ports in Brazil (TANNURI; MARTINS, 2018).

6.4 Simulated vessels

To evaluate the robustness of the proposed method, different types of vessels were tested. The presented ones, shown in Tab.1, were selected accordingly to the availability of recorded data trials in the TPN-USP database.

Table 1: List of vessels used in this study.

Vessel	Vessel category	General dimensions
0	Bulk carrier	LOA 259 m Beam 43 m Draft 11.5 m
1	Bulk carrier	LOA 300 m Beam 50 m Draft 17.8 m
2	Tanker (Suezmax)	LOA 278.5 m Beam 48 m Draft 17.2 m
3	Tanker (Suezmax)	LOA 278.5 m Beam 48 m Draft 17.2 m
4	Container ship	LOA 244 m Beam 32.2 m Draft 12.5 m
5	Container ship	LOA 300 m Beam 48 m Draft 13.7 m
6	Container ship	LOA 300 m Beam 50 m Draft 17.8 m
7	Container ship	LOA 335 m Beam 51 m Draft 13.8 m
8	Container ship	LOA 366 m Beam 51 m Draft 12.8 m
9	Container ship	LOA 368 m Beam 51 m Draft 14.8 m

More details of these ships can be found in Appendix B.1. Apart from some container ships, all of them were equipped with a single screw fixed propeller and a single rudder as the solely system responsible to generate forces and moments in the vessel to move it through the water. The mentioned exceptions have an additional bow thruster propeller, yet it could be neglected as they are not used in high speeds – which is the current evaluated navigation context – due to being extremely ineffective. Thus, allowing the modeling presented in 4.3.1 and 4.3.2 to well represent their real dynamics.

6.5 Estimator setup values

Aiming to represent a more realist scenario, as the *pyDyna* gives directly the real simulated values, a white noise was added to the outputted velocity and acceleration data to emulate the response of actual sensors. Values for these noise were loosely taken from the VN series Inertial Measurement Unit (IMU) product from Vectornav (VECTORNAV, n.d.).

$$\begin{gathered} r_1^{1P} = r_1^{3P} = r_2^{3P} = 2.5 \times 10^{-4},\ r_3^{3P} = 7.62 \times 10^{-7} \\ b_x = b_y = 1 \times 10^{-12} \end{gathered} \tag{6.18}$$

The velocities terms are r_1^{1P}, r_1^{3P} and r_2^{3P}, which represent the velocities in surge and sway, respectively. The rotation in yaw, r_3^{3P} and the acceleration bias by b_x and b_y.

Regarding the 1P estimator phase, the disturbance matrix Q^{1P} for the KF was empirically set as:

$$q_1^{1P} = 5 \times 10^{-1},\ q_2^{1P} = 1 \times 10^{4},\ \Rightarrow Q^{1P} = \begin{bmatrix} q_1^{1P} & 0 \\ 0 & q_2^{1P} \end{bmatrix} \tag{6.19}$$

As for the 3P estimator, the matrix Q^{3P} was defined as:

$$\begin{gathered} q_1^{3P} = q_2^{3P} = 5 \times 10^{-1},\ q_3^{3P} = 3.04 \times 10^{-6} \\ q_4^{3P} = 1 \times 10^{-6} \\ q_5^{3P} = q_6^{3P} = 1 \times 10^{-12},\ q_7^{3P} = 7.62 \times 10^{-11} \\ q_8^{3P} = q_9^{3} = 1 \times 10^{-12} \end{gathered} \Rightarrow Q^{3P} = \begin{bmatrix} q_1^{3P} & 0 & \dots & 0 \\ 0 & q_2^{3P} & \dots & 0 \\ \vdots & \vdots & \ddots & \vdots \\ 0 & 0 & \dots & q_9^{3P} \end{bmatrix} \tag{6.20}$$

Such initialized values can also be interpreted as being a trade-off between the utilized model with the received measurements data when the latter is available. If the correspondent value of q_i for a specific state is lesser than r_i, the final estimation of $\hat{x}_i$ will tend to follow the modeled dynamics; otherwise, $\hat{x}_i$ will be more adherent with the measurements.

Recalling that the first states q_1^{1P}, q_{1-3}^{3P} refer to the velocities, which are measured through sensors; by setting higher values than their measured counterpart r^{1P}, r_{1-3}^{3P}, the measurements of velocities will have more importance than the system dynamics.

In states that are not measured, as for the surge damping force q_2^{1P} or for the parameters q_{5-7}^{3P}, their values are set in an expectancy that the respective estimate standard variation will not surpass such values. Thence, the value for q_2^{1P} is in force magnitude order, while q_{5-7}^{3P} are in their respective parameters magnitude order.

The accelerometer bias are the own states q_8^{3P} and q_9^{3P} and the errors for the surge coefficient q_4^{3P} were chosen to capture the errors in the estimation in surge equation.

Parameters such as the ones in the UKF setup were assumed as their usually assigned values (WAN; VAN DER MERWE, 2000): $\alpha = 1 \times 10^{-3}, \kappa_i = 0$ and $\beta = 2$, for the optimal

value for Gaussian distributions.

7 RESULTS

As there are many different vessels and maneuvers which were used in this study, intending to not pollute the work with various images, the results were compiled into tables; while the procedure as a whole is shown only for a single vessel in particular.

7.1 Results obtained from maneuver number 7

This vessel was randomly chosen to be a showcase for the entire proposed procedure, which can be recalled through Fig.18. The first phase is shown in 7.1.1, while the second in 7.1.2 for a zigzag maneuver and for a port maneuver executed by real pilots in 7.1.3. More details about these can be found in Appendix B.2.

Both open sea and zigzag maneuvers were manually set to run through *pyDyna* with a fixed time step of 0.1 second, with a total simulation time of 10,000 seconds. The measurement frequency was 5 times slower, or in other words, with a period of 0.5 seconds between each measured sample. As for the real maneuvers, they were only slightly changed to not consider parts where the tugboats influenced its behaviour, as it is not considered in the adopted model of this work.

7.1.1 Open sea navigation

All the open sea maneuvers started with 5 m/s without any rotation or lateral speed. The rudder is maintained on midship. The only command given is the engine full ahead (acceleration up until the maximum rotation) as shown in Fig.19.

The line in red represents the estimation output given directly by the UKF approach and the green line the supposedly real value given from *pyDyna* output. In Fig.20, as expected since the measurements are taken, the estimate follows well the green line counterpart.

As for the estimation of the surge coefficient C_0^x, Fig.21 shows the estimated coefficient

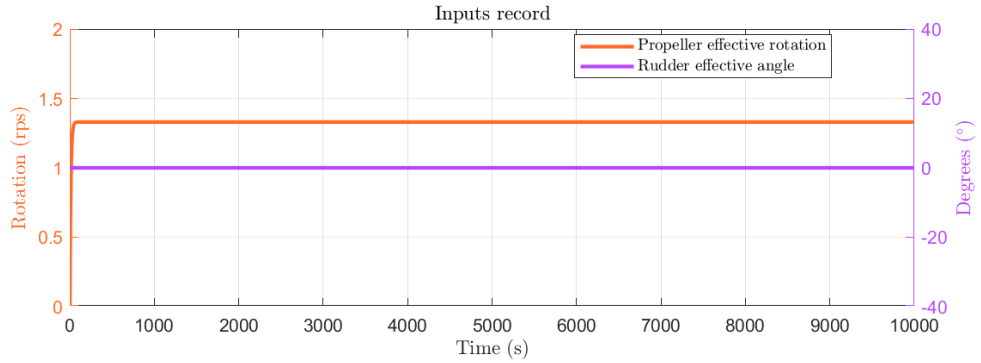

Figure 19: List of commands given in the open sea maneuver.

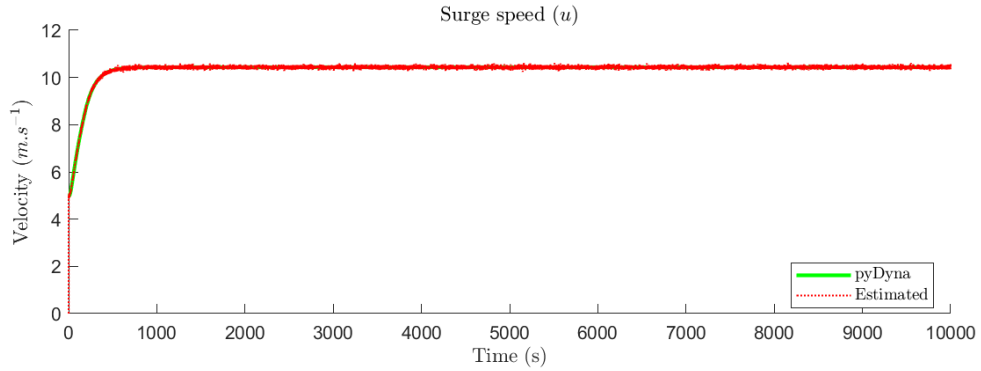

Figure 20: Estimated surge speed in contrast to the *pyDyna* in the open sea maneuver.

during the maneuver. An average value (shown in magenta) is taken considering only the estimates obtained after the 8000 seconds mark (shown by the dotted red line), time arbitrarily chosen as the estimate better stabilized.

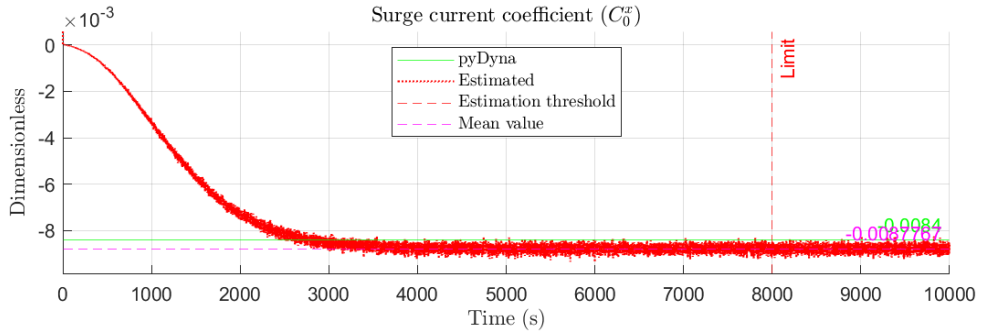

Figure 21: Estimated surge coefficient C_0^x in contrast to the real value from *pyDyna* in the open sea maneuver.

From Fig.22 one can better quantify how the disparity of the drift coefficient estimation impacts on the system, as forces data give more tangible notions for readability.

Another form to evaluate the obtained estimate is through the error analysis, as shown in Fig.23, with both absolute and percentage errors being shown.

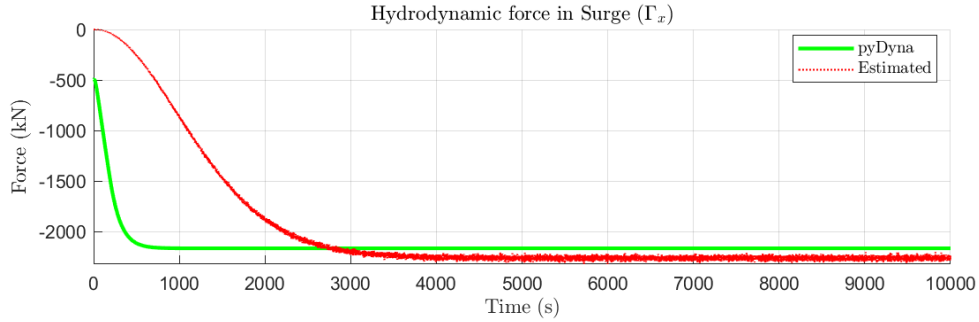

Figure 22: Estimated hydrodynamic force in surge in contrast to the *pyDyna* in the open sea maneuver.

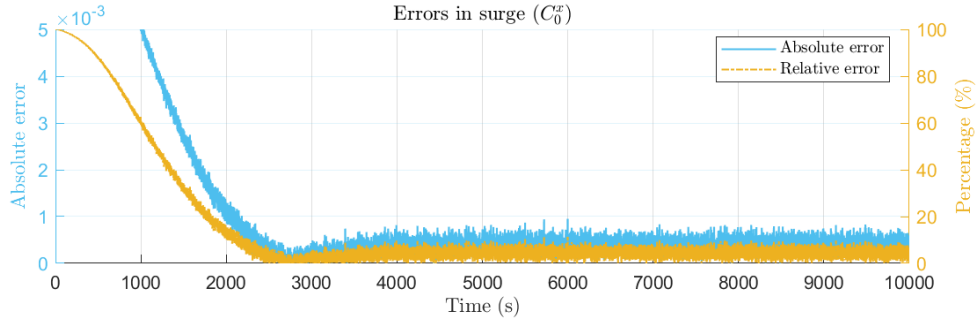

Figure 23: Comparison of absolute and percentage errors in the surge drift coefficient in the open sea maneuver.

7.1.2 Zigzag maneuver

As described in (ITTC, 2002), the maneuver is obtained by reversing the rudder alternately by 10, 20 or 30 degrees to either side at a deviation of 10, 20 or 30 degrees from the initial heading. After a steady approach, the rudder is put over to starboard (first execute). When the heading is 10, 20 or 30 degrees off the initial value, the rudder is reversed to the same angle to port (second execute). The first number following the name refers to the heading deviation, while the second, the rudder angle.

All the simulated maneuvers were standardized to zigzag 10/30, whose list of commands can be seen in Fig.24 and which would produce the highest values for drift angles in a calm water scenario. Fig.25 shows that the drift angle almost reach 20 degrees.

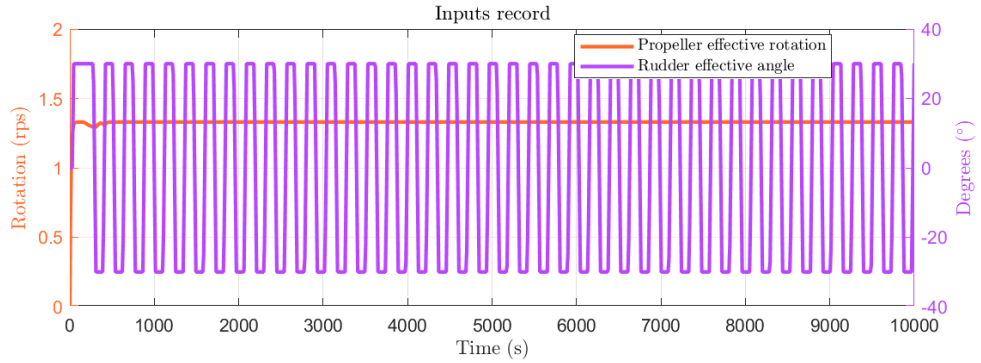

Figure 24: List of commands given in the simulated zigzag 10/30 maneuver.

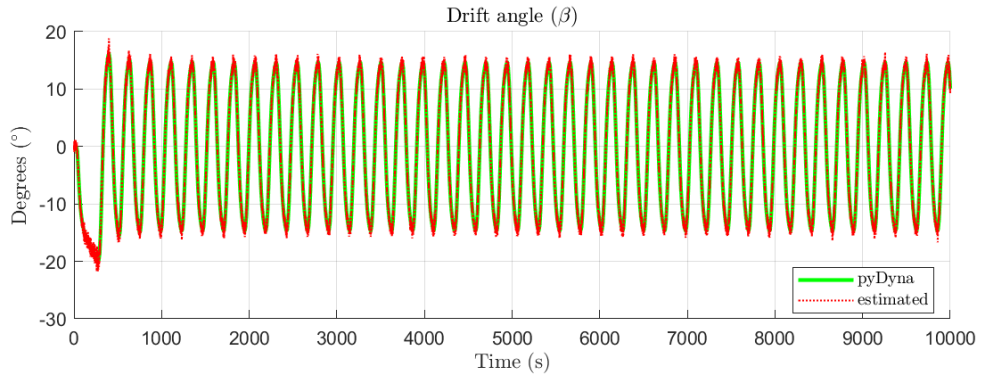

Figure 25: Estimated drift angle in the simulated zigzag 10/30 maneuver.

Analogous to Fig.20, the estimated velocities in surge, sway and yaw (Fig.26) were well accurate as expected from measured states.

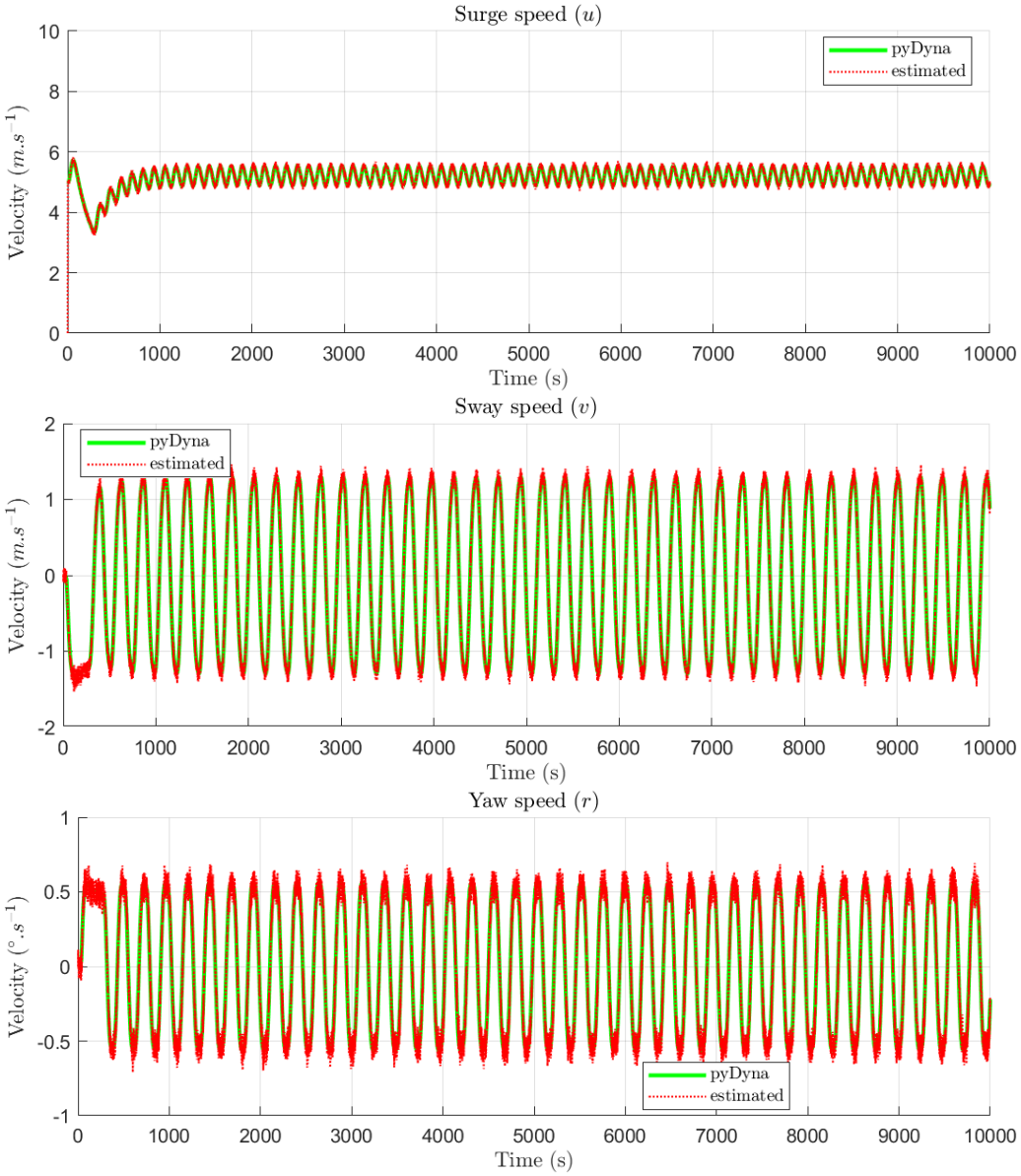

Figure 26: Estimated velocities (u, v, r) in the simulated zigzag 10/30 maneuver.

One form to evaluate how the proposed model for the propeller 4.3.1 and rudder 4.3.2 performed was to plot the forces and moment obtained from the estimated states in Fig.26 with the *pyDyna* output as shown in Fig.27. Note that these forces and moment are then used as an input for the KF system dynamics.

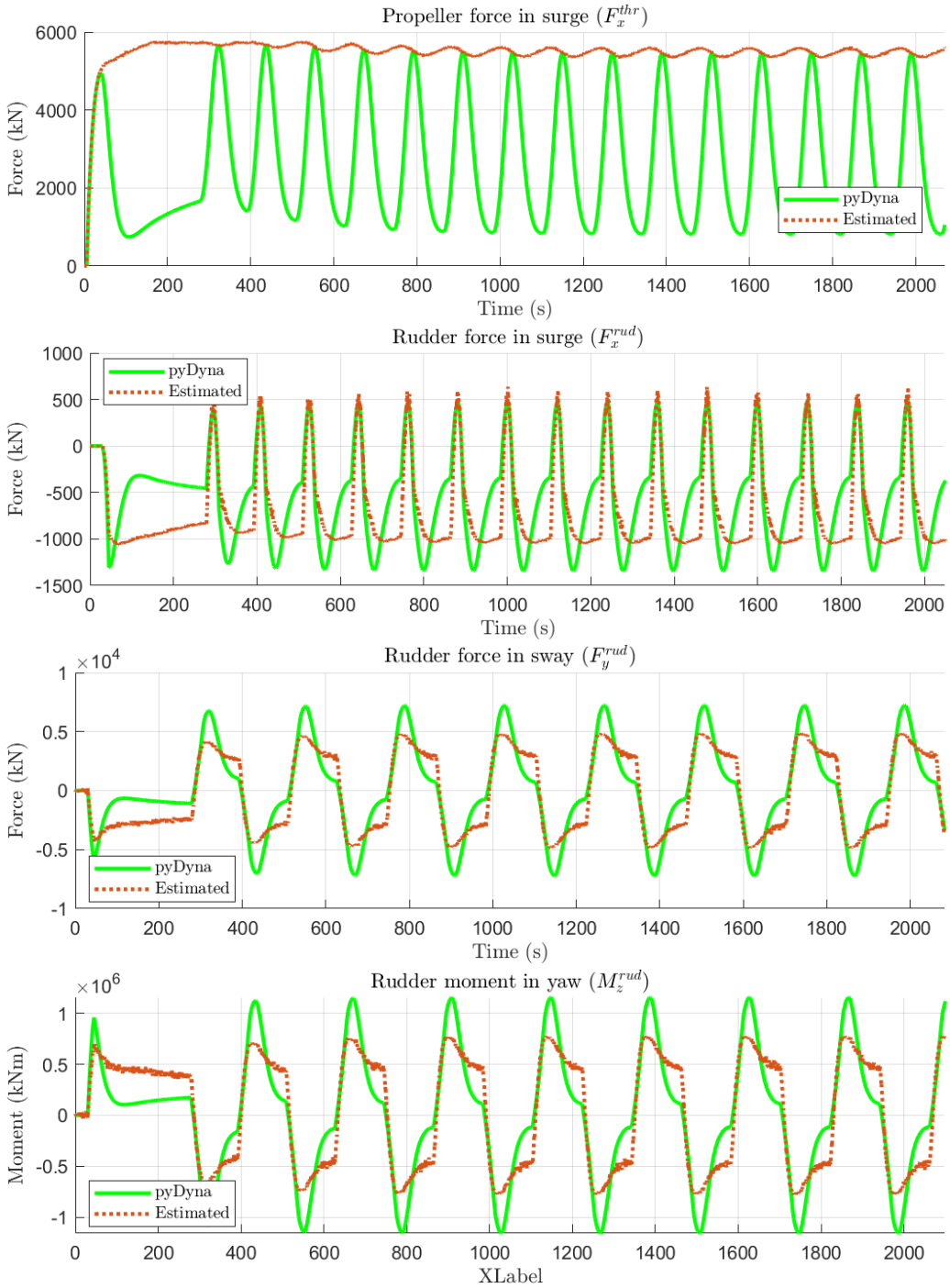

Figure 27: Estimated forces and moment generated by the propeller and rudder in the simulated zigzag 10/30 maneuver.

For the zigzag 10/30, the proposed model suffered to capture the rapid variation of the propeller force in surge, which certainly influenced such error towards the rudder components. Nonetheless, the peak value for the former reached the *pyDyna* counterpart and the rudder parcels more or less could follow the *pyDyna* behaviour.

As for the 3P estimator, the parameters are now the three drift coefficients $X_{\beta\beta}, Y_{\beta}, N_{\beta}$,

whose estimates are shown in Fig.28. The red line represents the direct output retrieved from the KF method, while the green and purple lines were plot to show what would be the expected value of the respective parameter at the specified drift range, as shown in the graph legend.

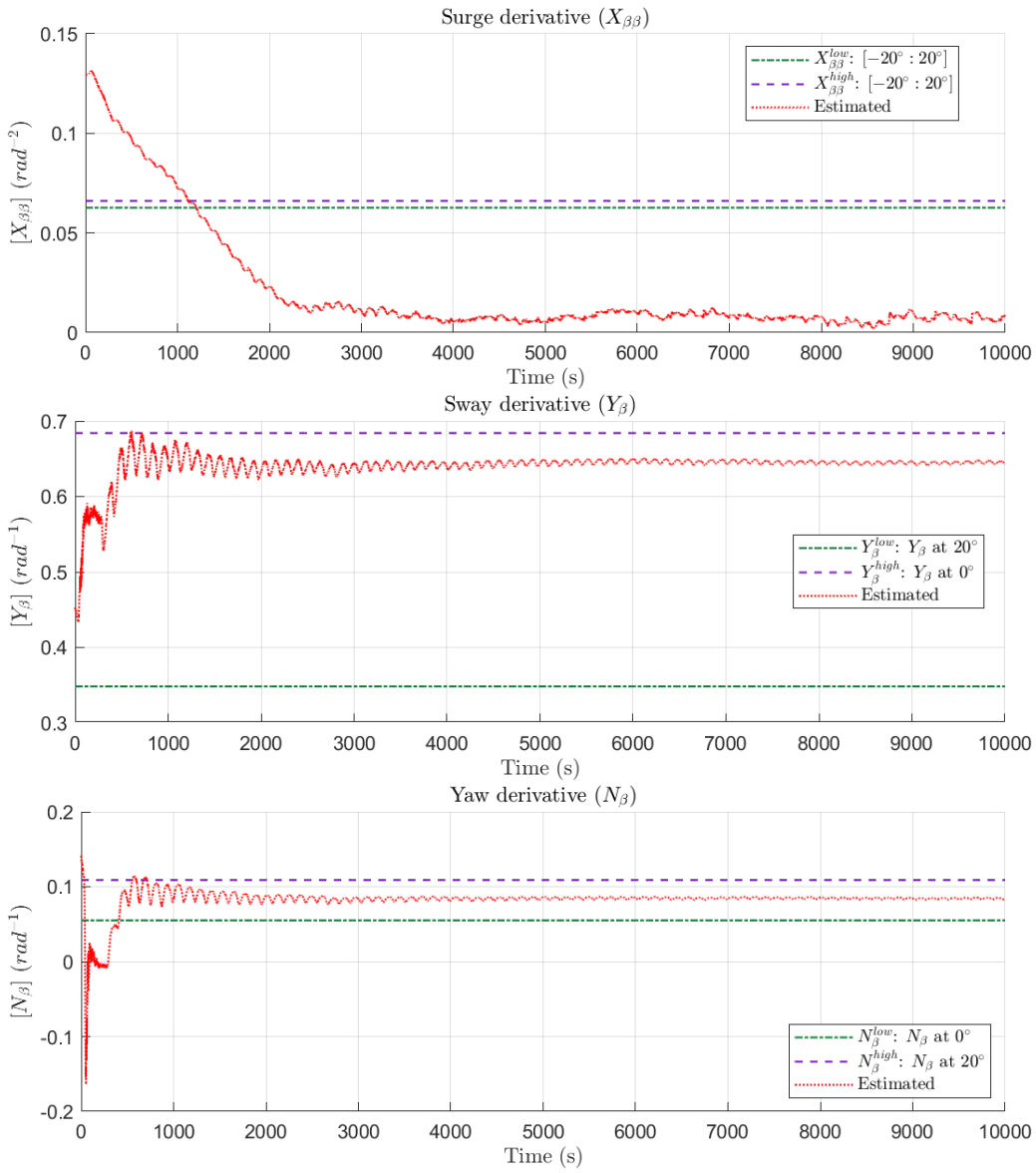

Figure 28: Estimated parameters $(X_{\beta\beta}, Y_\beta, N_\beta)$ in the simulated zigzag 10/30 maneuver.

Yet, as they are not so direct to interpret, through applying these obtained values in (6.1) (remembering that C_0^x is retrieved from the 1P estimator in 7.1.1), the drift coefficients can be obtained, which are easier to compare with the actual counterpart, as shown in Fig.29 by plotting in the time domain.

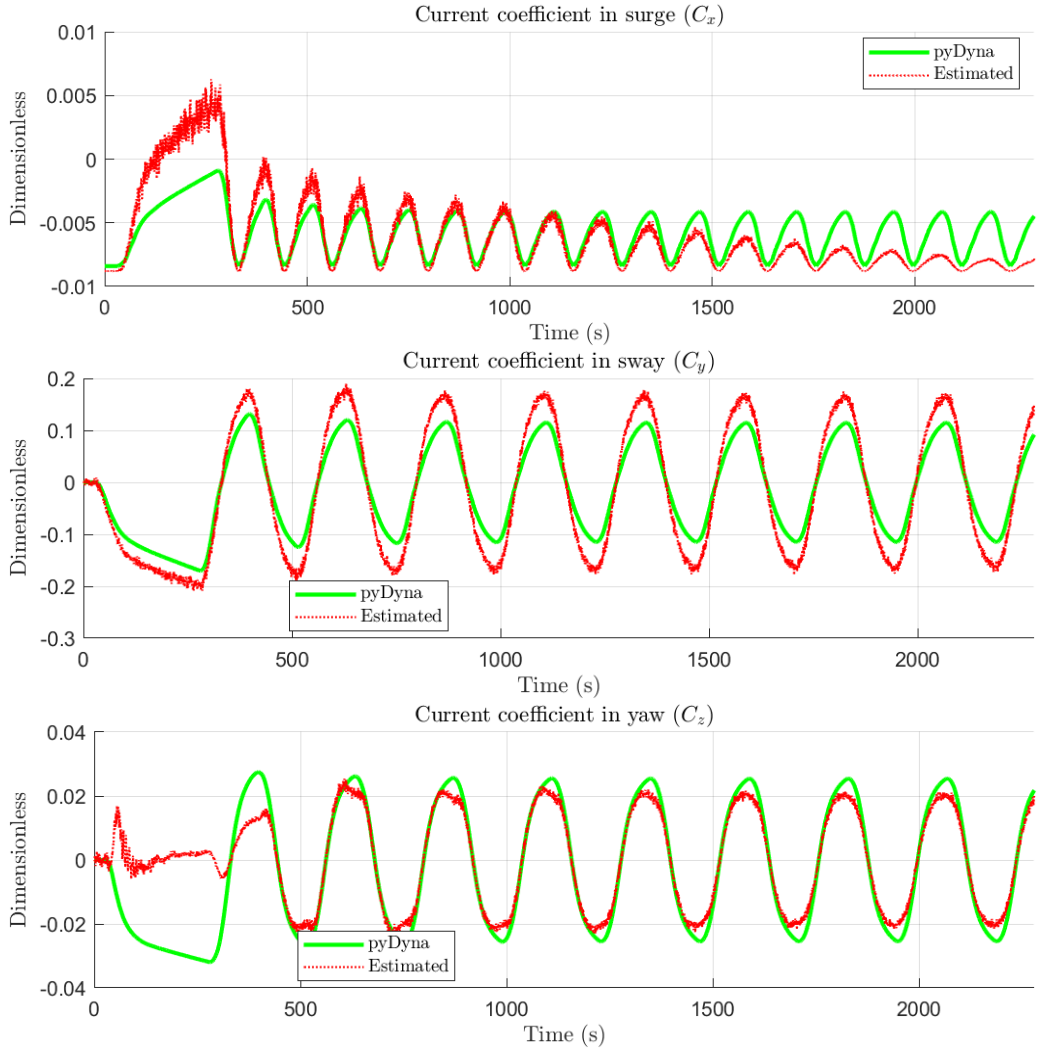

Figure 29: Estimated drift $C_x(t), C_y(t), C_z(t)$ in the simulated zigzag 10/30 maneuver plotted in time domain.

Fig.30 presents another manner to grasp a better feeling regarding the estimations from Fig.28. By taking only the final parcel of the parameters (last 20 % of the estimation analogously to the 1P phase in Fig.21), the average values can be taken and by plugging again in (6.1), allowing the plot of the drift coefficients for a more broad range of drift angles as shown in Fig.30.

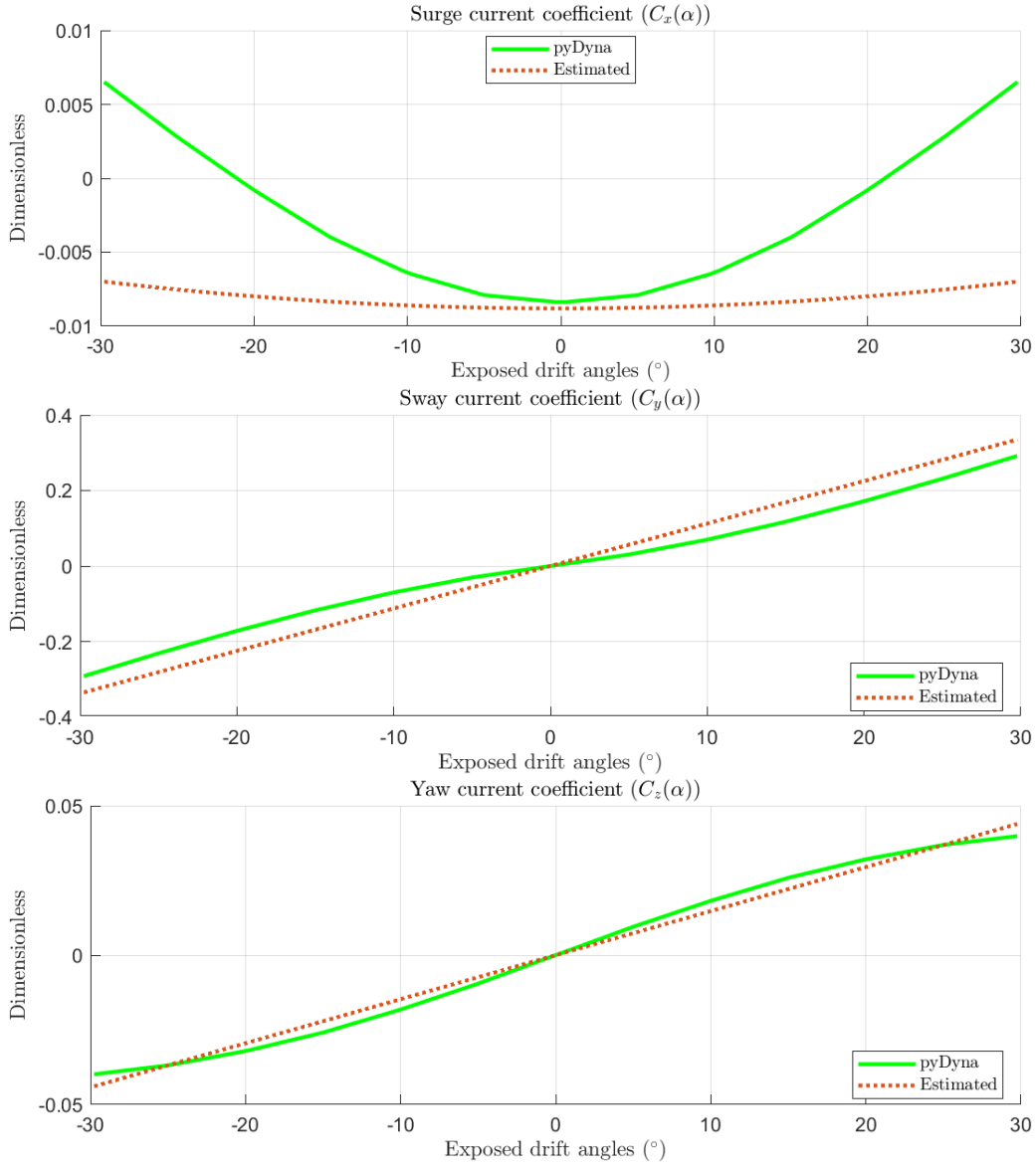

Figure 30: Estimated coefficients $C_x(\beta), C_y(\beta), C_z(\beta)$ in the simulated zigzag 10/30 maneuver plotted for generic drift angles.

7.1.3 Simulated maneuver

For this particular maneuver number 7, the simulated maneuver consisted in a container ship entrance into its terminal in Guanabara Bay, Rio de Janeiro, Brazil. The major environmental conditions affecting the maneuver were the wind, coming from a Southeast direction with an average speed of 15 knots; and the current, going to Northwest with the highest registered intensity in the trajectory being 0.2 knots and further decreasing as the vessel approached a sheltered area. Fig.31 illustrates the recorded trajectory.

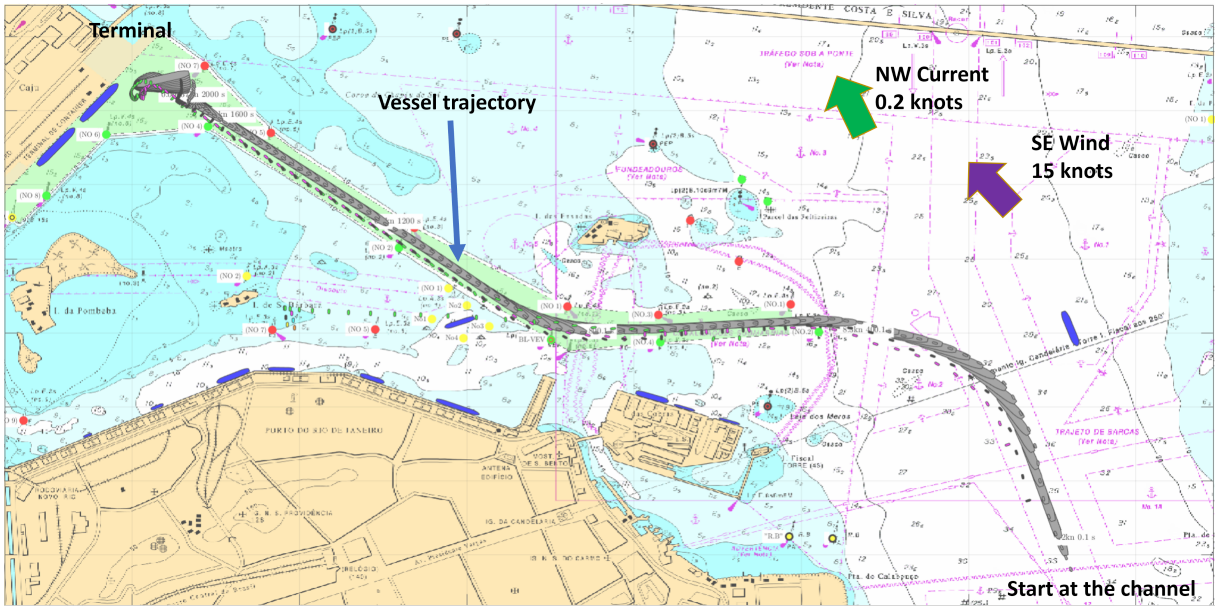

Figure 31: Visual description of a simulated maneuver in Guanabara Bay.

As should be expected from a real person in charge of controlling the ship navigation, the rudder and propeller orders (Fig.32 are not so uniform as the previous shown in Fig.19 and Fig.24).

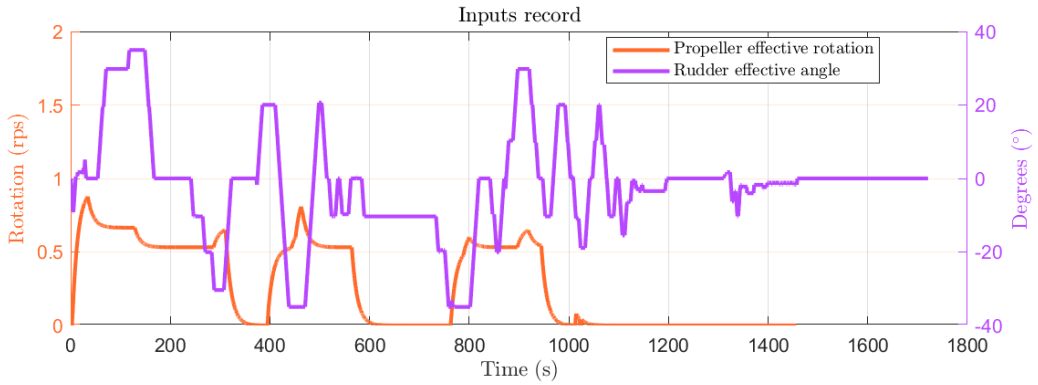

Figure 32: List of commands given in the simulated maneuver in Guanabara Bay.

The drift angle reaches almost -20° as shown in Fig.33.

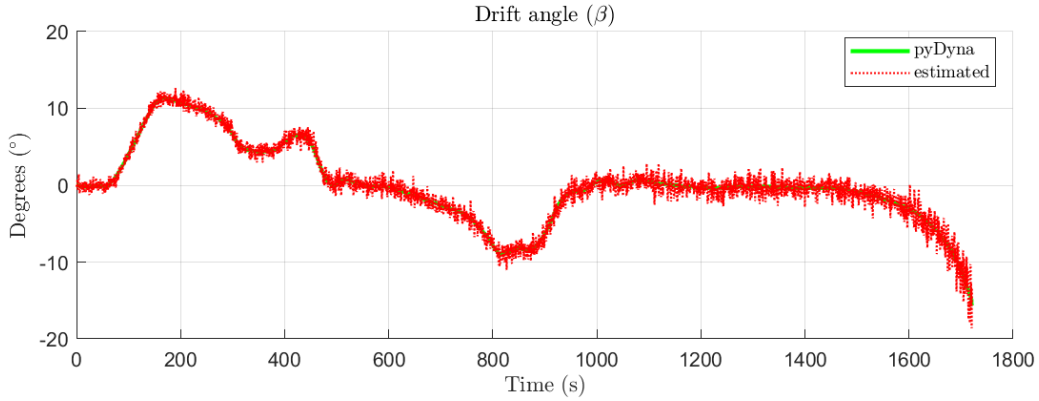

Figure 33: Estimated drift angle in the simulated maneuver in Guanabara Bay.

The estimated velocities are shown in Fig.34 and are equally accurate as in the previous tests (Fig.20 and Fig.26).

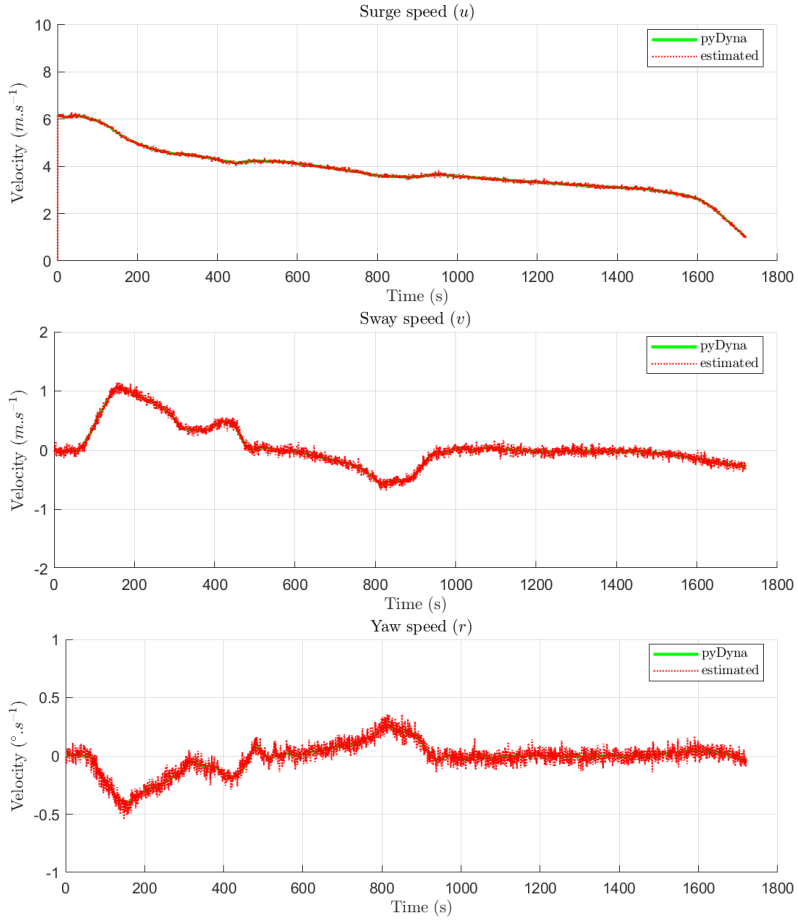

Figure 34: Estimated velocities (u, v, r) from the simulated maneuver in Guanabara Bay.

With the same purpose to evaluate the forces and moment model that are inputted in the KF as in Fig.27, these estimates are shown in Fig.35 now for the simulated maneuver. If in the zigzag 10/30 maneuver the model could not represent the quick variation appeared

in the *pyDyna* propeller force, here the model could almost match the *pyDyna* component. In the final moments of the simulated maneuver, the propeller operated with the engine going astern, envisioning to brake the ship. As such model was indeed not contemplated in 4.3.1, evidently the estimation would nullify.

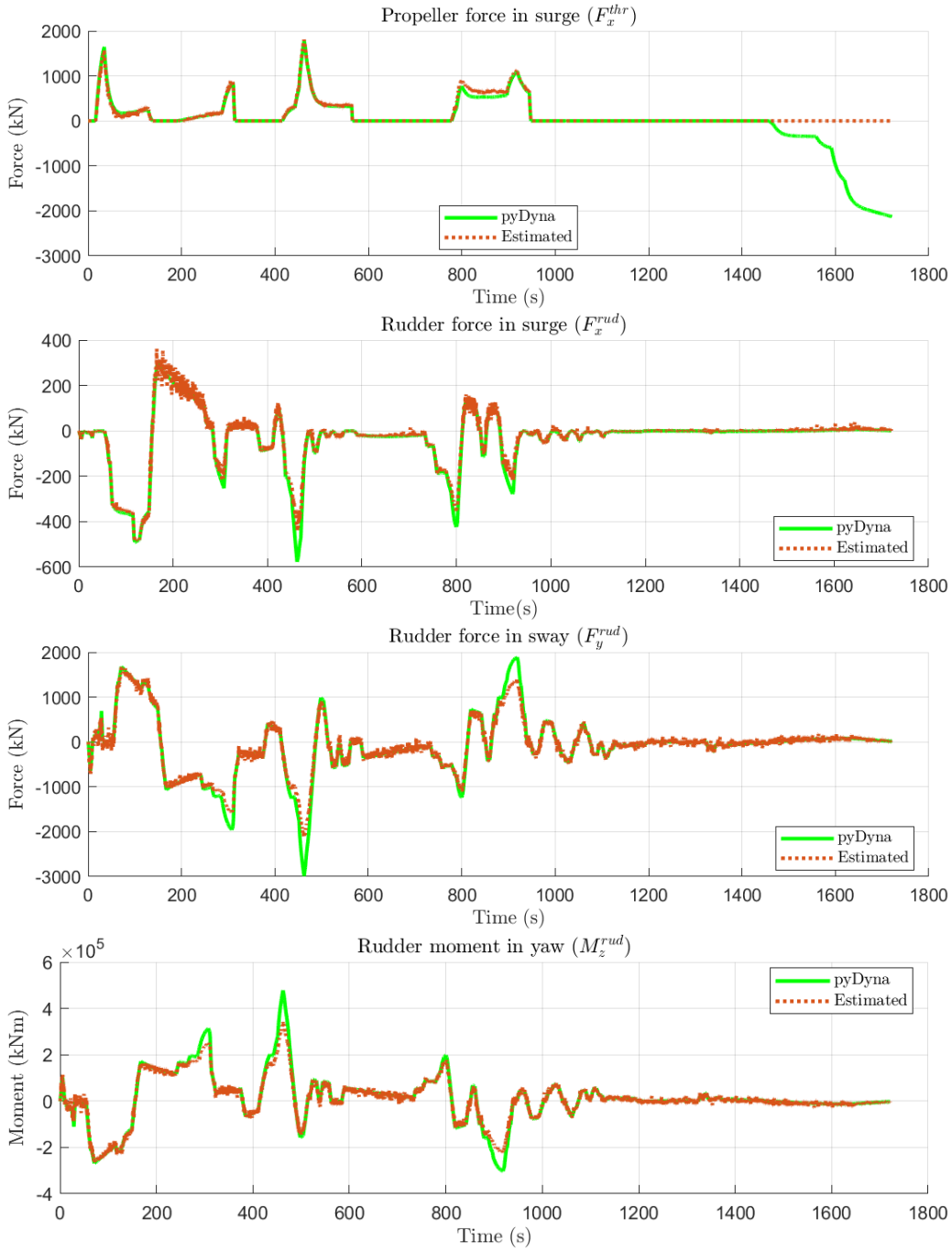

Figure 35: Estimated forces and moment generated by the propeller and rudder in the simulated maneuver in Guanabara Bay.

As the estimated propeller force became better, the rudder model could be analyzed more independently and by inspecting the forces and moments in Fig.35, the estimates

were much more adherent here in contrast to the zigzag maneuver, even though some discrepancies can be better seen in peak values.

From the direct UKF output, the parameter estimates are shown in Fig.36. Unexpectedly, the unmodelled environmental agents lead to the heavily impact in these estimates, with the filter not even reaching a stable value at the end and further distancing from the supposedly real values (purple and green lines).

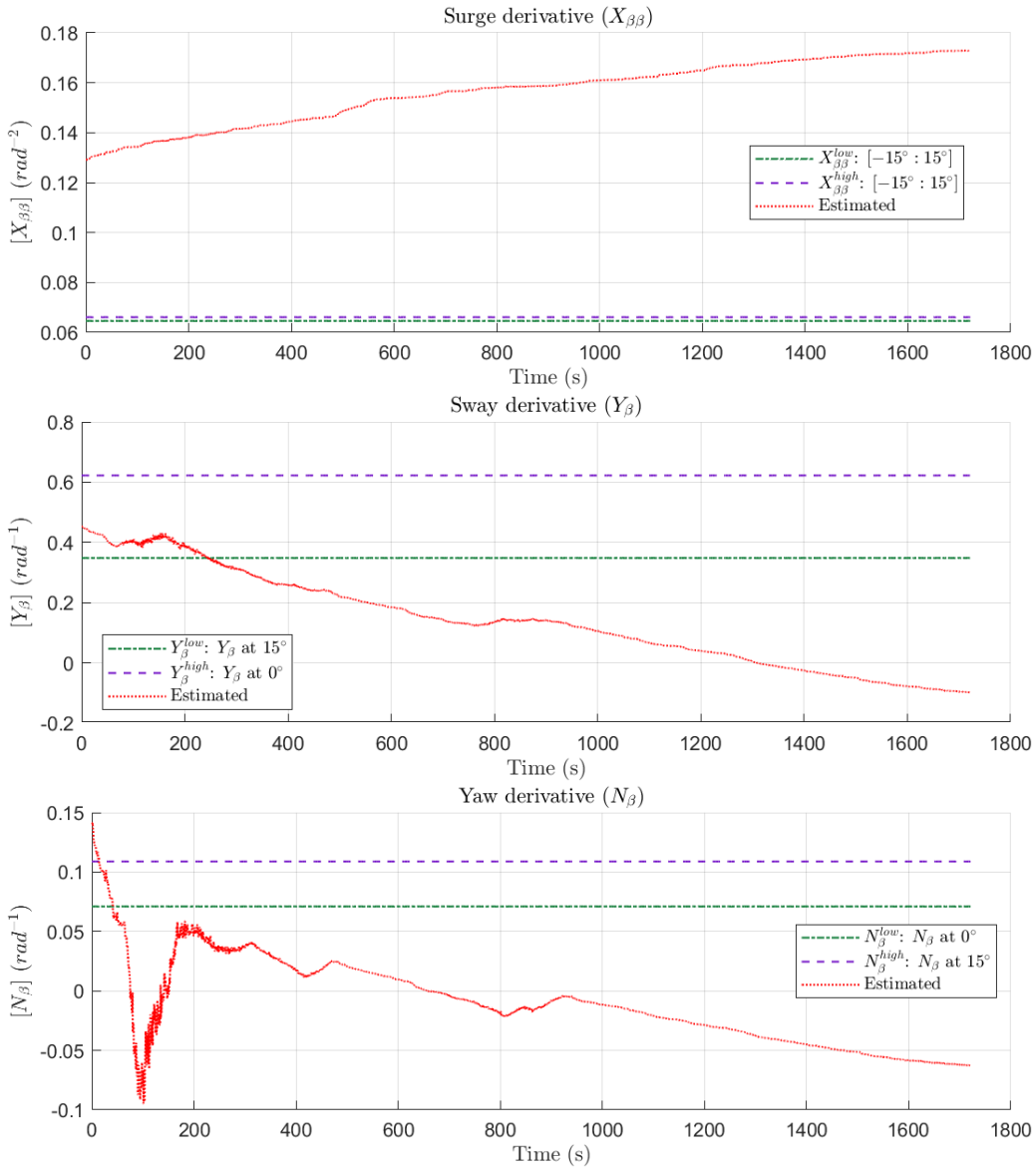

Figure 36: Estimated parameters ($X_{\beta\beta}, Y_\beta, N_\beta$) in the simulated maneuver in Guanabara Bay.

Again, applying these values in (6.1), the estimated drift coefficients during maneuver time can be retrieved in Fig.37. Both surge and sway coefficient estimates behaved similarly to the *pyDyna* counterpart, however the error for the former became more ap-

parently in the peaks while for the latter the estimate decoupled even more as the time step increased. The moment estimate could barely establish a resemblance to the *pyDyna* value.

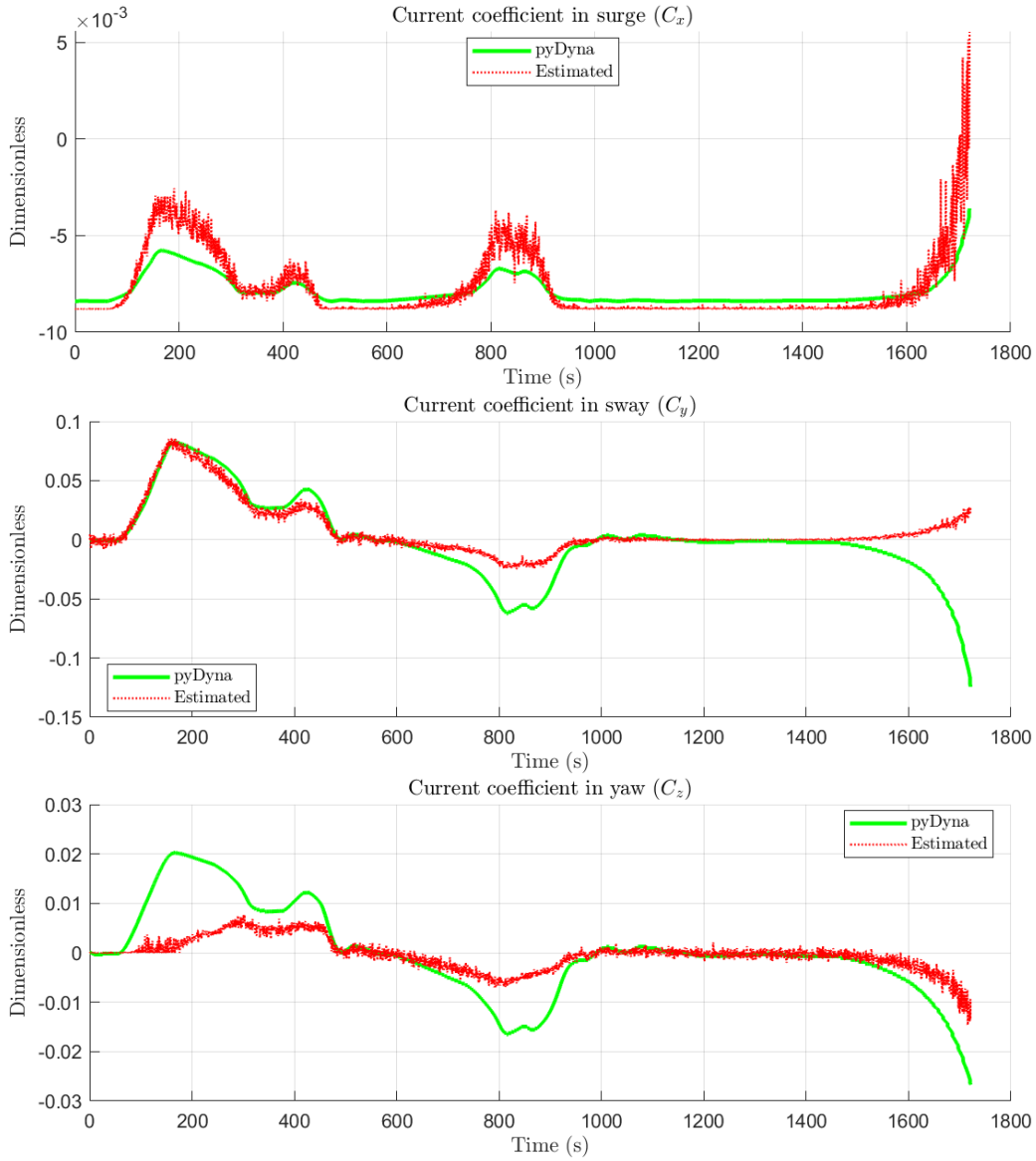

Figure 37: Estimated coefficients $C_x(t), C_y(t), C_z(t)$ in the simulated maneuver in Guanabara Bay plotted in time domain.

By capturing only the average values at the end portion, a more general interpolation can be obtained as shown in Fig.38.

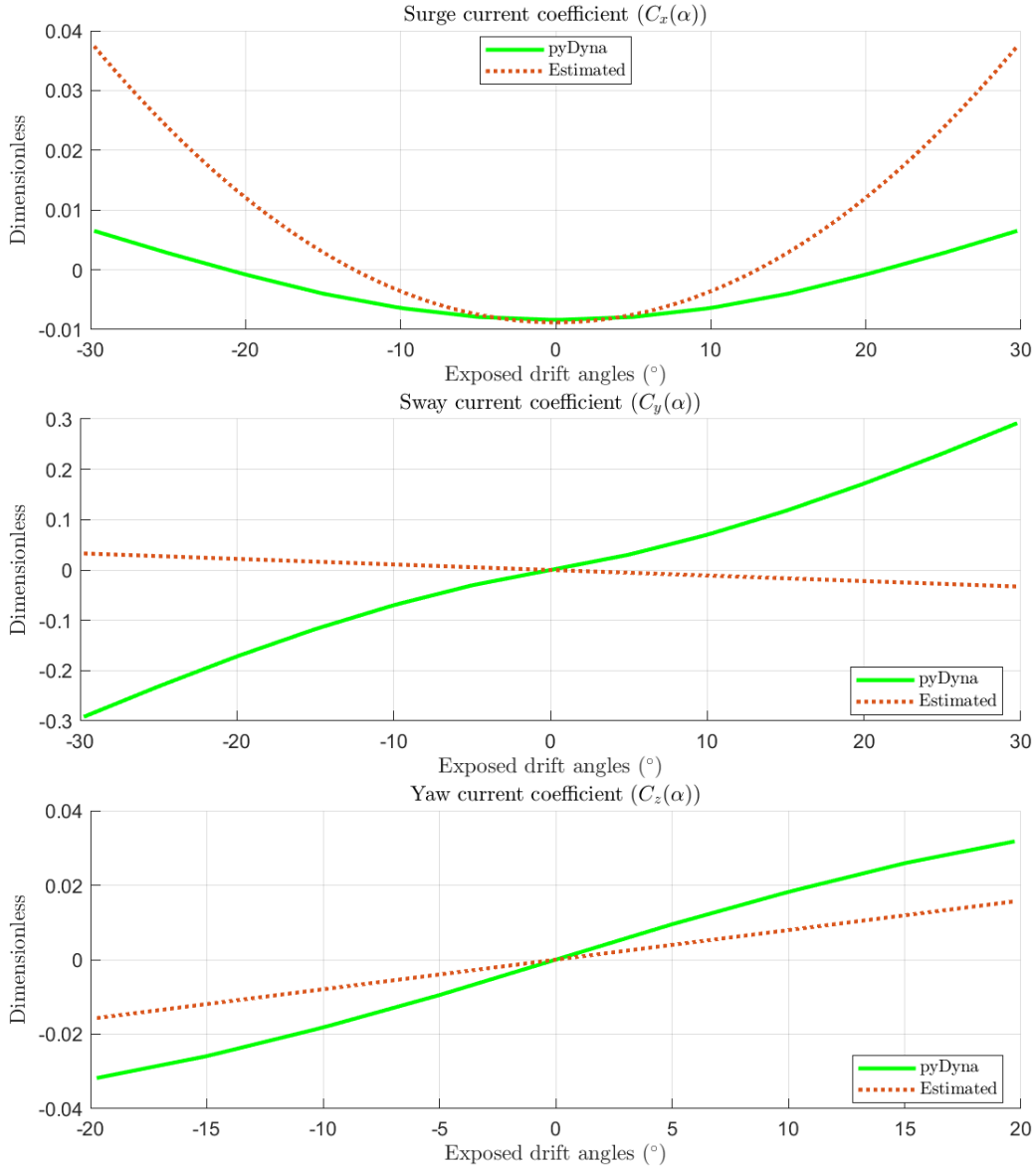

Figure 38: Estimated coefficients $C_x(\beta), C_y(\beta), C_z(\beta)$ in the simulated maneuver in Guanabara Bay plotted for generic drift angles.

Although the estimate of $X_{\beta\beta}$ diverged (Fig.36), due to the 1P estimate being accurate (Fig.21) and the simulated maneuver exposed the vessel to low variations of drift angles (Fig.33), the surge coefficient in Fig.38 ended being somehow very close to the real value.

The sway estimate being flipped in relation to the expected direction. At a first glance it would appear as an inconceivable behavior, however, by recalling the setup of the simulated maneuver (Fig.31), one can clearly see that the vessel has both current and wind components acting in port side of ship. As a consequence, the water ends with a pushing force in the starboard side. Due to the ship entering the channel making a counter-clock direction curve, the hydrodynamic resistance of the water would push it in the port side. Considering the first force is not modeled, such component would

indubitably ending by reflecting in the drift coefficient estimate itself. Fig.39 illustrates how these mentioned forces actuated on the ship during the maneuver.

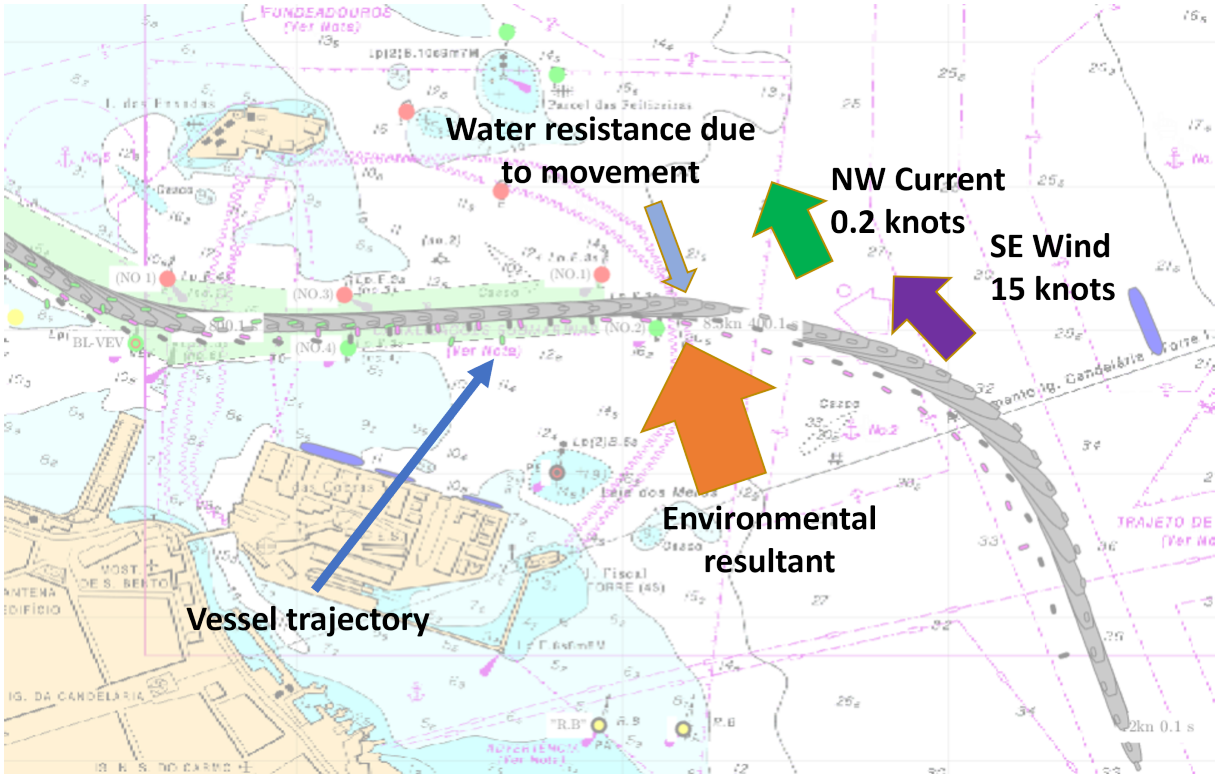

Figure 39: Explanation for the flipped behaviour on the sway parameter.

7.2 Estimate analyses

7.2.1 Summary of results for surge coefficient at $\beta = 0°$

Table 2 shows the compiled results obtained by the 1P estimator applied for all 10 vessels.

Table 2: Relation of results obtained from open sea maneuver.

Maneuver	C_0^x	$\hat{C}_0^x$	Steady surge speed	**Percentage error**	**Difference in surge force**
0	-0.0140	-0.0144	7.17 m/s	3.21 %	29.7 kN
1	-0.0114	-0.0115	7.51 m/s	1.93 %	21.1 kN
2	-0.0082	-0.0091	7.88 m/s	10.59 %	132.1 kN
3	-0.0095	-0.0098	7.87 m/s	3.74 %	51.9 kN
4	-0.0055	-0.0058	11.65 m/s	6.28 %	72.8 kN
5	-0.0102	-0.0128	10.63 m/s	21.35 %	517.8 kN
6	-0.0097	-0.0100	12.20 m/s	3.16 %	128.8 kN
7	-0.0084	-0.0088	10.44 m/s	4.41 %	95.6 kN
8	-0.0102	-0.0124	12.09 m/s	21.47 %	768.8 kN
9	-0.0101	-0.0104	12.14 m/s	3.14 %	130.4 kN

Apart from maneuvers 5 and 8 which had errors around 21 %, all others were accurate with the third highest being maneuver 2 with 10 % error followed by maneuver 4 with 6 % error.

Both steady speed and the difference found in the surge damping force obtained from the estimated drift coefficient $\hat{C}_0^x$ are also shown, yet these data could not lead to establish any direct strong correlation between them and the error values.

7.2.2 Drift angle analysis

One way to visualize if the approximation in (6.1) is sufficiently representative for modeling the drift coefficients is by looking at the presented box plot in Fig.40. The whiskers were set to englobe all data values (maximum and minimum).

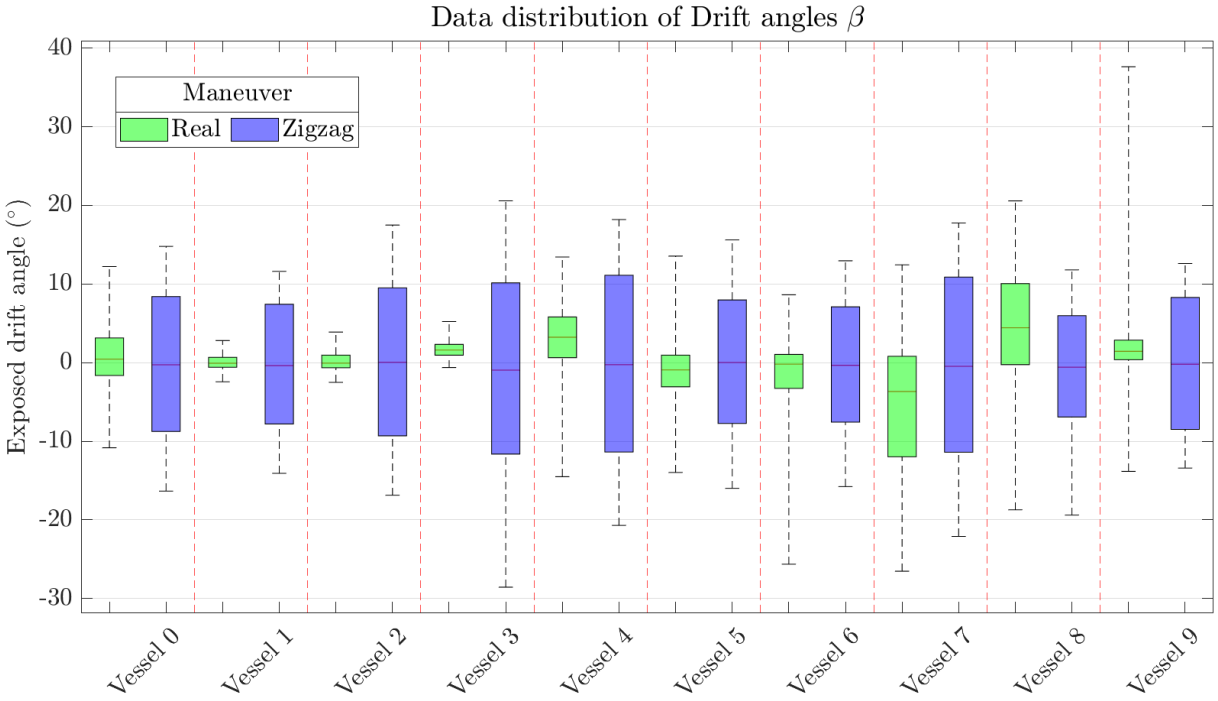

Figure 40: Data distribution of the estimated drift angles β in the real and zigzag maneuvers.

As expected from the ship motion mechanics, with the propeller and rudder being the principal responsible to excite the movement, the vessel will always tend to maintain low values of drift angles, even in scenarios with environmental conditions, as shown by the high data concentration around low drift angles (shorter boxes in green). In contrast, the zigzag maneuver (ITTC, 2002) produced higher drift angles and for longer duration (bigger boxes in blue), even in scenarios without environmental conditions.

All the evaluated maneuvers for the 3P estimator presented values of β that were most contained into the range of 10 degrees (being for one side or other), which reinforce the validity of the approximation (6.1), at least empirically and for a considerable real maneuver spectrum that fits within.

Another advantage of the box plot in Fig.40 is that it gives the information of the first and third quartiles. Therewith, one can know how the data is concentrated, as the interval delimited by these values define a 50 % percentile excluding the extremities. As such, they can be one form to characterize a maneuver. Notwithstanding, the other 50 % percentile related to the extremities could also influence the returned estimation, as the values of drift coefficients would further distance the approximation (6.1) adopted. Ergo, the analyses considered the whole spectrum of observed drift angles β.

7.2.3 Stipulated base values for drift dependent terms

In practice, the previously mentioned concern in 7.2.2 reflects essentially in questioning which approximation of the drift coefficients should be accepted as being the "true value" to compare with the obtained estimates. In contrast to the C_0^x, in which its value could be simply compared against the real surge coefficient C_x at zero degrees, depending on which interval is taken, the approximation (6.1) for the drift dependent terms $X_{\beta\beta}, Y_\beta, N_\beta$ results in different values. Visually, such problem can be seen in Fig.41 and Fig.42, as the slope of the linear interpolation is heavily shifted according to the considered angle interval.

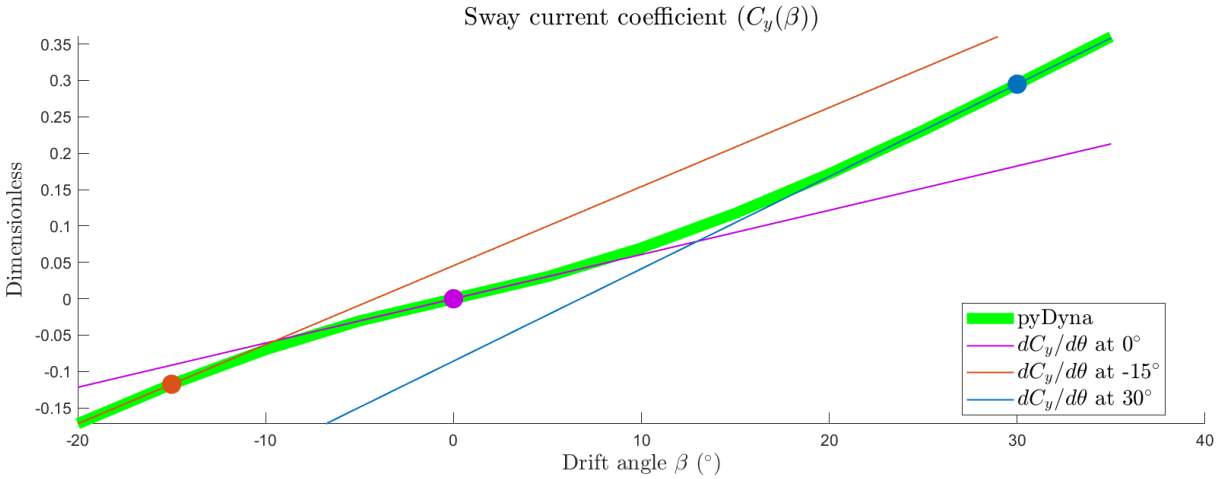

Figure 41: Comparison of sway drift coefficient derivatives for different values of angles.

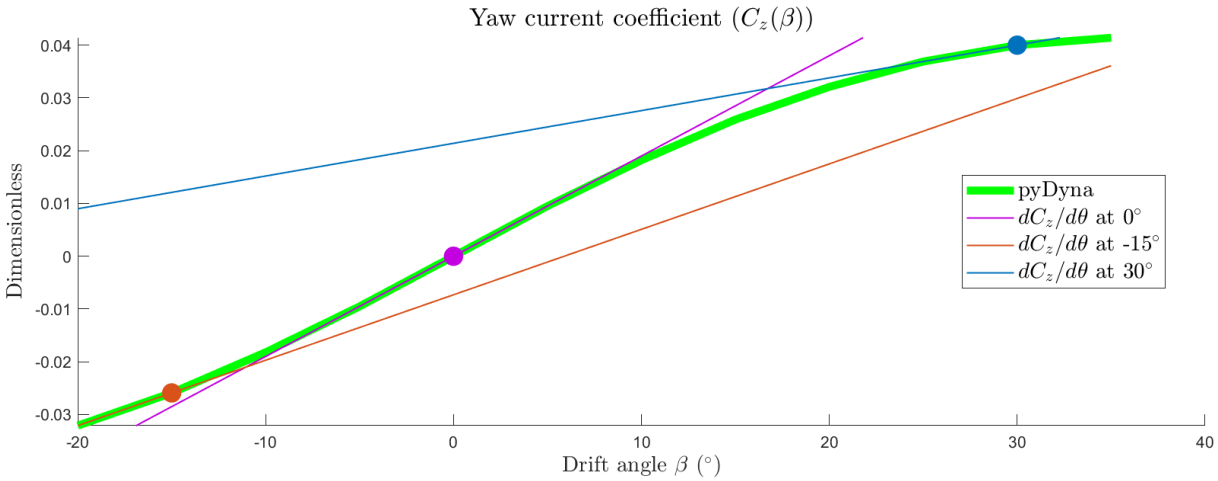

Figure 42: Comparison of yaw drift coefficient derivatives for different values of angles.

For each maneuver, the recorded maximum and minimum observed drift angles were taken to then define a range to search the maximum and minimum drift dependent terms

$X_{\beta\beta}, Y_{\beta}, N_{\beta}$. Taking also the maneuver 7 as illustrate this procedure, Fig.43, Fig.44 and Fig.45 show how these intervals impact on the estimation analysis.

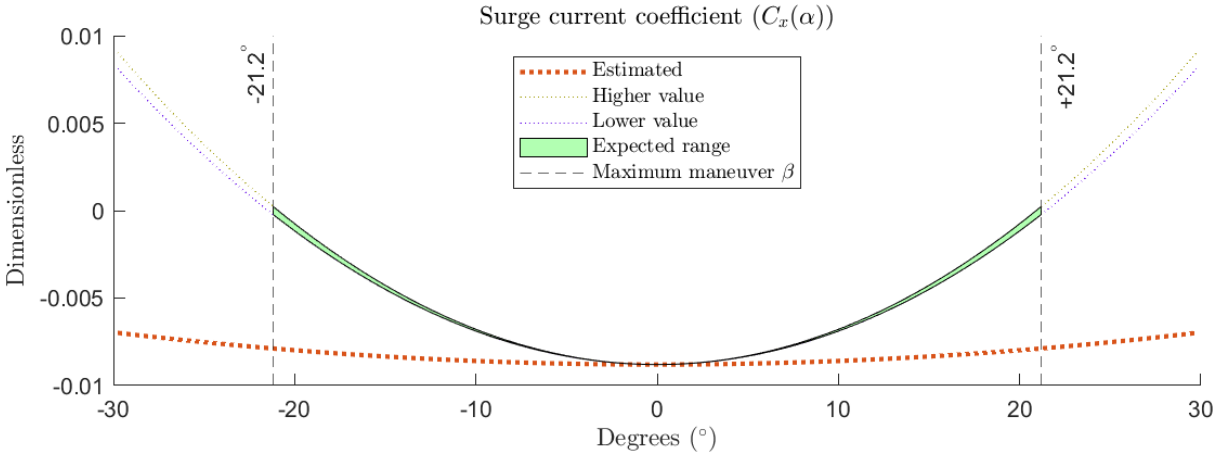

Figure 43: Surge coefficient visual analysis for the simulated zigzag 10/30 maneuver 7.

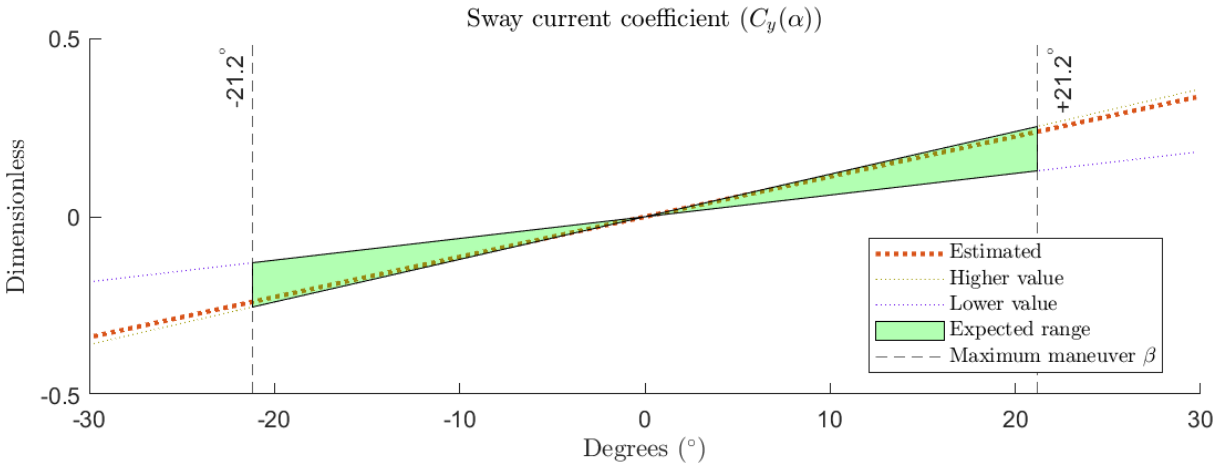

Figure 44: Sway coefficient visual analysis for simulated zigzag 10/30 maneuver 7.

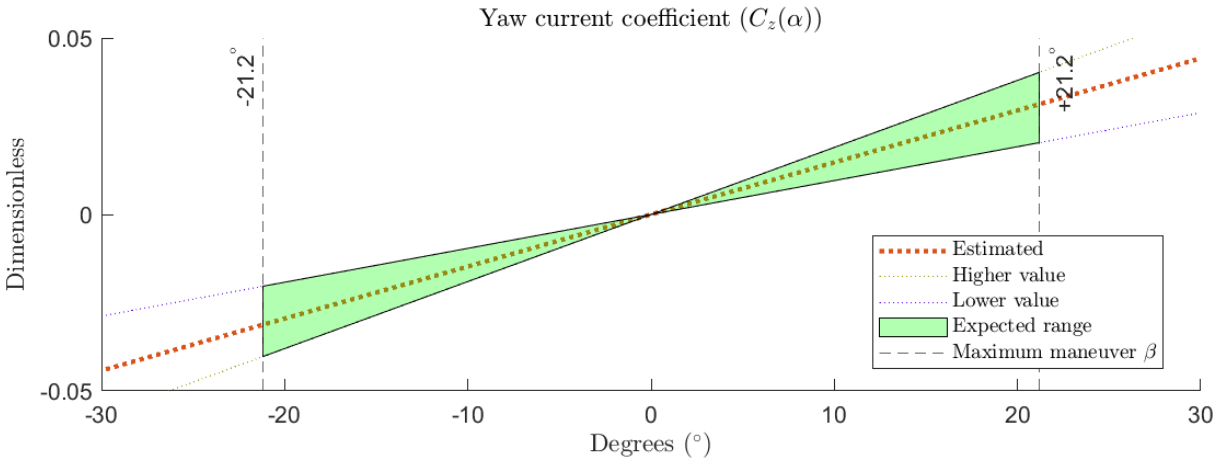

Figure 45: Yaw coefficient visual analysis for simulated zigzag 10/30 maneuver 7.

Due to having a single value to be compared with a certain range of possible values, an obtained estimate was considered sufficiently accurate if it was contained inside the expected range. If outside, another criterion of being tolerable close to one of the extremities was added (less than 20 % from any extremity). The flowchart in Fig.46 exposes more clearly the criteria to evaluate the obtained estimates.

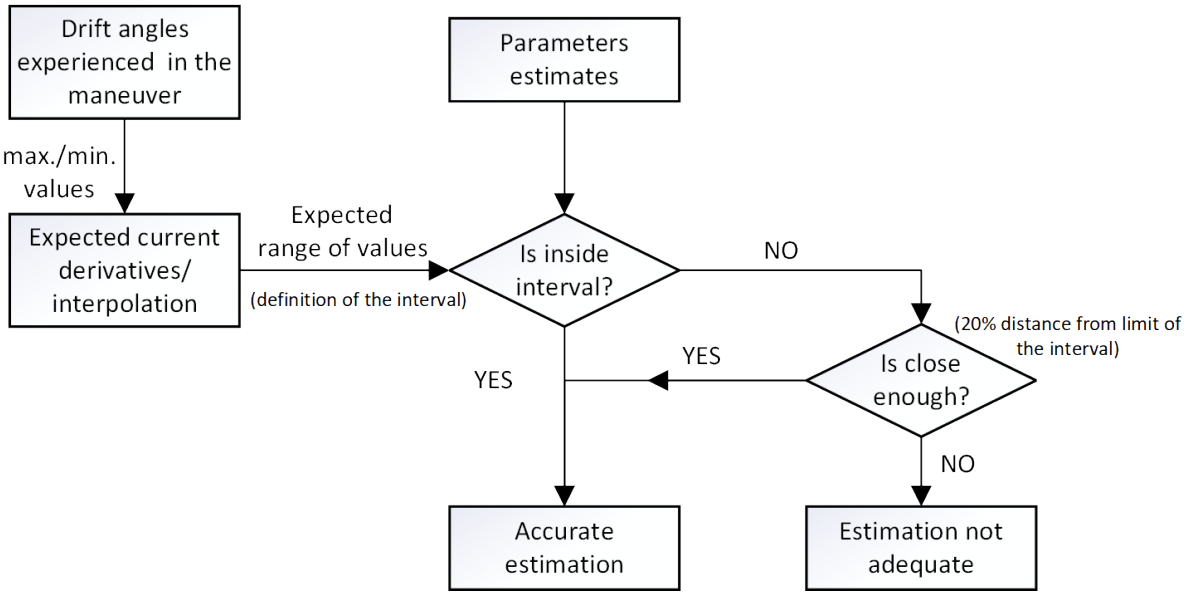

Figure 46: Flowchart to evaluate obtained estimates.

7.2.4 Tabled results for drift dependent terms

Tab.3 shows the obtained results from the 3P estimator applying the aforementioned procedure in Fig.46 applied for all vessels in the zigzag 10/30 maneuvers, while Tab.4 for the simulated maneuvers.

The first criterion for each maneuver has three possible outcomes: "higher", "lower" (referring to the direction where the estimate falls short, meaning it fails) or ✓(when the estimate is inside the acceptable range, indicating an accurate estimation). By passing through this, the second criterion becomes unnecessary, in these cases, the * represents exactly that; otherwise, the error percentage towards the closest border (minimum or maximum value) is given. Lastly, if a case has a ✓or has an error inferior than 20 % (highlighted in green), its estimate is given another ✓to indicate it was sufficiently accurate.

Table 3: Evaluation of drift dependent terms estimates for the zigzag 10/30 maneuvers.

Vessel	Inside range?			Error towards borders			Is accurate?		
	$X_{\beta\beta}$	Y_β	N_β	$X_{\beta\beta}$	Y_β	N_β	$X_{\beta\beta}$	Y_β	N_β
0	higher	lower	lower	159 %	3.13 %	2.12 %	no	✓	✓
1	higher	lower	lower	222 %	1.32 %	84.8 %	no	✓	no
2	higher	lower	lower	98.1 %	0.12 %	36.7 %	no	✓	no
3	higher	✓	✓	104 %	*	*	no	✓	✓
4	higher	lower	lower	269 %	58.6 %	13.1 %	no	no	✓
5	higher	✓	✓	39.2 %	*	*	no	✓	✓
6	lower	✓	lower	17.0 %	*	26.8 %	✓	✓	no
7	higher	✓	✓	87.4 %	*	*	no	✓	✓
8	lower	✓	lower	60.2 %	*	51.7 %	no	✓	no
9	lower	✓	lower	77.8 %	*	46.9 %	no	✓	no

Table 4: Evaluation of drift dependent terms estimates for the simulated maneuvers.

Vessel	Inside range?			Error towards borders			Is accurate?		
	$X_{\beta\beta}$	Y_β	N_β	$X_{\beta\beta}$	Y_β	N_β	$X_{\beta\beta}$	Y_β	N_β
0	higher	higher	higher	271 %	125 %	126 %	no	no	no
1	higher	✓	✓	58.4 %	*	*	no	✓	✓
2	higher	higher	lower	101 %	52.6 %	51.3 %	no	no	no
3	higher	higher	higher	71.0 %	33.7 %	11.3 %	no	no	✓
4	higher	✓	✓	84.1 %	*	*	no	✓	✓
5	higher	lower	lower	183 %	25.1 %	82.1 %	no	no	no
6	higher	lower	lower	135 %	68.1 %	17.2 %	no	no	✓
7	higher	lower	lower	157 %	78.1 %	20.2 %	no	no	no
8	higher	higher	lower	267 %	74.2 %	91.5 %	no	no	no
9	higher	lower	✓	67.4 %	76.4 %	28.0 %	no	no	✓

With the exception of the vessel 4, for the zigzag 10/30 maneuver, all other vessels could have their sway term Y_β accurately retrieved according to the adopted criteria. For the yaw term N_β, the success rate drop by 4 mismatches and finally the surge term $X_{\beta\beta}$ ended with the vessel 6 being the single pièce de résistance, including both set of maneuvers, achieving an error of 17 % to the lower extremity.

As for the simulated maneuvers, the rate drop notably for both sway and yaw, reached

2 and 4 accurate estimations respectively, indicating the high influence due to unmodelled environmental forces. Being said, at the current state, at least, the method should not be chosen in the context of port or restricted waters maneuvers.

Notwithstanding, the method overall showed mainly good experimental results in retrieving the sway parameter Y_β and above average for the yaw parameter N_β in zigzag maneuvers. In practice, this could infer in a good prospectus towards maneuvers with standardized variations such as sea-trials in open waters and with low incidence of environmental agents.

As for the surge parameter $X_{\beta\beta}$, in contrast to C_0^x, the estimates were far from ideal, most probably indicating some flaws regarding the validity of the method.

PART V

CONCLUSION

8 OVERVIEW OF THE OBTAINED RESULTS

8.1 Accuracy level and limitations encountered

The approximation in (6.1) allowed the application of two distinct estimators: the 1P (6.2.1) and the 3P (6.2.2). Notwithstanding, the applicability of these estimators was well delimited in a real scope scenario, with the former acting mainly in open seas (7.1.1) while the latter in confined port areas in which some maneuvering was required (7.1.3) or even in trial tests (7.1.2).

Recalling that the open sea maneuver (7.1.1) consisted in moving the ship purely in the longitudinal direction with a constant thrust rotation, eventually it is expected that the system will find an equilibrium of forces moving forward (propeller force) and forces in opposite direction, acting as a resistance against the motion (hydrodynamic resistance). In this scenario, assuming the latter as a parameter to be found in the KF point-of-view (1P estimator), it showed as a viable approach theoretically and also empirically, due to the satisfactory accuracy levels found in 7.2.1, with the worst estimates reaching the 20% mark (Tab.2).

On the other hand with the simulated maneuvers (7.1.3), the ship was continuously exposed to external environmental agents such as wind, current and waves. As these effects were neglected in the current proposed model, the 3P estimator incorporated some of their influence in the parameters estimates, as briefly shown in 7.1.3 with the sway force.

Intending to control these aforementioned externalities, a standard sea-trial maneuver was proposed, the zigzag 10/30 (7.1.2). It achieved a better estimation of the Y_β, given the adopted evaluation methodology (Fig.46). Still, the yaw parameter did not achieve the same level of success, presenting partially acceptable estimates. Some hypotheses to justify it recall in the expanded terms derived in A.1.2 and A.1.3, as they could lead to some exaggerated influence of the sway parameter Y_β in the calculation of the yaw moment; in the limitations around the simplification itself (6.1); or even in the sensibility

of the moment itself, that is more dependent on the different forces on the bow and stern of the ship and the hull format and details.

Regarding the surge parameter $X_{\beta\beta}$, the adopted parabola approximation (6.1), although apparently good enough once one already has the complete surge drift coefficient curve, in the context of parameter to be retrieved by a KF methodology faced some major problems. Firstly, as the values around the vertex showed a broad opening, adding to a limited exposition of drift angles, the parabola could easily be misinterpreted as a constant value. Secondly, the tested maneuvers faced the problem of not handling the correct inputted forces of the propeller thrust (Fig.27), which also incurred error in the rudder force, ending by affecting the surge estimate itself. Finally, even by correcting these previous problems, $X_{\beta\beta}$ presents in association with the quadratic of the drift angle, thus incurring a even further error if the latter is not sufficiently excited. In a scenario where it could be directly measured and used as an input for the system, perhaps it would not be much relevant, but as it is obtained in-maneuver by the composition of surge and sway speeds (4.27), which are also estimated, the final value could easily be corrupted by some noise, that is even worsen when elevated by two.

8.2 Related developed works

Throughout this research, three correlated papers were developed:

- **A Standards-Based Digital Twin of an Experiment with a Scale Model Ship**: This work proposed some standards to be adopted in a DT, envisioning not only current but also future implementation with different degrees of maturities. As an illustration to how some of the concepts could be applied, a study case was presented, using a scaled model Platform Supply Vessel (PSV) operated with a Dynamic System (DP) control (FONSECA et al., 2022).
- **Digital Twin of a Maneuvering ship: Real-time Estimation of Derivatives and Resistance Coefficient Based on Motion Sensors**: A first attempt to tackle the same problem presented any DT implementation, the representation of the model. The scope was delimited in a maneuvering ship scenario and the approach was to simplify the hydrodynamic forces and moment into slow-varying parameters in an EKF estimation problem (UEHARA SASAKI et al., 2021).
- **Digital Twin of a Maneuvering ship: Real-time Estimation of Drift and Resistance Coefficients Based on Ship Motion and Rudder and Propeller**

Commands: An evolution of the previous work, the model had been expanded to incorporate modular formulations for the propeller and rudder dynamics as well the filter changed to an UKF (UEHARA SASAKI; DE MELLO; TANNURI, 2022).

8.3 Results in DT point-of-view and future steps

Envisioning future DT applicability, the proposed method achieved limited success. By opting to utilize as few real-time information and few specific characteristics of the ship, the rudder and propeller dynamics could be well represented. At the same time, such models enhanced interpretability, as usually other maneuvering models used in parameter estimations loosely incorporate these terms.

The methodology could be proven feasible as partial information regarding the drift coefficients could be retrieved in real-time maneuver, in contrast to the usual CFD runs or captive tests. Evidently not proposing as a replacement to then, specially given the future improvements that shall be made in the mathematical model (environmental agents and the damping forces), the method can be implemented as a rapid analysis tool apart from the traditional monitoring aspect of DT technologies.

Towards a more general formulation that could tackle some of the observed limitations encountered in this work, future works shall investigate these aspects:

- Environmental agents
  - Wind modeling: ships are equipped with wind transducers that can retrieve some information regarding the gust and direction of the relative wind. Thence, expanding the modeling to incorporate this aspect is fairly feasible in a real DT application.
  - Wave modeling: although there is no fully reliable equipment inboard that can retrieve information of the incident waves in a ship, there is on-going research to use the vertical motions of the vessel to estimate the incident waves (ship-buoy analogy, for example (BISINOTTO et al., 2022)). This information about waves can be included in the models adopted in DT and improve parameter estimation.
  - Current modeling: ships have some capability to retrieve relative water velocity, yet they usually rely on instruments based in Acoustic Doppler Current Profiler (ADCP), which requires detecting the bottom of the sea. As such, they are not

very accurate and can have problems with high depth profiles. Analogous to the waves, by extrapolating current model information, tackling the modeling aspect becomes feasible in the DT framework.

- Estimation method:
  - Machine learning approaches: some implementations were already discussed in 3.2, nevertheless their effectiveness can lead to positive prospectus. Regarding interpretability issues mentioned in 3.3, methods mixed with some physical knowledge shall be preferable for a DT context, when some other complex analysis is taken.
  - Estimator choice: this work opted for the UKF as the tool for retrieving online the parameters. Perhaps investigating other possibilities such as the Particle Filter or even assimilating some techniques from post-processing analysis for towing experiments could elevate the degree of accuracy of this same model.

REFERENCES

ABKOWITZ, M. A. **Lectures on Ship Hydrodynamics – Steering and Maneuverability**. Lyngby, Denmark: Hydro-Og Aerodynamisk Laboratorium, May 1964. (Report No. Hy-5). Cit. on p. 34.

BISINOTTO, G. A.; COTRIM, L. P.; COZMAN, F. G.; TANNURI, E. A. Assessment of Sea State Estimation With Convolutional Neural Networks Based on the Motion of a Moored FPSO Subjected to High-Frequency Wave Excitation. In: INTERNATIONAL CONFERENCE ON OCEAN, OFFSHORE AND ARTIC ENGINEERING (OMAE), 41., 2022, Hamburg, Germany. **Volume 5B: Ocean Engineering; Honoring Symposium for Professor Günther F. Clauss on Hydrodynamics and Ocean Engineering**. American Society of Mechanical Engineers (ASME), June 2022. ISBN 978-0-7918-8590-1. DOI: 10.1115/OMAE2022-78603. Cit. on p. 86.

CASADO, M. H.; FERREIRO, R. Identification of the nonlinear ship model parameters based on the turning test trial and the backstepping procedure. **Ocean Engineering**, American Society of Mechanical Engineers (ASME), v. 32, n. 11-12, p. 1350–1369, Aug. 2005. ISSN 00298018. DOI: 10.1016/j.oceaneng.2004.11.003. Cit. on pp. 15, 17.

CHIU, F.-C.; CHANG, T.-L.; GO, J.; CHOU, S.-K.; CHEN, W.-C. A recursive neural networks model for ship maneuverability prediction. In: OCEANS MTS/IEEE TECHNO-OCEAN (IEEE CAT. NO.04CH37600), 9-12 Nov. 2004, Kobe, Japan. **Proceedings**. IEEE, 2004. p. 1211–1218. ISBN 0-7803-8669-8. DOI: 10.1109/OCEANS.2004.1405752. Cit. on p. 16.

DANIELSEN-HACES, A. **Digital Twin Development: Condition Monitoring and Simulation Comparison for the ReVolt Autonomous Model Ship**. June 2018. MA thesis – Norwegian University of Science and Technology (NTNU). Cit. on p. 13.

DARWIN, C. Note on hydrodynamics. **Mathematical Proceedings of the Cambridge Philosophical Society**, v. 49, p. 342–354, 2 Apr. 1953. ISSN 0305-0041. DOI: 10.1017/S0305004100028449. Cit. on p. 23.

DUNN, P. F. **Measurement and Data Analysis for Engineering and Science**. 2. ed. Indiana, USA: CRC Press, 2010. Cit. on p. 3.

ERIKSTAD, S. O. Design Patterns for Digital Twin Solutions in Marine Systems Design and Operations. In: CONFERENCE ON COMPUTER AND IT APPLICATIONS IN THE MARITIME INDUSTRIES (COMPIT), 17., May 2018, Pavone, Italy. **Proceedinds**. Hamburg, Germany: Technische Universität Hamburg-Harburg, 2018. p. 354–363. ISBN 978-3-89220-707-8. Cit. on p. 13.

— Merging Physics, Big Data Analytics and Simulation for the Next-Generation Digital Twins. In: SYMPOSIUM ON HIGH-PERFORMANCE MARINE VEHICLES (HIPER), 11., Sept. 2017, Zevenwacht, South-Africa. **Proceedings**. Hamburg, Germany: Technische Universität Hamburg-Harburg, 2017. p. 140–150. ISBN 978-3-89220-702-3. Cit. on pp. 7–9.

FALTINSEN, O. **Sea loads on ships and offshore structures**. United States: Cambridge University Press, Jan. 1993. ISBN 9780521458702. Cit. on p. 31.

FONSECA, Í. A.; GASPAR, H. M.; DE MELLO, P. C.; UEHARA SASAKI, H. A. A Standards-Based Digital Twin of an Experiment with a Scale Model Ship. **Computer-Aided Design**, v. 145, p. 103191, Apr. 2022. ISSN 00104485. DOI: 10.1016/j.cad.2021.103191. Cit. on p. 85.

FOSSEN, T. I. **Handbook of Marine Craft Hydrodynamics and Motion Control**. Chichester, UK: John Wiley & Sons, Ltd, Apr. 2011. ISBN 9781119994138. DOI: 10.1002/9781119994138. Cit. on pp. 22–24, 28, 30, 31, 36.

FUCATU, C.; NISHIMOTO, K. An Empirical Model of Current Shadow Effect. In: INTERNATIONAL CONFERENCE ON OCEAN, OFFSHORE AND ARTIC ENGINEERING (OMAE), 23., 20-25 June 2004, Vancouver, British Columbia, Canada. **Volume 1, Parts A and B**. American Society of Mechanical Engineers (ASME), 2004. p. 769–776. DOI: 10.1115/OMAE2004-51432. Cit. on p. 32.

GRIEVES, M.; VICKERS, J. In: KAHLEN, J.; FLUMERFELT, S.; ALVES, A. **Digital Twin: Mitigating Unpredictable, Undesirable Emergent Behavior in Complex Systems**. Springer, Cham, Aug. 2017. p. 85–113. ISBN 978-3-319-38754-3. DOI: 10.1007/978-3-319-38756-7_4. Cit. on p. 12.

HAJIZADEH, S.; SEIF, M.; MEHDIGHOLI, H. Determination of ship maneuvering hydrodynamic coefficients using system identification technique based on free-running model test. **Scientia Iranica**, v. 23, p. 2154–2165, Oct. 2016. DOI: 10.24200/sci.2016.3945. Cit. on pp. 15, 17.

HESS, D.; FALLER, W. Twenty-Third Symposium on Naval Hydrodynamics. In: SYMPOSIUM ON NAVAL HYDRODYNAMICS, 23., 17-22 Sept. 2001, Val de Reuil, France. **Proceedings**. Washington, DC, USA: National Academies Press, Dec. 2001. p. 223–242. ISBN 978-0-309-25467-0. DOI: 10.17226/10189. Cit. on p. 16.

HOERNER, S. F. **Fluid-Dynamic Drag**. by the Author, 1965. Cit. on p. 27.

ISERMANN, R.; MÜNCHHOF, M. **Identification of Dynamic Systems**: An Introduction with Applications. 1. ed. Berlin, Germany: Springer, 2011. ISBN 978-3-540-78878-2. DOI: 10.1007/978-3-540-78879-9. Cit. on p. 48.

ITTC. **1978 ITTC Performance Prediction Method**. Version Revision 04 (Approved by the 28th ITTC), 2017. chap. 7.5-02-03-01.4. (ITTC – Recommended Procedures and Guidelines). Cit. on p. 27.

— **Testing and Extrapolation Methods Resistance Resistance Test**. Version Revision 01 (Approved by the 23rd ITTC), 2002. chap. 7.5-02-02-01. (ITTC – Recommended Procedures and Guidelines). Cit. on pp. 50, 56, 62, 77.

JULIER, S. J.; UHLMANN, J. K. New extension of the Kalman filter to nonlinear systems. In: AEROSENSE, 1997, Orlando, FL, USA. **Proceedings Volume 3068, Signal Processing, Sensor Fusion, and Target Recognition VI**. Ed. by I. Kadar: International Society for Optics and Photonics (SPIE), 1997. p. 182–193. DOI: 10.1117/12.280797. Cit. on pp. 42, 43.

KAGERMANN, H.; WAHLSTER, W.; HELBIG, J. **Recommendations for implementing the strategic initiative Industrie 4.0: Final report of the Industrie 4.0 Working Group**. Munich, Germany, Apr. 2013. Cit. on p. 12.

KÄLLSTRÖM, C. G.; ÅSTRÖM, K. J. Experiences of system identification applied to ship steering. **Automatica**, v. 17, n. 1, p. 187–198, 1981. ISSN 0005-1098. DOI: 10.1016/0005-1098(81)90094-7. Cit. on p. 15.

KALMAN, R. E. A New Approach to Linear Filtering and Prediction Problems. **Journal of Basic Engineering**, American Society of Mechanical Engineers (ASME), v. 82, n. 1, p. 35–45, Mar. 1960. DOI: 10.1115/1.3662552. Cit. on p. 40.

KOSE, K.; YUMURO, A.; YOSHIMURA, Y. Mathematical Model for Manoeuvring Ship Motion (MMG Model). (Japanese). In: SYMPOSIUM ON SHIP MANOEAUVERABILITY, 3. **Proceedings**. Tokyo, Japan: Japan Society of Naval Architects and Ocean Engineers (JASNAOE), Dec. 1981. p. 27–80. Cit. on pp. 21, 37.

KRSTIĆ, M.; KANELLAKOPOULOS, I.; KOKOTOVIĆ, P. V. **Nonlinear and Adaptive Control Design**. Ed. by S. Haykim. New York, USA: John Wiley and Sons, 1995. (A Volume in the Wiley Series on Adaptive and Learning Systems for Signal Processing, Communications, and Control). Cit. on p. 16.

LEITE, A. J. P.; ARANHA, J. A. P.; UMEDA, C.; DE CONTI, M. B. Current forces in tankers and bifurcation of equilibrium of turret systems: hydrodynamic model and experiments. **Applied Ocean Research**, v. 20, p. 145–156, 3 June 1998. ISSN 01411187. DOI: 10.1016/S0141-1187(98)00002-9. Cit. on pp. 50, 51.

LEWIS, E. V. **Principles of Naval Architecture Second Revision Volume II Resistance, Propulsion and Vibration**. Ed. by E. V. Lewis. 3. ed. Jersey City, NJ, USA: The Society of Naval Architects and Marine Engineers (SNAME), 1988. v. 2. Cit. on pp. 20, 26.

LEWIS, F. L.; XIE, L.; POPA, D. **Optimal and Robust Estimation**. 2. ed. Boca Raton, FL, USA: CRC Press, Dec. 2017. ISBN 9781315221656. DOI: 10.1201/9781315221656. Cit. on pp. 40, 41.

LI, X. R.; JILKOV, V. Survey of maneuvering target tracking . Part I: dynamic models. **IEEE Transactions on Aerospace and Electronic Systems**, IEEE, v. 39, p. 1333–1364, 4 Oct. 2003. ISSN 0018-9251. DOI: 10.1109/TAES.2003.1261132. Cit. on p. 15.

LIU, J.; HEKKENBERG, R. Sixty years of research on ship rudders: effects of design choices on rudder performance. **Ships and Offshore Structures**, v. 12, n. 4, p. 495–512, May 2017. ISSN 1744-5302. DOI: 10.1080/17445302.2016.1178205. Cit. on p. 37.

LJUNG, L. **System Identification**: Theory for the User. Ed. by T. Kailath. 2. ed. Upper Saddle River, New Jersey, USA: Prentice-Hall, 1998. (Information and System Sciences Series). ISBN 9780132440530. Cit. on p. 14.

LUO, W. Parameter Identifiability of Ship Manoeuvring Modeling Using System Identification. **Mathematical Problems in Engineering**, v. 1, p. 1–10, 2016. ISSN 1024-123X. DOI: 10.1155/2016/8909170. Cit. on p. 16.

LUO, W.; MOREIRA, L.; GUEDES SOARES, C. Manoeuvring simulation of catamaran by using implicit models based on support vector machines. **Ocean Engineering**, v. 82, p. 150–159, May 2014. ISSN 00298018. DOI: 10.1016/j.oceaneng.2014.03.008. Cit. on p. 16.

MA, F. C.; TONG, S. H. Real time parameters identification of ship dynamic using the extended Kalman filter and the second order filter. In: CONFERENCE ON CONTROL APPLICATIONS (CCA), 25 June 2003, Istanbul, Turkey. **Proceedings**. IEEE, 2003. v. 2, p. 1245–1250. DOI: 10.1109/CCA.2003.1223189. Cit. on pp. 15, 17.

MADNI, A. M.; MADNI, C. C.; LUCERO, S. D. Leveraging Digital Twin Technology in Model-Based Systems Engineering. **Systems**, v. 7, n. 1, 2019. ISSN 2079-8954. DOI: 10.3390/systems7010007. Cit. on pp. 8, 9.

MADYASTHA, V.; RAVINDRA, V.; MALLIKARJUNAN, S.; GOYAL, A. Extended Kalman Filter vs. Error State Kalman Filter for Aircraft Attitude Estimation. In: AIAA GUIDANCE, NAVIGATION, AND CONTROL CONFERENCE, 2011, Portland, Oregon, USA. **Proceedings**. Reston, Virigina, USA: American Institute of Aeronautics and Astronautics, Aug. 2011. ISBN 978-1-60086-952-5. DOI: 10.2514/6.2011-6615. Cit. on p. 42.

MARTINS, P. T.; LOBO, V. Estimating Maneuvering and Seakeeping Characteristics with Neural Networks. In: OCEANS '07 IEEE ABERDEEN, 18-21 June 2007, Aberdeen, UK. **Proceedings**. IEEE, 2007. p. 1–5. ISBN 978-1-4244-0634-0. DOI: 10.1109/OCEANSE.2007.4302465. Cit. on p. 16.

MEI, B.; SUN, L.; SHI, G. White-Black-Box Hybrid Model Identification Based on RM-RF for Ship Maneuvering. **IEEE Access**, v. 7, p. 57691–57705, 2019. ISSN 2169-3536. DOI: 10.1109/ACCESS.2019.2914120. Cit. on p. 16.

MILAKOVIĆ, A.-S.; LI, F.; MAROUF, M.; EHLERS, S. A machine learning-based method for simulation of ship speed profile in a complex ice field. **Ships and Offshore Structures**, v. 15, n. 9, p. 974–980, Oct. 2020. ISSN 1744-5302. DOI: 10.1080/17445302.2019.1697075. Cit. on p. 16.

MOLLAND, A.; TURNOCK, S. **Marine Rudders and Control Surfaces**: Principles, Data, Design and Applications. 1. ed.: Elsevier Ltd., 2007. ISBN 978-0-7506-6944-3. DOI: 10.1016/B978-0-7506-6944-3.X5000-8. Cit. on pp. 21, 37.

MOLLAND, A. F.; TURNOCK, S. R.; HUDSON, D. A. **Ship Resistance and Propulsion**. 2. ed. Cambridge, UK: Cambridge University Press, Aug. 2017. ISBN 9781316494196. DOI: 10.1017/9781316494196. Cit. on pp. 25–27.

MOREIRA, L.; GUEDES SOARES, C. Dynamic model of manoeuvrability using recursive neural networks. **Ocean Engineering**, v. 30, p. 1669–1697, 13 Sept. 2003. ISSN 00298018. DOI: 10.1016/S0029-8018(02)00147-6. Cit. on p. 16.

NEGRI, E.; FUMAGALLI, L.; MACCHI, M. A Review of the Roles of Digital Twin in CPS-based Production Systems. **Procedia Manufacturing**, v. 11, p. 939–948, 2017. ISSN 2351-9789. DOI: 10.1016/j.promfg.2017.07.198. Cit. on pp. 7, 9.

NEWMAN, J. N. **Marine Hydrodynamics**. The MIT Press, 1977. ISBN 9780262280617. DOI: 10.7551/mitpress/4443.001.0001. Cit. on pp. 23–25.

NOMOTO, K.; TAGUCHI, T.; HONDA, K.; HIRANO, S. On the steering qualities of ships. **International Shipbuilding Progress**, v. 4, n. 35, p. 354–370, July 1957. ISSN 15662829. DOI: 10.3233/ISP-1957-43504. Cit. on pp. 15, 17.

OBOKATA, J. On The Basic Design of Single Point Mooring Systems, 1st Report: Applications of The Dynamic Stability Analysis to the Primary Planning of the System. (Japanese). **Journal of the Society of Naval Architects of Japan**, v. 161, 1987. Cit. on pp. 31, 50.

OOSTERVELD, M. W. C. Advances in maritime hydrodynamic research during the last century. In: INTERNATIONAL COLLOQUIUM "INDUSTRIAL REVOLUTIONS AND THE SEA", 28-31 Mar. 1989. **Proceedings**. Ed. by C. Koninckx. Brussels, Belgium: Wetenschappelijk Comité voor Maritieme Geschiedenis. Koninklijke Academie voor Wetenschappen, Letteren en Schone Kunsten van België, 1991. Collectanea Maritima V, p. 153–165. ISBN 90-6569-447-1. Cit. on p. 2.

OUYANG, Z.-L.; ZOU, Z.-J. Nonparametric modeling of ship maneuvering motion based on Gaussian process regression optimized by genetic algorithm. **Ocean Engineering**, v. 238, p. 109699, Oct. 2021. ISSN 00298018. DOI: 10.1016/j.oceaneng.2021.109699. Cit. on p. 16.

PARROTT, A.; WARSHAW, L. **Industry 4.0 and the digital twin**. 12 May 2017. Available from: ¡https://www2.deloitte.com/us/en/insights/focus/industry-4-0/digital-twin-technology-smart-factory.html¿. Visited on: 16 July 2019. Cit. on p. 8.

PERERA, L. P.; OLIVEIRA, P.; GUEDES SOARES, C. System Identification of Nonlinear Vessel Steering. **Journal of Offshore Mechanics and Arctic Engineering**, American Society of Mechanical Engineers (ASME), v. 137, n. 3, June 2015. ISSN 0892-7219. DOI: 10.1115/1.4029826. Cit. on pp. 15, 17.

— System Identification of Vessel Steering With Unstructured Uncertainties by Persistent Excitation Maneuvers. **IEEE Journal of Oceanic Engineering**, IEEE, v. 41, n. 3, p. 1–14, 2016. ISSN 0364-9059. DOI: 10.1109/JOE.2015.2460871. Cit. on pp. 15, 17.

RASHEED, A.; SAN, O.; KVAMSDAL, T. Digital Twin: Values, Challenges and Enablers From a Modeling Perspective. **IEEE Access**, v. 8, p. 21980–22012, 2020. DOI: 10.1109/ACCESS.2020.2970143. Cit. on p. 12.

RØDSETH, Ø.; PERERA, L. P.; MO, B. Big data in shipping: Challenges and opportunities. In: INTERNATIONAL CONFERENCE ON COMPUTER AND IT APPLICATIONS IN THE MARITIME INDUSTRIES (COMPIT), 15., 2016, Lecce, Italy. **Proceedinds**. Hamburg, Germany: Technische Universität Hamburg-Harburg, May 2016. p. 361–373. Cit. on p. 13.

SHI, C.; ZHAO, D.; PENG, J.; SHEN, C. Identification of Ship Maneuvering Model Using Extended Kalman Filters. **TransNav, the International Journal on Marine Navigation and Safety of Sea Transportation**, Gdynia Maritime University, Faculty of Navigation, v. 3, n. 1, p. 105–110, 2009. ISSN 2083-6473. Cit. on pp. 15, 17.

SIMON, D. Kalman filtering with state constraints: a survey of linear and nonlinear algorithms. **IET Control Theory & Applications**, Institution of Engineering and Technology, v. 4, 1303–1318(15), 8 Aug. 2010. ISSN 1751-8644. Cit. on p. 46.

— **Optimal State Estimation**: Kalman, H_∞, and Nonlinear Approaches. Hoboken, NJ, USA: John Wiley & Sons, Inc., May 2006. ISBN 9780470045343. DOI: 10.1002/0470045345. Cit. on p. 47.

SIMON, D.; SIMON, D. L. Kalman filtering with inequality constraints for turbofan engine health estimation. **IEE Proceedings - Control Theory and Applications**, v. 153, 371–378(7), 3 May 2006. DOI: 10.1049/ip-cta:20050074. Cit. on p. 47.

SIMOS, A. N.; TANNURI, E. A.; PESCE, C. P.; ARANHA, J. A. P. A Quasi-Explicit Hydrodynamic Model for the Dynamic Analysis of a Moored FPSO Under Current Action. **Journal of Ship Research**, v. 45, n. 04, p. 289–301, Dec. 2001. ISSN 0022-4502. DOI: 10.5957/jsr.2001.45.4.289. Cit. on p. 50.

STAPERSMA, D.; WOUD, H. K. Matching propulsion engine with propulsor. **Journal of Marine Engineering & Technology**, Taylor & Francis, v. 4, n. 2, p. 25–32, 2005. DOI: 10.1080/20464177.2005.11020189. Cit. on pp. 20, 36.

STEEN, S. **Experimental Methods in Marine Hydrodynamics (TMR7)**. 2014. Lecture notes. Cit. on p. 2.

STORCH, R. L.; HAMMON, C. P.; BUNCH, H. M.; RICAHRD, C. M. **Ship Production**. 2. ed. Cetreville, Maryland, USA: Cornell Maritime Press, 1995. v. 2. Cit. on p. 19.

TANNURI, E. A.; MARTINS, G. H. A. Application of a Maneuvering Simulation Center and Pilots Expertise to the Design of New Ports and Infrastructure Optimization in Brazil. In: PIANC-WORLD CONGRESS, 34., 2018, Panama City, Panama. **Proceedings**. 2018. Cit. on p. 57.

TANNURI, E. A.; RATEIRO, F.; FUCATU, C. H.; FERREIRA, M. D.; MASETTI, I. Q.; NISHIMOTO, K. Modular Mathematical Model for a Low-Speed Maneuvering Simulator. In: INTERNATIONAL CONFERENCE ON OCEAN, OFFSHORE AND ARTIC ENGINEERING (OMAE), 33., 8-13 June 2014, San Francisco, California, USA. **Volume 1B: Offshore Technology**. American Society of Mechanical Engineers (ASME), 2014. ISBN 978-0-7918-4538-7. DOI: 10.1115/OMAE2014-24414. Cit. on pp. 32, 50.

TEIXEIRA, B. O. S.; TÔRRES, L. A. B.; AGUIRRE, L. A.; BERNSTEIN, D. S. On unscented Kalman filtering with state interval constraints. **Journal of Process Control**, v. 20, n. 1, p. 45–57, 2010. ISSN 0959-1524. DOI: 10.1016/j.jprocont.2009.10.007. Cit. on p. 47.

— Unscented filtering for interval-constrained nonlinear systems. In: CONFERENCE ON DECISION AND CONTROL (CDC), 47., 2008, Cancun, Mexico. **Proceedings**. IEEE, 2008. p. 5116–5121. DOI: 10.1109/CDC.2008.4739141. Cit. on pp. 47, 48.

UEHARA SASAKI, H. A.; DE MELLO, P. C.; TANNURI, E. A. Digital Twin Of A Maneuvering Ship: Real-Time Estimation Of Drift And Resistance Coefficients Based On Ship Motion And Rudder And Propeller Commands. In: INTERNATIONAL CONFERENCE ON OCEAN, OFFSHORE AND ARTIC ENGINEERING (OMAE), 41., 2022, Hamburg, Germany. **Volume 5B: Ocean Engineering; Honoring Symposium for Professor Günther F. Clauss on Hydrodynamics and Ocean Engineering**. American Society of Mechanical Engineers (ASME), June 2022. ISBN 978-0-7918-8590-1. DOI: 10.1115/OMAE2022-78714. Cit. on pp. 17, 50, 86.

UEHARA SASAKI, H. A.; IANAGUI, A. S. S.; MELLO, P. C. DE; TANNURI, E. A. Digital Twin of a Maneuvering Ship: Real-Time Estimation of Derivatives and Resistance Coefficient Based on Motion Sensor. In: INTERNATIONAL CONFERENCE ON OCEAN, OFFSHORE AND ARTIC ENGINEERING (OMAE), 40., 2021, Virtual, Online. **Volume 6: Ocean Engineering**. American Society of Mechanical Engineers (ASME), June 2021. ISBN 978-0-7918-8516-1. DOI: 10.1115/OMAE2021-62899. Cit. on pp. 17, 50, 85.

VAN AMERONGEN, J.; UDINK TEN CATE, A. Model reference adaptive autopilots for ships. **Automatica**, v. 11, n. 5, p. 441–449, July 1975. ISSN 00051098. DOI: 10.1016/0005-1098(75)90020-5. Cit. on p. 15.

VECTORNAV. **Product brochure**. Accessed: May 28th, 2019. Cit. on p. 57.

WAKITA, K.; MAKI, A.; UMEDA, N.; MIYAUCHI, Y.; SHIMOJI, T.; RACHMAN, D. M.; AKIMOTO, Y. On neural network identification for low-speed ship maneuvering model. **Journal of Marine Science and Technology**, v. 27, n. 1, p. 772–785, Mar. 2022. ISSN 0948-4280. DOI: 10.1007/s00773-021-00867-1. Cit. on p. 16.

WAN, E. A.; VAN DER MERWE, R. The unscented Kalman filter for nonlinear estimation. In: ADAPTIVE SYSTEMS FOR SIGNAL PROCESSING, COMMUNICATIONS, AND CONTROL SYMPOSIUM (ASSPCC), 4 Oct. 2000, Lake Louise, AB, Canada. **Proceedings of the IEEE 2000 (Cat. No.00EX373)**. IEEE, 2000. p. 153–158. DOI: 10.1109/ASSPCC.2000.882463. Cit. on p. 58.

WANG, Y.; PERERA, L. P.; BATALDEN, B.-M. Particle Filter Based Ship State and Parameter Estimation for Vessel Maneuvers. In: INTERNATIONAL OCEAN AND POLAR ENGINEERING CONFERENCE (ISOPE), 31., 20-25 June 2021, Rhodes, Greece. **Proceedings**. 2021. ISOPE-I-21-4176. Cit. on p. 15.

WORDEN, K.; CROSS, E. J.; GARDNER, P.; BARTHORPE, R. J.; WAGG, D. J. On digital twins, mirrors and virtualisations. In: CONFERENCE AND EXPOSITION ON STRUCTURAL DYNAMICS (IMAC), 37., 3-06 June 2019, Reno, NV, USA. **Model Validation and Uncertainty Quantification**. Ed. by R. J. Barthorpe: Springer, Cham, 2020. v. 3, p. 285–295. Conference Proceedings of the Society for Experimental Mechanics Series. DOI: 10.1007/978-3-030-12075-7_34. Cit. on pp. 7, 9, 11.

WRIGHT, L.; DAVIDSON, S. How to tell the difference between a model and a digital twin. **Advanced Modeling and Simulation in Engineering Sciences**, v. 7, p. 13, 1 Dec. 2020. ISSN 2213-7467. DOI: 10.1186/s40323-020-00147-4. Cit. on p. 7.

XU, H.; HINOSTROZA, M. A.; HASSANI, V.; GUEDES SOARES, C. Real-Time Parameter Estimation of a Nonlinear Vessel Steering Model Using a Support Vector Machine. **Journal of Offshore Mechanics and Arctic Engineering**, American Society of Mechanical Engineers (ASME), v. 141, n. 6, Dec. 2019. ISSN 0892-7219. DOI: 10.1115/1.4043806. Cit. on p. 16.

XU, H.; HINOSTROZA, M. A.; WANG, Z.; GUEDES SOARES, C. Experimental investigation of shallow water effect on vessel steering model using system identification method. **Ocean Engineering**, v. 199, p. 106940, Mar. 2020. ISSN 00298018. DOI: 10.1016/j.oceaneng.2020.106940. Cit. on p. 16.

XUE, Y.; LIU, Y.; JI, C.; XUE, G.; HUANG, S. System identification of ship dynamic model based on Gaussian process regression with input noise. **Ocean Engineering**, v. 216, p. 107862, Nov. 2020. ISSN 00298018. DOI: 10.1016/j.oceaneng.2020.107862. Cit. on p. 16.

YASUKAWA, H.; YOSHIMURA, Y. Introduction of MMG standard method for ship maneuvering predictions. **Journal of Marine Science and Technology**, Japan Society of Naval Architects and Ocean Engineers (JASNAOE), v. 20, n. 1, p. 37–52, 2015. ISSN 0948-4280. DOI: 10.1007/s00773-014-0293-y. Cit. on p. 37.

ŻELAZNY, K. Approximate Method of Calculating Forces on Rudder During Ship Sailing on a Shipping Route. **TransNav, the International Journal on Marine Navigation and Safety of Sea Transportation**, v. 8, p. 459–464, 3 2014. ISSN 2083-6473. DOI: 10.12716/1001.08.03.18. Cit. on p. 52.

APPENDIX A – EQUATION DERIVATION

A.1 Damping simplification

Recalling the formulation in (4.29):

$$\begin{aligned}
\Gamma_u(\nu) &= -\frac{1}{2}\rho T \int_{-L/2}^{L/2} C_x(\beta_{crx}) V_{crx}^2 dx \\
\Gamma_v(\nu) &= -\frac{1}{2}\rho T \int_{-L/2}^{L/2} C_y(\beta_{crx}) V_{crx}^2 dx \\
\Gamma_r(\nu) &= -\frac{1}{2}\rho T \int_{-L/2}^{L/2} \left(C_y(\beta_{crx}) V_{crx}^2 - C_y(\psi_{cr}) V_{cr}^2 \right) x dx - \frac{1}{2}\rho T L^2 C_z(\psi_{cr}) V_{cr}^2
\end{aligned} \tag{A.1}$$

The mentioned relative velocity term V_{crx} that reaches the section x of the ship can be written as:

$$\begin{aligned}
\vec{V}_{crx} = \begin{pmatrix} u_{rx} \\ v_{rx} \end{pmatrix} &= \begin{pmatrix} u \\ v + rx \end{pmatrix} - \overbrace{J_\Theta(\eta)^{-1} \vec{V}_c|_{\text{NED}}}^{(4.3)} \\
&= \begin{pmatrix} u \\ v + rx \end{pmatrix} - \begin{bmatrix} \cos\psi & -\sin\psi \\ \sin\psi & \cos\psi \end{bmatrix}^{-1} \begin{pmatrix} V_x^{\text{NED}} \\ V_y^{\text{NED}} \end{pmatrix} \\
&= \begin{pmatrix} u - V_x^{\text{NED}} \cos\psi - V_y^{\text{NED}} \sin\psi \\ v + rx + V_x^{\text{NED}} \sin\psi - V_y^{\text{NED}} \cos\psi \end{pmatrix}
\end{aligned} \tag{A.2}$$

While the relative drift angle at the section x:

$$\tan\beta_{crx} = \frac{v + rx}{u} \overbrace{\approx \beta_{crx}}^{\text{for small angles}} \tag{A.3}$$

The quadratic term V_{crx}^2 is then:

$$
\begin{aligned}
V_{crx}^2 &= (u - V_x^{\mathrm{NED}}\cos\psi - V_y^{\mathrm{NED}}\sin\psi)^2 + (v + rx + V_x^{\mathrm{NED}}\sin\psi - V_y^{\mathrm{NED}}\cos\psi)^2 \\
&= u^2 + (V_x^{\mathrm{NED}}\cos\psi)^2 + (V_y^{\mathrm{NED}}\sin\psi)^2 - 2u(V_x^{\mathrm{NED}}\cos\psi + V_y^{\mathrm{NED}}\sin\psi) \\
&+ 2V_x^{\mathrm{NED}}\cos\psi V_y^{\mathrm{NED}}\sin\psi \\
&+ (v + rx)^2 + (V_x^{\mathrm{NED}}\sin\psi)^2 + (V_y^{\mathrm{NED}}\cos\psi)^2 + 2(v + rx)(V_x^{\mathrm{NED}}\sin\psi - V_y^{\mathrm{NED}}\cos\psi) \\
&- 2V_x^{\mathrm{NED}}\sin\psi V_y^{\mathrm{NED}}\cos\psi \\
&= u^2 + (V_x^{\mathrm{NED}})^2 + (V_y^{\mathrm{NED}})^2 - 2u(V_x^{\mathrm{NED}}\cos\psi + V_y^{\mathrm{NED}}\sin\psi) \\
&+ (v^2 + 2vrx + r^2x^2) + 2(v + rx)(V_x^{\mathrm{NED}}\sin\psi - V_y^{\mathrm{NED}}\cos\psi)
\end{aligned}
\tag{A.4}
$$

Considering a scenario without any external currents, $V_x^{\mathrm{NED}} = V_y^{\mathrm{NED}} = 0$, thus (A.4) can be reduced to:

$$
V_{crx}^2 = u^2 + (v^2 + 2vrx + r^2x^2) \tag{A.5}
$$

The main equations used in the 3P estimator were developed from (4.28) assuming the simplification in (6.1):

$$
\begin{aligned}
C_x(\beta) &= C_0^x + X_{\beta\beta}\beta^2 \\
C_y(\beta) &= Y_\beta\beta \\
C_z(\beta) &= N_\beta\beta
\end{aligned}
\tag{A.6}
$$

A.1.1 Surge force

The surge hydrodynamic component is described by:

$$
\Gamma_u(\nu) = -\frac{1}{2}\rho T\int_{-L/2}^{L/2} C_x(\beta_{crx})V_{crx}^2 dx \tag{A.7}
$$

By incorporating the simplification in (6.1) along with (A.3) and (A.5):

$$
\begin{aligned}
\Gamma_u(\nu) &= -\frac{1}{2}\rho T \int_{-L/2}^{L/2} \left(\left(C_0^x + X_{\beta\beta} \left(\frac{v+rx}{u} \right)^2 \right) (u^2 + (v^2 + 2vrx + r^2x^2)) \right) dx \\
&= -\frac{1}{2}\rho T \left(C_0^x \int_{-L/2}^{L/2} (u^2 + (v^2 + 2vrx + r^2x^2) dx \right. \\
&\qquad \left. + X_{\beta\beta} \int_{-L/2}^{L/2} \left(\frac{v+rx}{u} \right)^2 (u^2 + (v^2 + 2vrx + r^2x^2) dx \right) \\
&= -\frac{1}{2}\rho T \left(C_0^x \left(L(u^2+v^2) + \frac{1}{12}L^3r^2 \right) \right. \\
&\qquad \left. + X_{\beta\beta} \left(L\frac{v^2}{u^2}(u^2+v^2) + \frac{1}{12}L^3r^2 + \frac{1}{2}L^3\frac{v^2}{u^2}r^2 + \frac{1}{80}L^5\frac{r^4}{u^2} \right) \right) \\
\Gamma_u(\nu) &= -\frac{1}{2}\rho LT(C_0^x + X_{\beta\beta}\beta^2)(u^2+v^2) - \frac{1}{24}\rho L^3T(C_0^x + X_{\beta\beta})r^2 \\
&\quad - \frac{1}{4}\rho L^3T\, X_{\beta\beta}\beta^2r^2 - \frac{1}{160}\rho L^5T X_{\beta\beta}\frac{r^4}{u^2}
\end{aligned}
\tag{A.8}
$$

For a scenario with movement only in surge direction ($v = r = \beta = 0$):

$$
\Gamma_u(\nu) = -\frac{1}{2}\rho LTC_0^x u^2 \tag{A.9}
$$

A.1.2 Sway force

The sway hydrodynamic component is described by:

$$
\Gamma_v(\nu) = -\frac{1}{2}\rho T \int_{-L/2}^{L/2} C_y(\beta_{crx}) V_{crx}^2 dx \tag{A.10}
$$

Again by incorporating the simplification in (6.1) along with (A.3) and (A.5):

$$
\begin{aligned}
\Gamma_v(\nu) &= -\frac{1}{2}\rho T \int_{-L/2}^{L/2} \left(Y_\beta \left(\frac{v+rx}{u} \right) (u^2 + (v^2 + 2vrx + r^2x^2) \right) dx \\
&= -\frac{1}{2}\rho T \frac{Y_\beta}{u} \int_{-L/2}^{L/2} \left(u^2v + v^3 + 2v^2rx + vr^2x^2 + u^2rx + v^2rx + 2vr^2x^2 + r^3x^3 \right) dx \\
&= -\frac{1}{2}\rho T \frac{Y_\beta}{u} \int_{-L/2}^{L/2} \left(u^2v + v^3 + u^2rx + 3v^2rx + 3vr^2x^2 + r^3x^3 \right) dx \\
\Gamma_v(\nu) &= -\frac{1}{2}\rho LTY_\beta\beta(u^2+v^2) - \frac{1}{8}\rho L^3TY_\beta\beta r^2
\end{aligned}
\tag{A.11}
$$

A.1.3 Yaw moment

Finally, the yaw hydrodynamic component is described by:

$$\Gamma_r(\nu) = -\frac{1}{2}\rho T \int_{-L/2}^{L/2} \left(C_y(\beta_{crx})V_{crx}^2 - C_y(\beta_{cr})V_{cr}^2\right) x dx - \frac{1}{2}\rho T L^2 C_z(\beta_{cr})V_{cr}^2 \tag{A.12}$$

As V_{cr} is simply V_{crx} at midships $x = 0$:

$$V_{crx}^2 - V_{cr}^2 = 2vrx + r^2x^2 \tag{A.13}$$

Analogous to the surge and surge previous derivations, by replacing (A.1), (A.3) and (A.5) in (A.12), its integral term becomes:

$$\begin{aligned}
&\int_{-L/2}^{L/2} \left(C_y(\beta_{crx})V_{crx}^2 - C_y(\beta_{cr})V_{cr}^2\right) x dx = \\
&= \int_{-L/2}^{L/2} \left(Y_\beta \left(\frac{v + rx}{u}\right)(u^2 + (v^2 + 2vrx + r^2x^2)) - Y_\beta \frac{v}{u}(u^2 + v^2)\right) x dx \\
&= Y_\beta \int_{-L/2}^{L/2} \left(\frac{vx}{u}(2vrx + r^2x^2) + \frac{rx^2}{u}(u^2 + v^2 + 2vrx + r^2x^2)\right) dx \\
&= Y_\beta \frac{1}{u} \int_{-L/2}^{L/2} \left(2v^2rx^2 + vr^2x^3 + u^2rx^2 + v^2rx^2 + 2vr^2x^3 + r^3x^4\right) dx \\
&= Y_\beta \frac{1}{u} \int_{-L/2}^{L/2} \left(u^2rx^2 + 3v^2rx^2 + 3vr^2x^3 + r^3x^4\right) dx \\
&= \frac{1}{80}L^5 Y_\beta \frac{r^3}{u} + \frac{1}{12}L^3 Y_\beta ru + \frac{1}{4}L^3 Y_\beta \frac{rv^2}{u}
\end{aligned} \tag{A.14}$$

Rejoining with (A.12):

$$\Gamma_r(\nu) = -\frac{1}{2}\rho T L^2 N_\beta \beta(u^2 + v^2) - \frac{1}{160}\rho L^5 T Y_\beta \frac{r^3}{u} - \frac{1}{24}\rho L^3 T Y_\beta ru - \frac{1}{8}\rho L^3 T Y_\beta \frac{rv^2}{u} \tag{A.15}$$

A.2 Surge current coefficient derivate in time

The drift coefficient can be calculated by:

$$\beta = \arctan\left(\frac{v}{u}\right) \tag{A.16}$$

As both u, v are functions in time, β would also be. By derivating through the chain rule:

$$\begin{aligned} (\tan\beta)'\dot{\beta} &= \frac{\dot{v}}{u} + \frac{-v\dot{u}}{u^2} \\ \dot{\beta} &= \cos^2(\beta)\frac{u\dot{v} - v\dot{u}}{u^2} \end{aligned} \tag{A.17}$$

From the approximation adopted in (6.1), we can derivate in time:

$$\begin{aligned} C_x(t) = C_0^x + X_{\beta\beta}\beta^2(t) \Rightarrow \dot{C}_x(t) &= 2X_{\beta\beta}\beta(t)\dot{\beta}(t) \\ \dot{C}_x &= 2X_{\beta\beta}\beta\cos\beta^2\frac{u\dot{v} - v\dot{u}}{u^2} \\ \dot{C}_x &= 2X_{\beta\beta}\beta\frac{u\dot{v} - v\dot{u}}{u^2 + v^2} \end{aligned} \tag{A.18}$$

APPENDIX B – SIMULATION AND ANALYSES DATA

B.1 Vessel data

In this section the data used from each vessel is described:

Table 5: Data for the vessel 0 used in the maneuver.

Vessel no. **0**			Vessel class	Bulk carrier	
General dimensions			LOA 254 m Beam 43 m Draft 11.5 m		
Propeller dimensions	Diameter D_P (m)	7.5	Rudder dimensions	Area S_R (m^2)	60
	Wake fraction w_P	0.0		Wake fraction w_R	0.0
	Center of pressure x_P (m)	-119.0		Center of pressure x_R (m)	-124.0
Rigid-body terms	Mass m (t)	1.08×10^5	Added mass terms	pure surge $X_{\dot{u}}$ (t)	-6.23 x 10^3
	Inertia I_z ($t.m^2$)	4.52×10^8		pure sway $Y_{\dot{v}}$ (t)	-5.30 x 10^4
				pure yaw $N_{\dot{r}}$ ($t.m^2$)	-2.55 x 10^8
				sway-yaw $Y_{\dot{r}}$ (t.m)	-2.86 x 10^6
				yaw-sway $N_{\dot{v}}$ (t.m)	-2.86 x 10^6

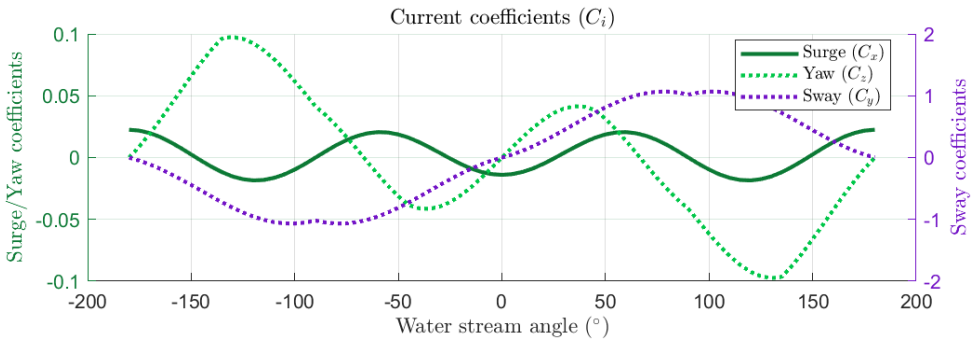

Figure 47: Current coefficients of the vessel 0 used in the maneuver.

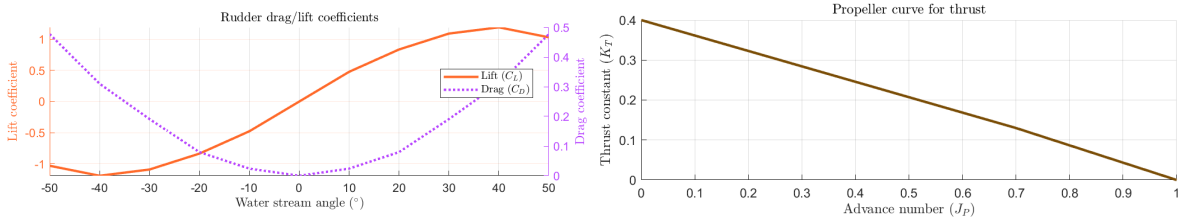

Figure 48: Curves for the rudder drag and lift coefficients (left) and propeller thrust constant (right) of the vessel 0 used in the maneuver.

Table 6: Data for the vessel 1 used in the maneuver.

Vessel no. **1**		Vessel class		Bulk carrier	
General dimensions		LOA 300 m Beam 50 m Draft 17.8 m			
Propeller dimensions	Diameter D_P (m)	8.2	Rudder dimensions	Area S_R (m^2)	70
	Wake fraction w_P	0.0		Wake fraction w_R	0.0
	Center of pressure x_P (m)	-140.0		Center of pressure x_R (m)	-145.0
Rigid-body terms	Mass m (t)	2.22×10^5	Added mass terms	pure surge $X_{\dot{u}}$ (t)	-1.20 x 10^4
	Inertia I_z (t.m^2)	1.25×10^9		pure sway $Y_{\dot{v}}$ (t)	-1.65 x 10^5
				pure yaw $N_{\dot{r}}$ (t.m^2)	-7.45 x 10^8
				sway-yaw $Y_{\dot{r}}$ (t.m)	-4.99 x 10^5
				yaw-sway $N_{\dot{v}}$ (t.m)	-4.99 x 10^5

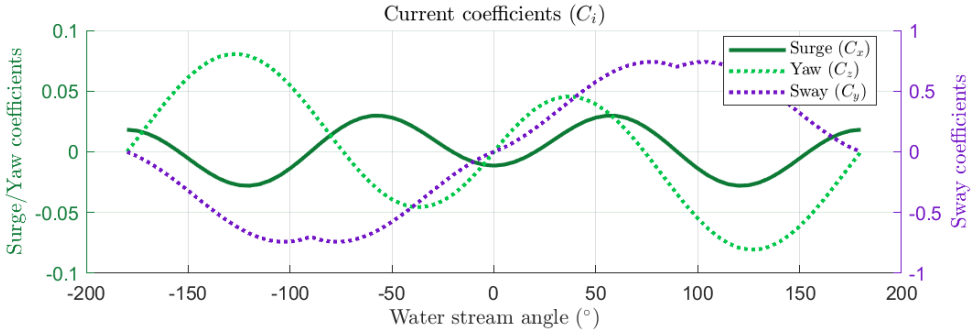

Figure 49: Current coefficients of the vessel 1 used in the maneuver.

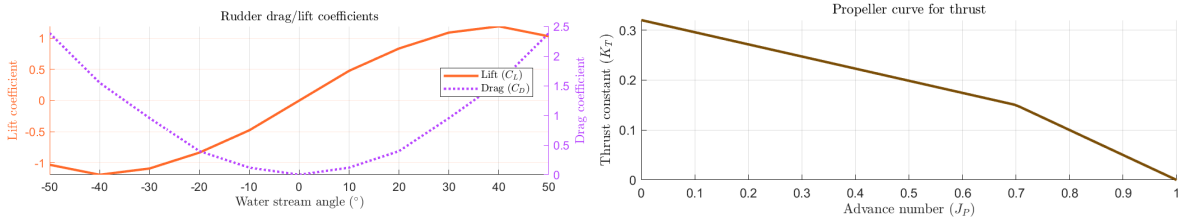

Figure 50: Curves for the rudder drag and lift coefficients (left) and propeller thrust constant (right) of the vessel 1 used in the maneuver.

Table 7: Data for the vessel 2 used in the maneuver.

Vessel no. **2**			Vessel class		Tanker ship
General dimensions			LOA 278.5 m Beam 51 m Draft 17.2 m		
Propeller dimensions	Diameter D_P (m)	8.3	Rudder dimensions	Area S_R (m^2)	50
	Wake fraction w_P	0.0		Wake fraction w_R	0.0
	Center of pressure x_P (m)	-127.4		Center of pressure x_R (m)	-133.0
Rigid-body terms	Mass m (t)	1.84×10^5	Added mass terms	pure surge $X_{\dot{u}}$ (t)	-1.03 x 10^4
	Inertia I_z ($t.m^2$)	8.70×10^8		pure sway $Y_{\dot{v}}$ (t)	-6.80 x 10^4
				pure yaw $N_{\dot{r}}$ ($t.m^2$)	-5.10 x 10^8
				sway-yaw $Y_{\dot{r}}$ (t.m)	-2.49 x 10^7
				yaw-sway $N_{\dot{v}}$ (t.m)	-2.49 x 10^7

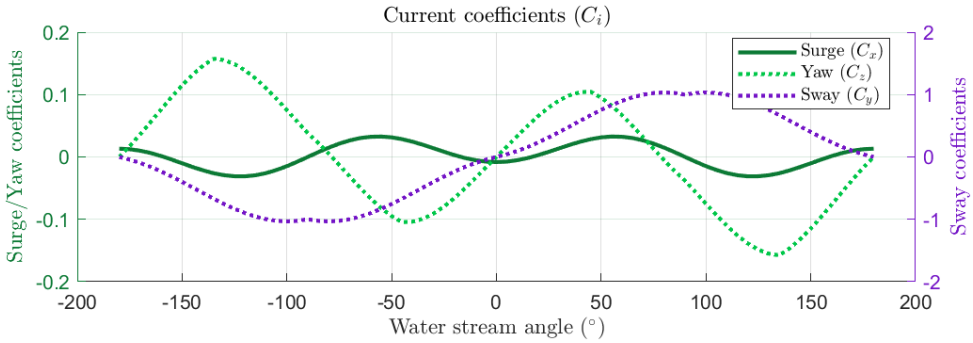

Figure 51: Current coefficients of the vessel 2 used in the maneuver.

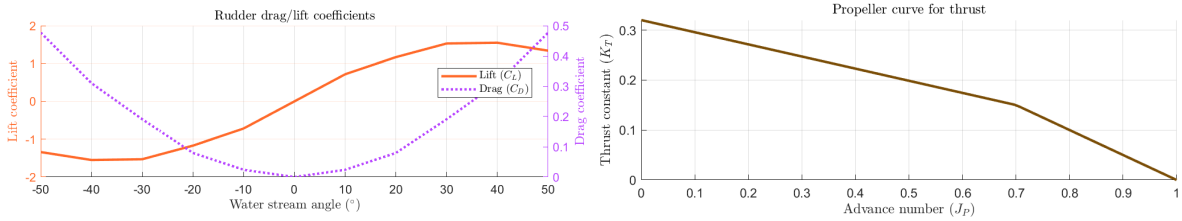

Figure 52: Curves for the rudder drag and lift coefficients (left) and propeller thrust constant (right) of the vessel 2 used in the maneuver.

Table 8: Data for the vessel 3 used in the maneuver.

Vessel no. **3**			Vessel class		Tanker ship
General dimensions			LOA 278.5 m Beam 48 m Draft 17.2 m		
Propeller dimensions	Diameter D_P (m)	8.3	Rudder dimensions	Area S_R (m^2)	60
	Wake fraction w_P	0.0		Wake fraction w_R	0.0
	Center of pressure x_P (m)	-127.4		Center of pressure x_R (m)	-133.0
Rigid-body terms	Mass m (t)	1.84×10^5	Added mass terms	pure surge $X_{\dot{u}}$ (t)	-1.03 x 10^4
	Inertia I_z ($t.m^2$)	8.70×10^8		pure sway $Y_{\dot{v}}$ (t)	-6.80 x 10^4
				pure yaw $N_{\dot{r}}$ ($t.m^2$)	-5.10 x 10^8
				sway-yaw $Y_{\dot{r}}$ (t.m)	-2.49 x 10^7
				yaw-sway $N_{\dot{v}}$ (t.m)	-2.49 x 10^7

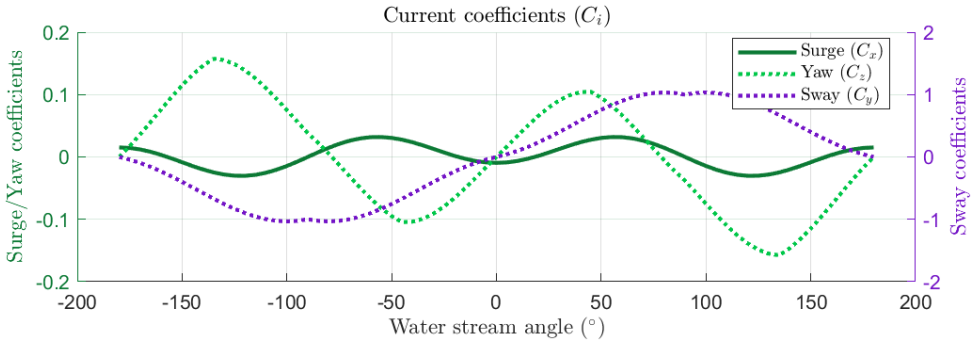

Figure 53: Current coefficients of the vessel 3 used in the maneuver.

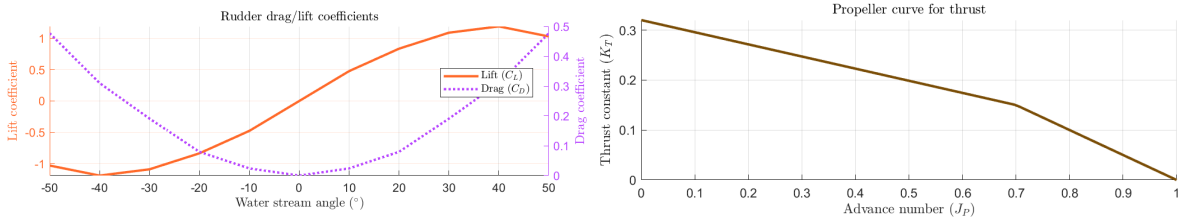

Figure 54: Curves for the rudder drag and lift coefficients (left) and propeller thrust constant (right) of the vessel 3 used in the maneuver.

Table 9: Data for the vessel 4 used in the maneuver.

Vessel no. **4**		Vessel class		Container carrier	
General dimensions		LOA 244 m Beam 32.2 m Draft 12.5 m			
Propeller dimensions	Diameter D_P (m)	7.6	Rudder dimensions	Area S_R (m^2)	51
	Wake fraction w_P	0.0		Wake fraction w_R	0.0
	Center of pressure x_P (m)	-110.0		Center of pressure x_R (m)	-115.0
Rigid-body terms	Mass m (t)	6.24×10^4	Added mass terms	pure surge $X_{\dot{u}}$ (t)	-4.34 x 10^3
	Inertia I_z ($t.m^2$)	2.40×10^8		pure sway $Y_{\dot{v}}$ (t)	-3.10 x 10^4
				pure yaw $N_{\dot{r}}$ ($t.m^2$)	-2.05 x 10^8
				sway-yaw $Y_{\dot{r}}$ (t.m)	-7.51 x 10^5
				yaw-sway $N_{\dot{v}}$ (t.m)	-7.51 x 10^5

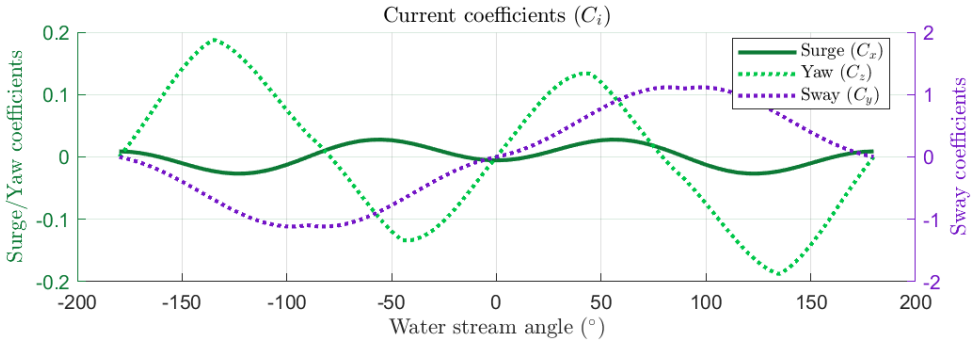

Figure 55: Current coefficients of the vessel 4 used in the maneuver.

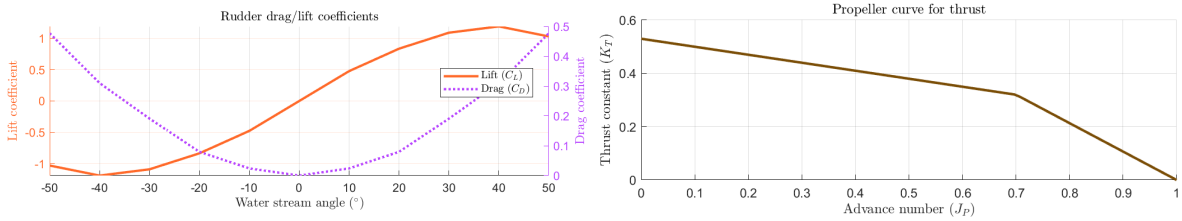

Figure 56: Curves for the rudder drag and lift coefficients (left) and propeller thrust constant (right) of the vessel 4 used in the maneuver.

Table 10: Data for the vessel 5 used in the maneuver.

Vessel no. **5**		Vessel class		Container carrier	
General dimensions		LOA 300 m Beam 48 m Draft 13.7 m			
Propeller dimensions	Diameter D_P (m)	9.3	Rudder dimensions	Area S_R (m^2)	74
	Wake fraction w_P	0.0		Wake fraction w_R	0.0
	Center of pressure x_P (m)	-137.0		Center of pressure x_R (m)	-145.0
Rigid-body terms	Mass m (t)	1.34×10^5	Added mass terms	pure surge $X_{\dot{u}}$ (t)	-1.88 x 10^4
	Inertia I_z ($t.m^2$)	7.93×10^8		pure sway $Y_{\dot{v}}$ (t)	-6.50 x 10^4
				pure yaw $N_{\dot{r}}$ ($t.m^2$)	-8.67 x 10^8
				sway-yaw $Y_{\dot{r}}$ (t.m)	-2.61 x 10^6
				yaw-sway $N_{\dot{v}}$ (t.m)	-2.61 x 10^6

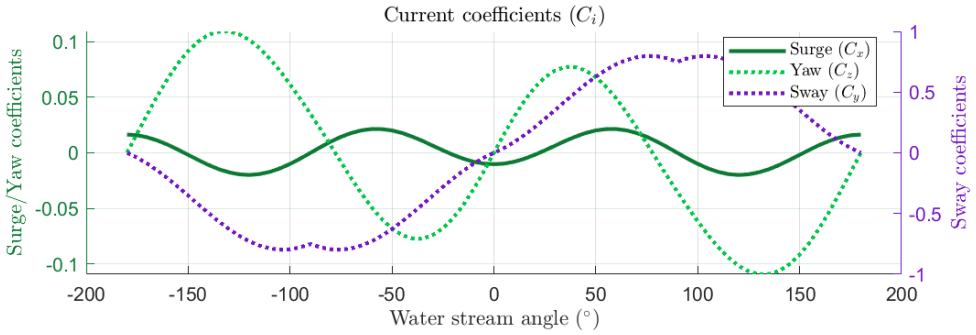

Figure 57: Current coefficients of the vessel 5 used in the maneuver.

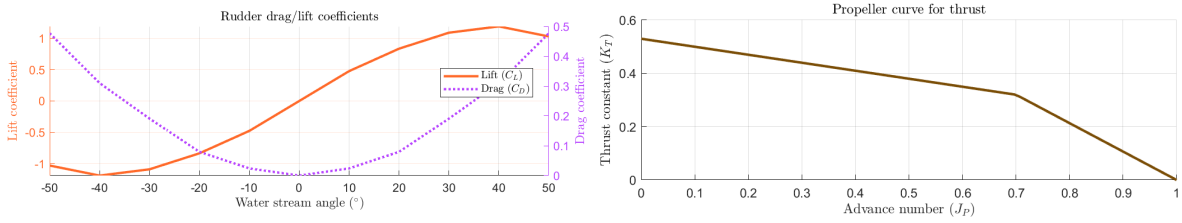

Figure 58: Curves for the rudder drag and lift coefficients (left) and propeller thrust constant (right) of the vessel 5 used in the maneuver.

Table 11: Data for the vessel 6 used in the maneuver.

Vessel no. **6**		Vessel class		Container carrier	
General dimensions		LOA 366 m Beam 51 m Draft 15.0 m			
Propeller dimensions	Diameter D_P (m)	9.0	Rudder dimensions	Area S_R (m^2)	58
	Wake fraction w_P	0.0		Wake fraction w_R	0.3
	Center of pressure x_P (m)	-164.7		Center of pressure x_R (m)	-173.5
Rigid-body terms	Mass m (t)	1.96×10^5	Added mass terms	pure surge $X_{\dot{u}}$ (t)	-1.68 x 10^4
	Inertia I_z ($t.m^2$)	1.62×10^9		pure sway $Y_{\dot{v}}$ (t)	-2.50 x 10^5
				pure yaw $N_{\dot{r}}$ ($t.m^2$)	-1.30 x 10^9
				sway-yaw $Y_{\dot{r}}$ (t.m)	-2.92 x 10^6
				yaw-sway $N_{\dot{v}}$ (t.m)	-2.92 x 10^6

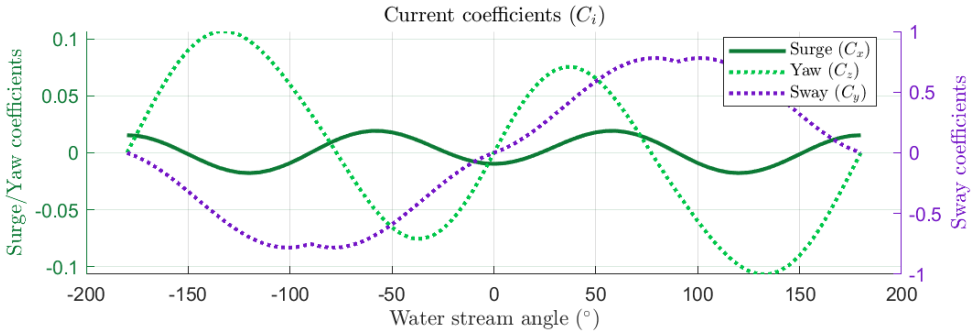

Figure 59: Current coefficients of the vessel 6 used in the maneuver.

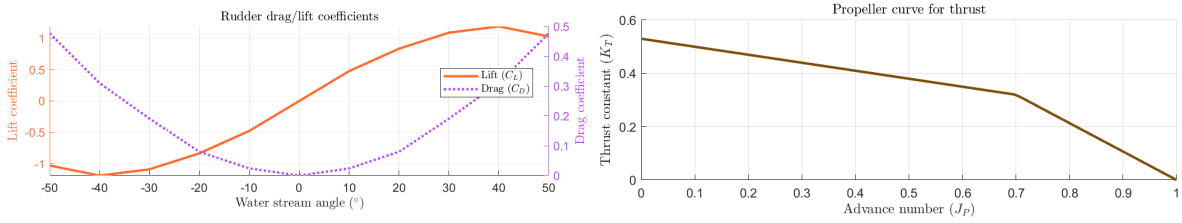

Figure 60: Curves for the rudder drag and lift coefficients (left) and propeller thrust constant (right) of the vessel 6 used in the maneuver.

Table 12: Data for the vessel 7 used in the maneuver.

Vessel no. **7**		Vessel class		Container ship	
General dimensions		Length Overall (LOA) 335 m Beam 51 m Draft 13.8 m			
Propeller dimensions	Diameter D_P (m)	9.3	Rudder dimensions	Area S_R (m^2)	80
	Wake fraction w_P	0.0		Wake fraction w_R	0.0
	Center of pressure x_P (m)	-155.0		Center of pressure x_R (m)	-160.0
Rigid-body terms	Mass m (t)	1.62×10^5	Added mass terms	pure surge $X_{\dot{u}}$ (t)	-2.05 x 10^4
	Inertia I_z (t.m^2)	1.13×10^9		pure sway $Y_{\dot{v}}$ (t)	-8.05 x 10^4
				pure yaw $N_{\dot{r}}$ (t.m^2)	-1.38 x 10^9
				sway-yaw $Y_{\dot{r}}$ (t.m)	-3.42 x 10^7
				yaw-sway $N_{\dot{v}}$ (t.m)	-3.42 x 10^7

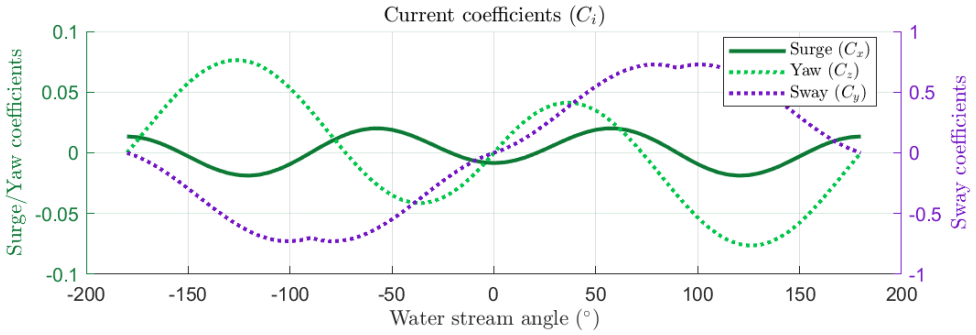

Figure 61: Current coefficients of the vessel 7 used in the maneuver.

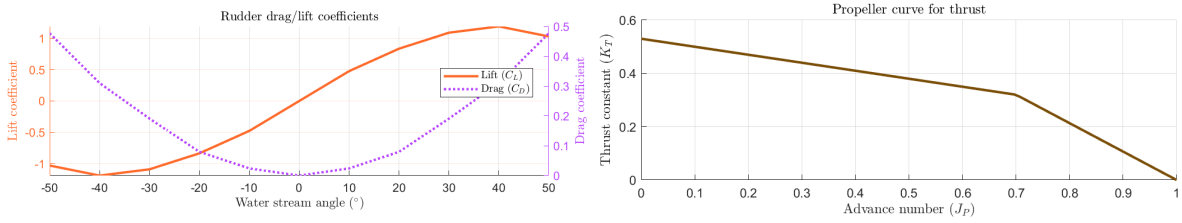

Figure 62: Curves for the rudder drag and lift coefficients (left) and propeller thrust constant (right) of the vessel 7 used in the maneuver.

Table 13: Data for the vessel used in the maneuver 8.

Vessel no. **8**			Vessel class	Container carrier	
General dimensions			LOA 366 m Beam 51 m Draft 12.8 m		
Propeller dimensions	Diameter D_P (m)	9.0	Rudder dimensions	Area S_R (m^2)	62
	Wake fraction w_P	0.0		Wake fraction w_R	0.0
	Center of pressure x_P (m)	-164.7		Center of pressure x_R (m)	-173.5
Rigid-body terms	Mass m (t)	1.59×10^5	Added mass terms	pure surge $X_{\dot{u}}$ (t)	-1.01 x 10^4
	Inertia I_z ($t.m^2$)	1.37×10^9		pure sway $Y_{\dot{v}}$ (t)	-7.10 x 10^4
				pure yaw $N_{\dot{r}}$ ($t.m^2$)	-8.47 x 10^8
				sway-yaw $Y_{\dot{r}}$ (t.m)	-1.98 x 10^6
				yaw-sway $N_{\dot{v}}$ (t.m)	-1.98 x 10^6

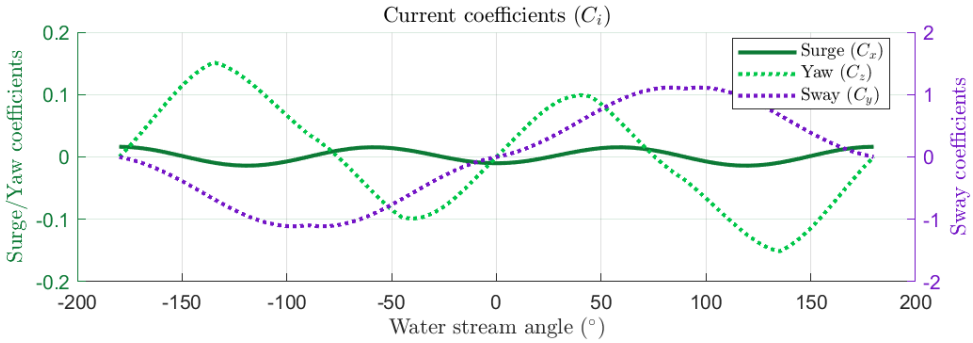

Figure 63: Current coefficients of the vessel 8 used in the maneuver.

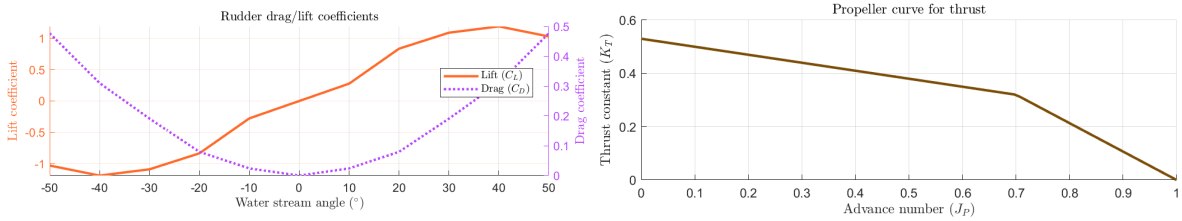

Figure 64: Curves for the rudder drag and lift coefficients (left) and propeller thrust constant (right) of the vessel 8 used in the maneuver.

Table 14: Data for the vessel 9 used in the maneuver.

Vessel no. **9**		Vessel class		Container carrier	
General dimensions		LOA 368 m Beam 51 m Draft 14.8 m			
Propeller dimensions	Diameter D_P (m)	9.0	Rudder dimensions	Area S_R (m^2)	78
	Wake fraction w_P	0.0		Wake fraction w_R	0.3
	Center of pressure x_P (m)	-164.7		Center of pressure x_R (m)	-173.5
Rigid-body terms	Mass m (t)	1.92×10^5	Added mass terms	pure surge $X_{\dot{u}}$ (t)	-6.20 x 10^3
	Inertia I_z ($t.m^2$)	1.66×10^9		pure sway $Y_{\dot{v}}$ (t)	-1.00 x 10^5
				pure yaw $N_{\dot{r}}$ ($t.m^2$)	-9.22 x 10^8
				sway-yaw $Y_{\dot{r}}$ (t.m)	-2.20 x 10^6
				yaw-sway $N_{\dot{v}}$ (t.m)	-2.19 x 10^6

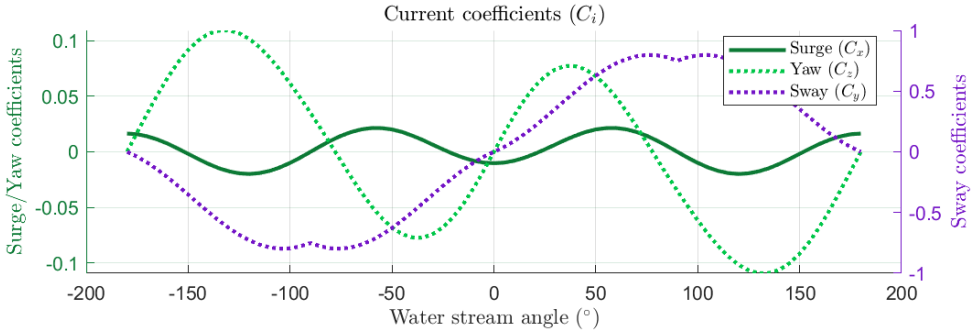

Figure 65: Current coefficients of the vessel 9 used in the maneuver.

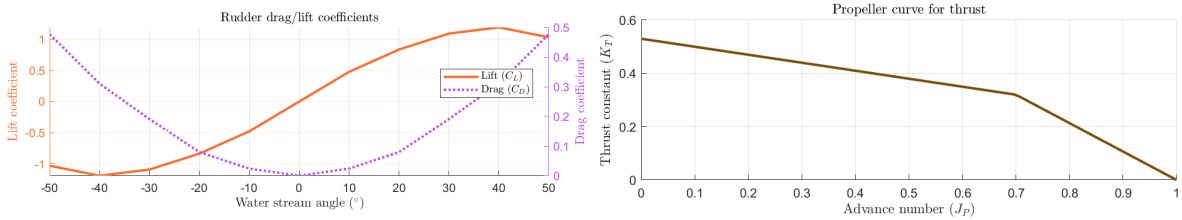

Figure 66: Curves for the rudder drag and lift coefficients (left) and propeller thrust constant (right) of the vessel 9 used in the maneuver.

B.2 Brief description of the real maneuvers

The simulated maneuver 0 was made in Santos Bay in a special conditioning without any external environmental condition. A bulk carrier was positioned on the entrance of the channel and the maneuver consisted in navigating towards one of the most internal terminal as shown in Fig.67.

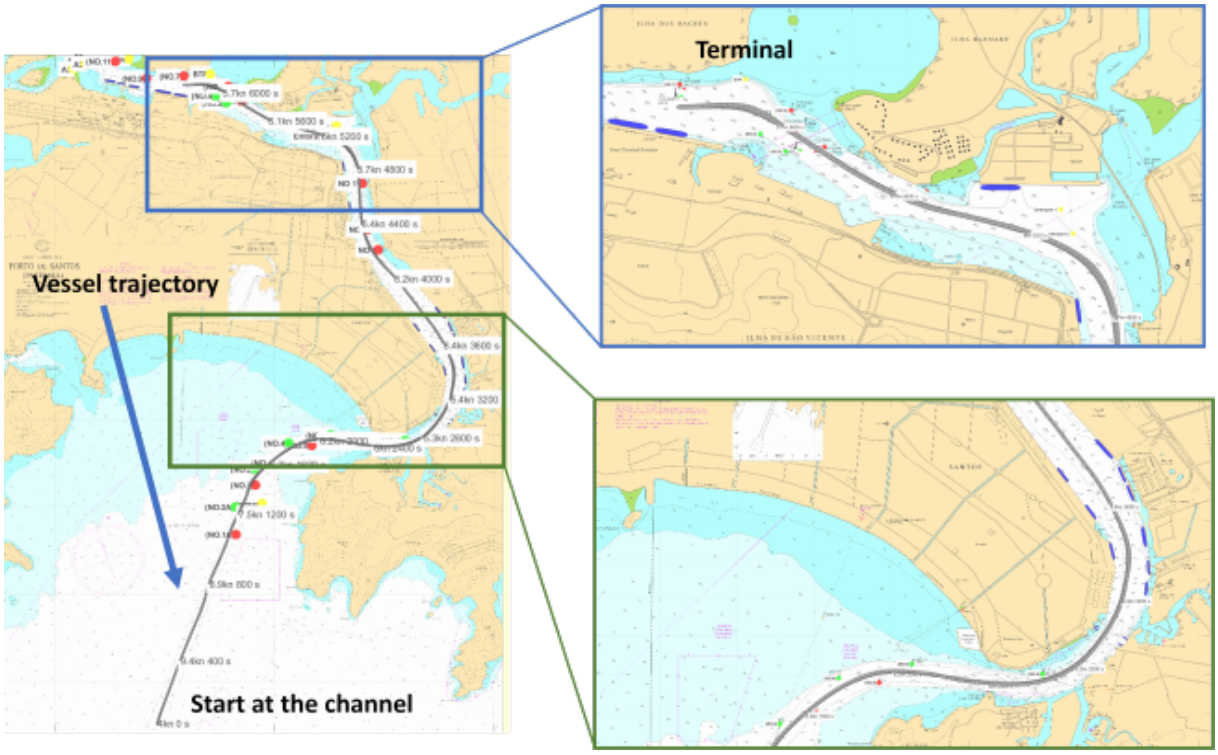

Figure 67: Simulated maneuver number 0 on Santos Bay scenario.

Maneuver 1 was conducted in a navigation channel near to access Itaguaí port in Rio de Janeiro, Brazil. Due to the surroundings islands, the channel makes a fairly accentuated curve to exit towards open seas. In the simulated scenario, there was a incident wind from Northeast with an average speed of 15 knots, currents going to West with 1.1 knots and waves from the Southwest with 0.3 meters height and period of 10 seconds. The ship was also a bulk carrier and an illustration of the maneuver can be seen in Fig.68.

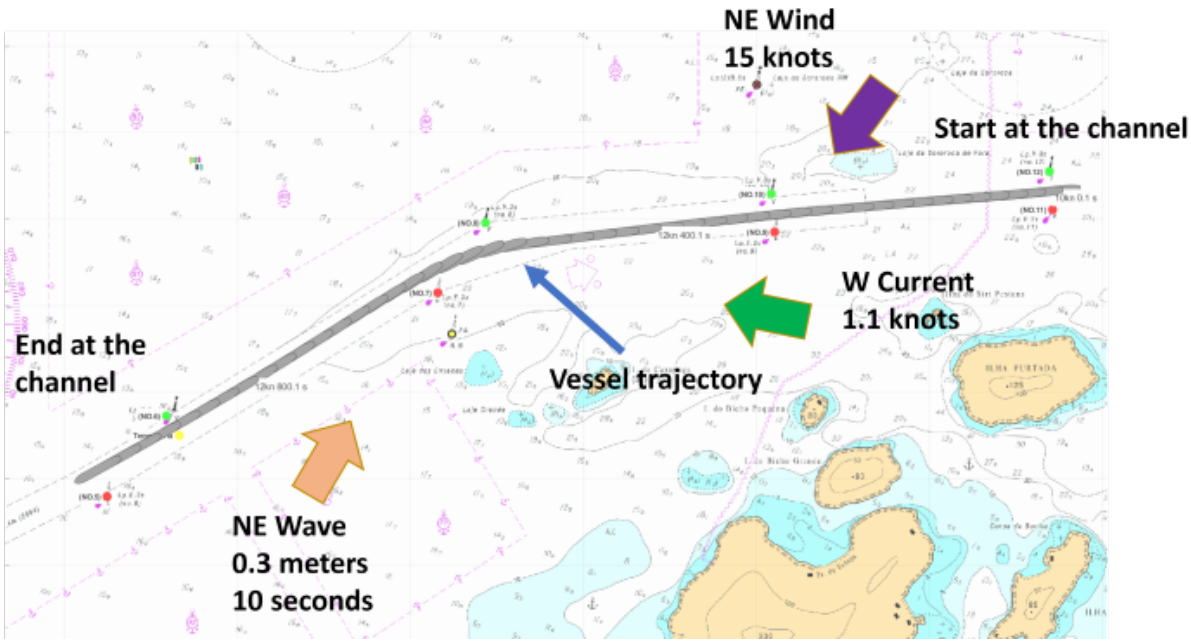

Figure 68: Simulated maneuver number 1 on the navigation channel to exit Itaguaí port.

Maneuver 2 was placed on the same location of the maneuver 1, but in a more inner portion of the channel, closer to the terminal port in another portion with an accentuated curve. The environmental conditions were set with a wind coming from West with an average of 15 knots, current going to Southeast with 0.8 knots and waves coming from West with 0.2 meters height and 8 seconds period as shown in Fig.69. The ship was entering towards the terminal area in the North. Both maneuvers 2 and 3 were done in Tanker ships.

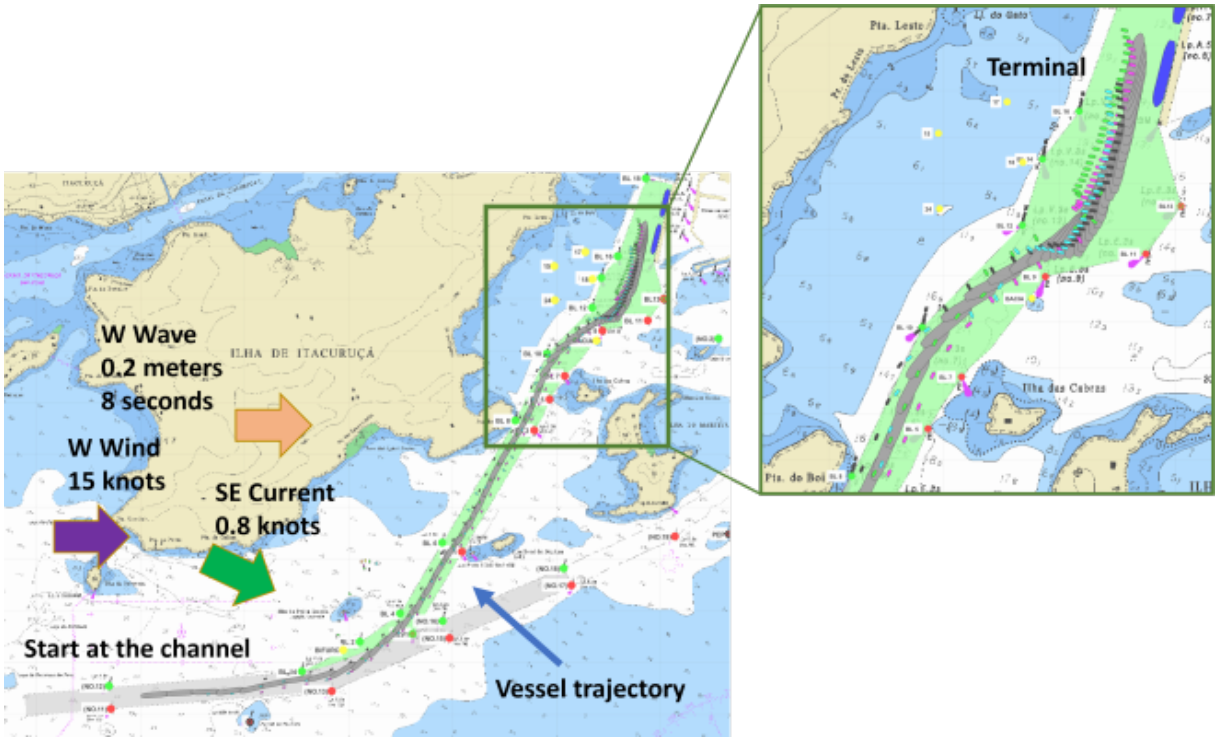

Figure 69: Simulated maneuver number 2 on the navigation channel to access Itaguaí port.

Placed in the exact same location of the maneuver 2, the maneuver 3 is done in the other way, simulating an outbound maneuver. The environmental conditions were set with a wind coming from North with an average of 18 knots, current going to West with 1.2 knots and waves coming from Northeast with 0.2 meters height and 8 seconds period as shown in Fig.70.

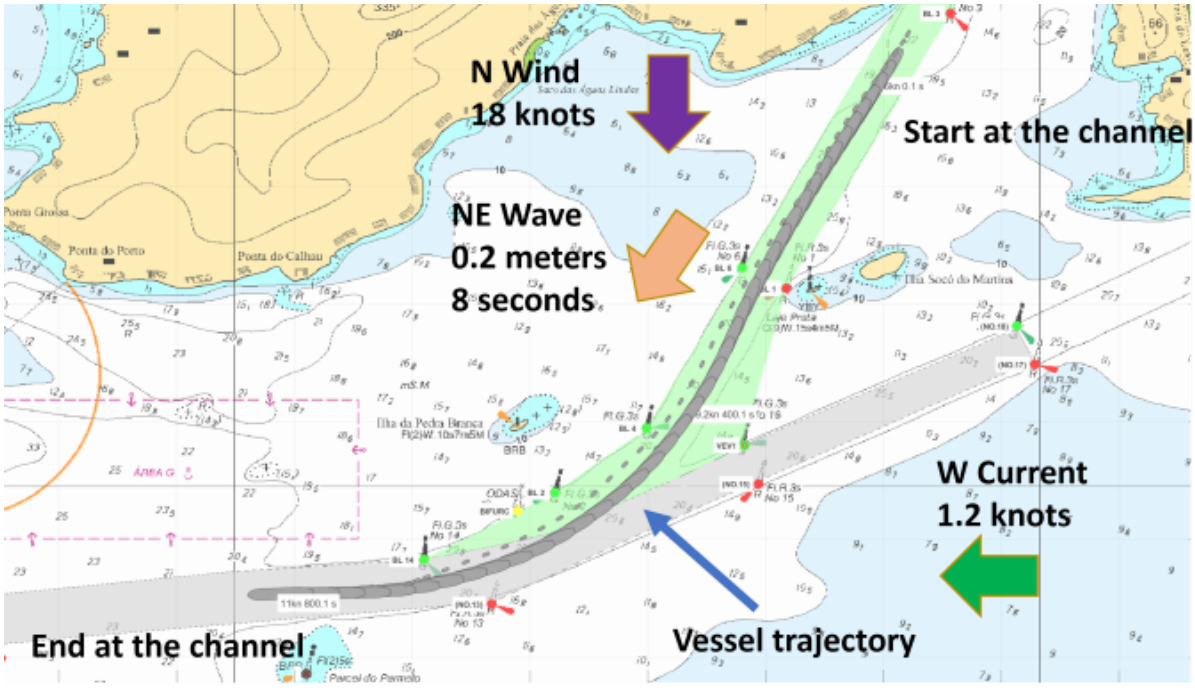

Figure 70: Simulated maneuver number 3 on the navigation channel to exit Itaguaí port.

Maneuver 4 consisted in an inbound maneuver in the Vitória Bay towards the terminal. In the most exposed area to the East, the wave were mainly coming from Northeast with 1 meter height and 9 seconds period, such value gradually decrease in the sheltered portion in the West until its effects become negligible. The current was going mainly towards East with 0.4 knots and wind coming from Southwest with 22 knots average as shown in Fig.71. Starting from here, all maneuvers onward were conducted with container ships.

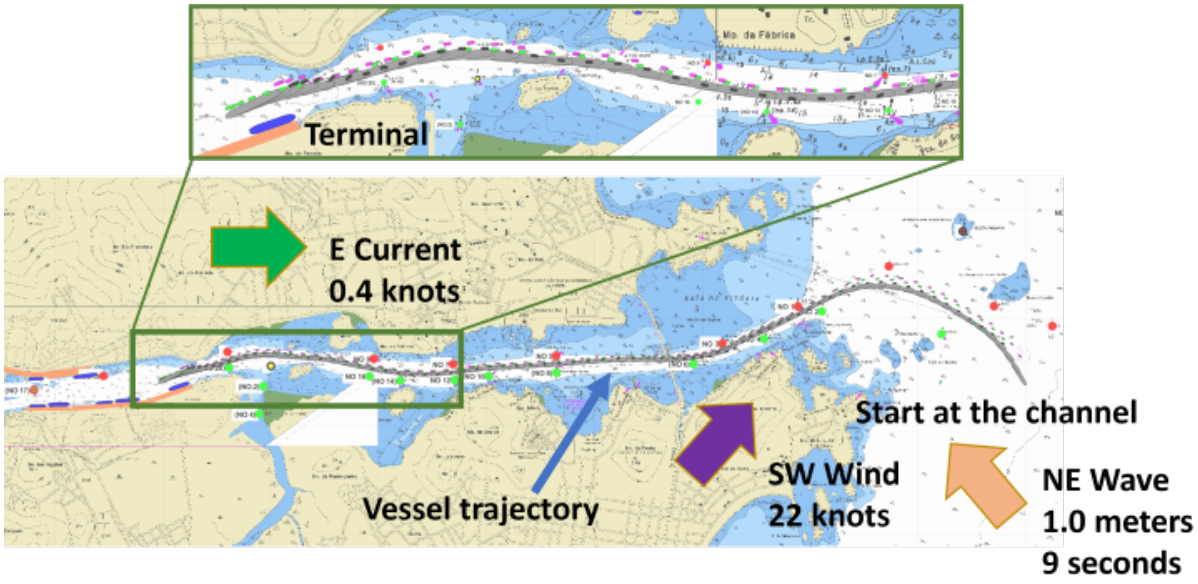

Figure 71: Simulated maneuver number 4 on Vitória Bay scenario.

Maneuver 5 simulated an entrance into the Santos Bay similarly to the maneuver 0, however, focusing in the entry portion where there is an accentuated curve which both current and wave exert more influence. In the most unsheltered area, the wind is coming from Southwest with 18 knots, wave from Southeast with 1.6 meters height and 12 seconds period, and current going towards East with 1 knot at the entrance section. Fig.72 better contextualize the maneuver.

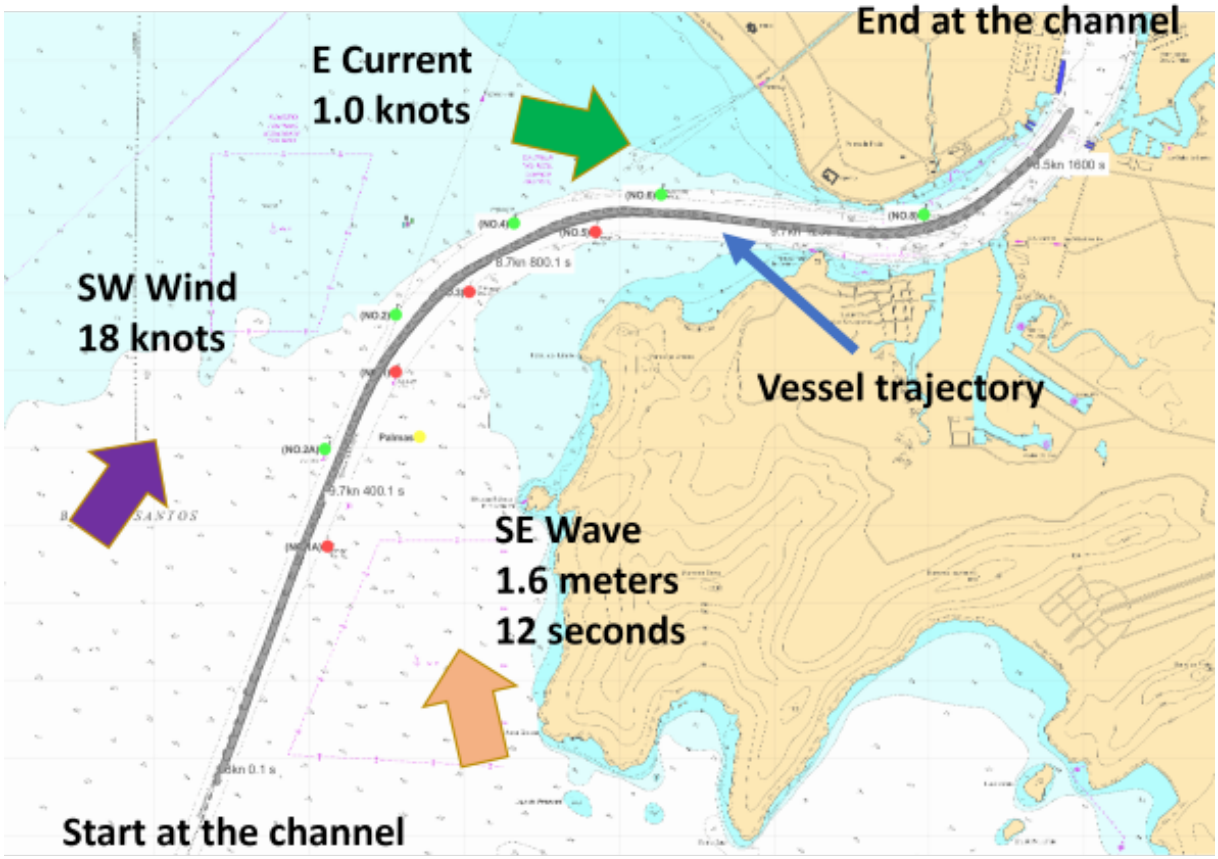

Figure 72: Simulated maneuver number 5 on Santos Bay entry channel scenario.

Maneuver 6 was set in the Suape port, in the most southern beach of Cabo de Santo Agostinho, in the state of Pernambuco, Brazil. Due to the draft of the container, the vessel had to strictly remain into the channel, avoiding the shallow areas around in North and South. At the same time, the wind was actuating from Southeast with 15 knots, current going to Northeast with 0.8 knots and wave coming from Southeast with 1.7 meters height and 10 seconds period. After the breakwater, these conditions were reduced. An illustration of the scenario can be seen in Fig.73.

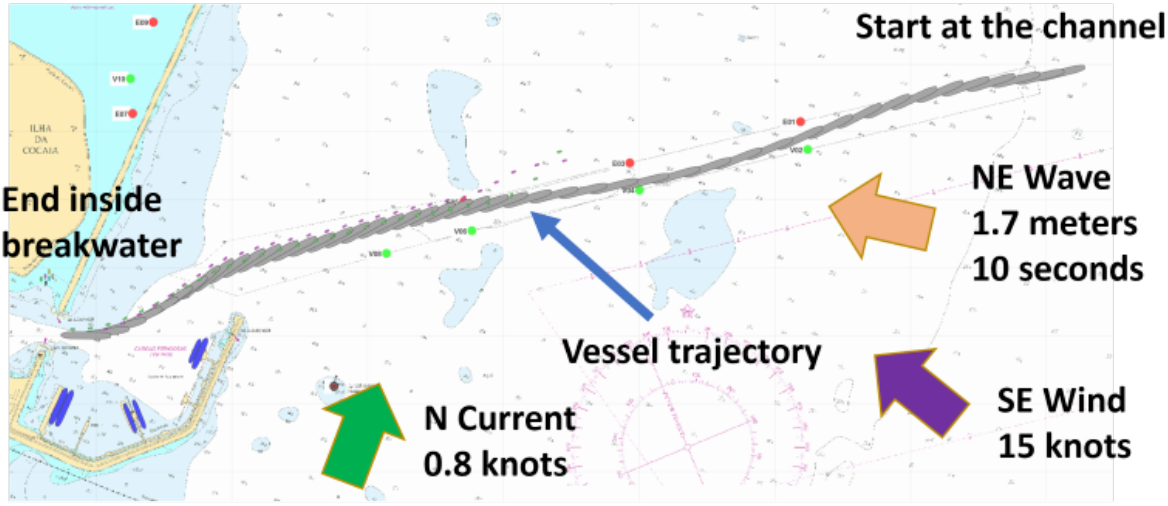

Figure 73: Simulated maneuver number 6 on the navigation channel to access Suape port.

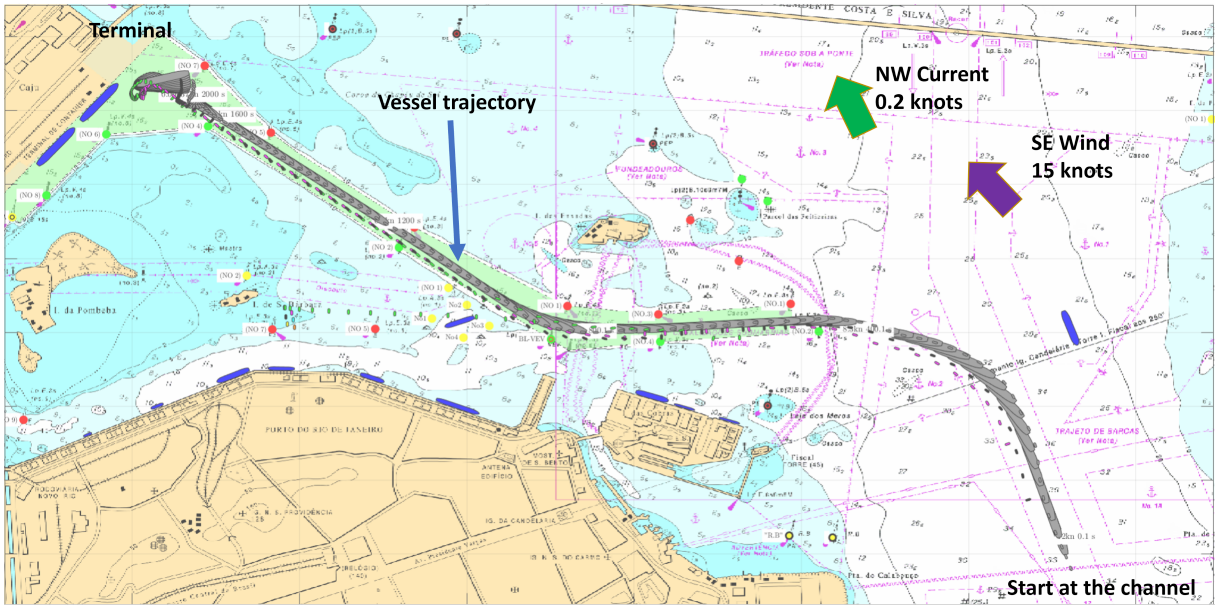

Figure 74: Simulated maneuver number 7 on Guanabara Bay scenario.

Maneuver 8 was simulated in the Paranagua Bay, in the Brazilian state of Paraná, starting in the most further point of the entry channel up until the terminal region. The conditions in the most unsheltered zone are wind coming from East with 15 knots, current entering the channel going to Northwest with 1.6 knots and wave coming from Southeast with 1.4 meters height and 13 seconds period as shown in Fig.75.

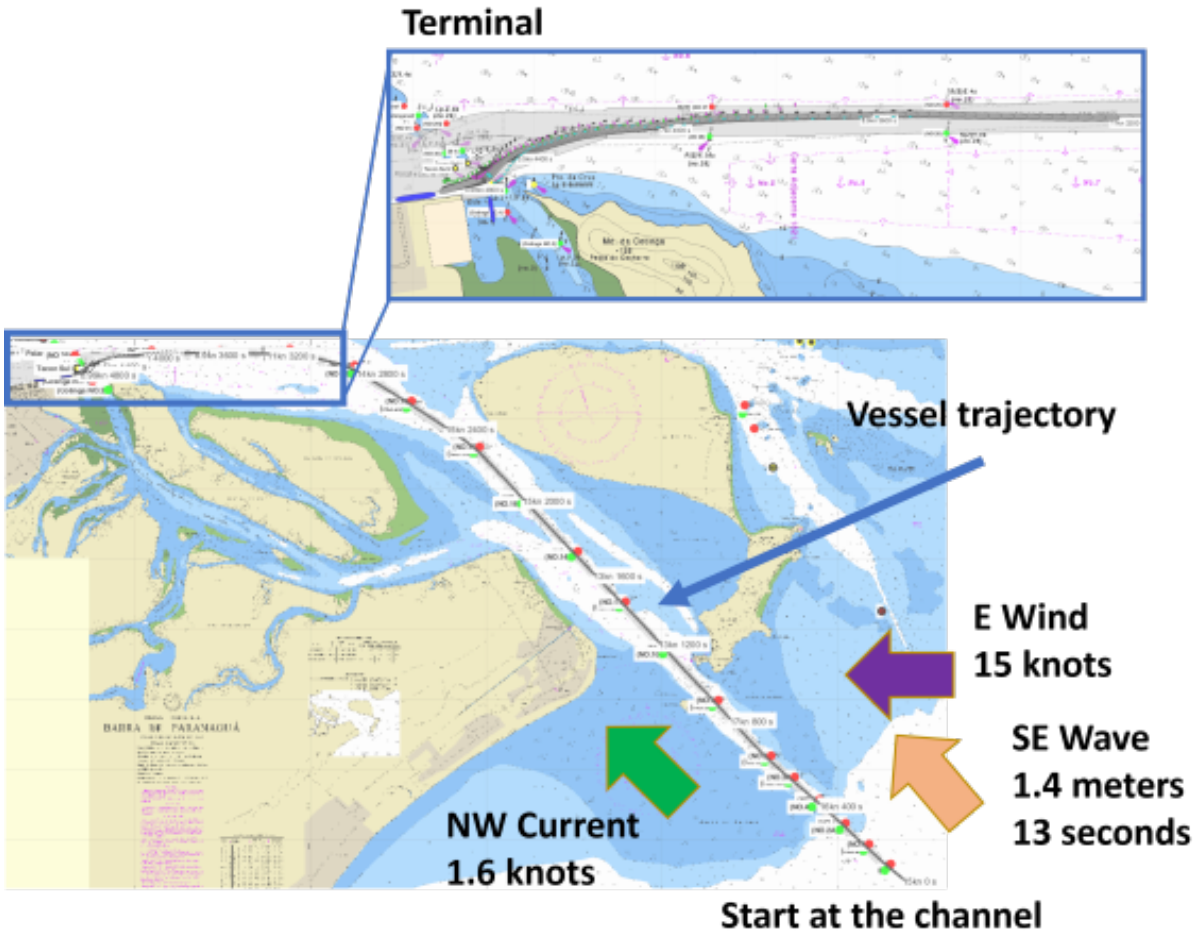

Figure 75: Simulated maneuver number 8 on Paranagua Bay scenario.

Maneuver 9 simulated an entrance into the Salvador port, in the Brazilian state of Bahia. The maneuver started from the access channel in the South and essentially was fairly simple as the only concerning points were the anchored vessels. The incident wind from Southeast was on average 16 knots with a current going to North with 2.3 knots. The maneuver for this work ended just before the usage of tugboats as shown in Fig.76.

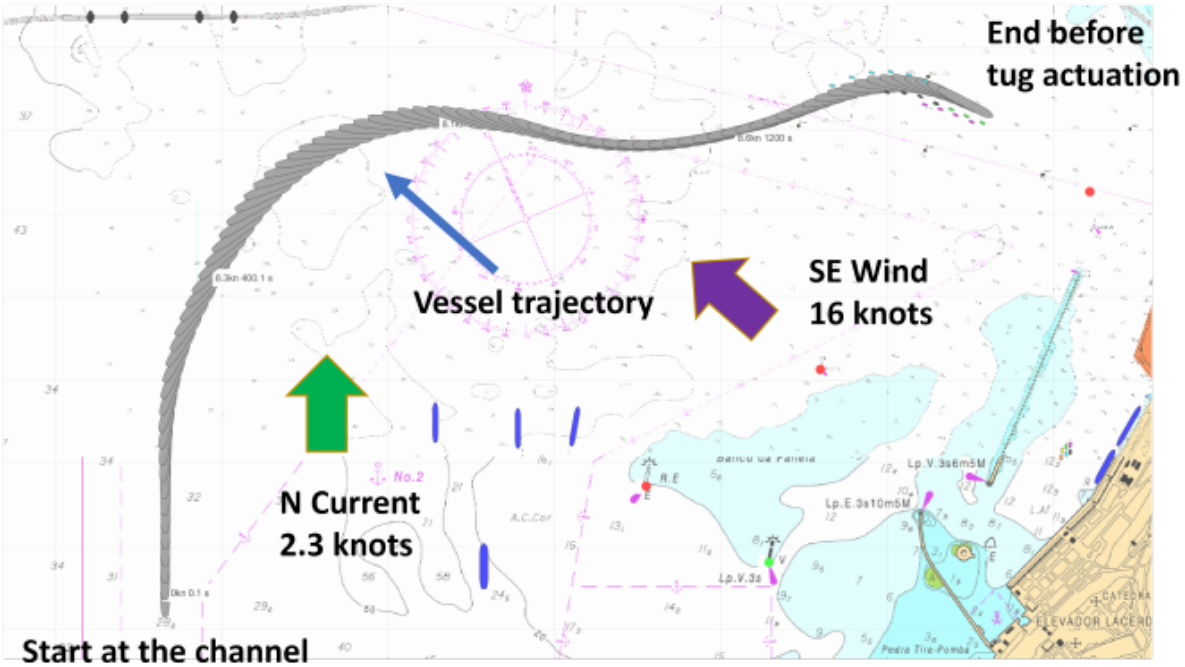

Figure 76: Simulated maneuver number 9 on Salvador Port scenario.